Deutsches Zentrum
DLR für Luft- und Raumfahrt

Universität zu Köln

Elastic Wave Propagation in Granular Packings

Inaugural-Dissertation

zur

Erlangung des Doktorgrades

der Mathematisch-Naturwissenschaftlichen Fakultät

der Universität zu Köln

vorgelegt von

Karsten Tell

aus Lauf a. d. Pegnitz

Köln, 2020

Berichterstatter:	Prof. Dr. Matthias Sperl
(Gutachter)	Prof. Dr. Stefan Luding
	Prof. Dr. Xiaoping Jia

Tag der mündlichen Prüfung: 14. August 2020

Ich widme diese Arbeit meinen Eltern Alfred und Olympia Tell.

Abstract

Jammed packings of granular materials such as sand, powders or glass beads show an effective elastic behavior. For a given confinement pressure p_0, volume fraction ϕ and coordination number Z an effective bulk- and shear-modulus arises which can be probed by measurements of the speed of sound for longitudinal and transverse elastic waves. For sufficiently high confinement pressure, low dynamic pressure and long wavelengths, wave propagation is well approximated by effective medium theory. At increasing amplitude or decreasing static pressure the effect of nonlinearities becomes increasingly noticeable. This results from nonlinear, dissipative and hysteretic contact forces on the microscopic scale and rearrangements in the force-chain network on the mesoscopic scale.

At low amplitudes, weakly-nonlinear behavior is found as a small correction to the linear elasticity. This leads to demodulation of incident waves, frequency-mixing and mode conversion between longitudinal and transversal waves. Upon vibrations of higher amplitudes, the static friction and static precompression are overcome, leading to irreversible changes in the force-chain network and elastic weakening. The wavefront speed drops in this intermediate amplitude regime. In the high-amplitude regime, when the dynamic pressure exceeds the static pressure, shock-like behavior with a characteristic increase in wavefront speed arises.

In this thesis, a fully automated experimental apparatus for elastic wave measurements at low confinement pressure was developed and used on a DLR sounding rocket campaign. During the microgravity phase of the MAPHEUS 8 mission, packings in the pressure range of 20 to 400 Pa were prepared and sound transmission at amplitudes varying by two orders of magnitude was measured. At the lowest amplitudes a linear regime with sound speed from 60 to 160 $\frac{m}{s}$ is found. The pressure dependence of the sound speed is found to vary with p_0^ν, ν being close to 1/3, deviating from the 1/6 exponent valid for high pressure and from the 1/4 exponent, previously reported in the literature to describe the low pressure behavior. Comparison with literature data at higher pressures suggests a continous increase of the exponent with pressure, similar to findings for 2D systems reported in the literature. In the present analysis, the logarithmic derivative is found constant over at least five orders of magnitude of pressure. Furthermore, for the highest amplitudes a drop in the wavefront-speed with increasing amplitude is found for p_0 between 100 and 400 Pa, suggesting elastic weakening, while for 20 and 50 Pa a rising wavefront speed is observed, suggesting shock-like behavior. Wave-front attenuation is found to be increased at the highest amplitudes, in agreement with previous results for shock-waves in glass bead packings on ground.

To further investigate wave propagation beyond effective medium theory, and to probe possible long correlation lengths related to anisotropy and unjamming, measurements of multiply-scattered elastic waves were conducted on ground with $p_0 \propto 1$ kPa. In measurements of the configurationally averaged incoherent intensity in the diffusive regime, the transport mean-free path is found between 1.6 and 1.8 bead diameters for a sample of small height, moderately affected by a hydrostatic gradient and close to 5 bead diameters for a larger sample affected by a much larger gradient. Similar values are found for the scattering mean-free path extracted from the attenuation of the coherent signal with varying sample thickness. These results are larger than literature values obtained at much higher pressure, where the hydrostatic gradient becomes negligible.

Finally, inverse-filtering and time-reversal techniques in a two transducer setup were used to measure wave focussing, to test it as a method for measuring microscopic rearrangements in the granular packing due to external excitation.

Kurzzusammenfassung

Verhakte (engl. 'jammed') Granulatpackungen aus Materialien wie Sand, Pulvern oder Glaskugeln zeigen ein effektives elastisches Verhalten. Bei gegebenem Einschlussdruck p_0, Volumenanteil ϕ und Koordinationszahl Z zeigt sich ein effektiver Kompressions- und Schermodul, welcher durch Messung der Schallgeschwindigkeit longitudinaler und transversaler elastischer Wellen untersucht werden kann. Bei hinreichend hohem Einschlussdruck, niedrigem dynamischem Druck und großer Wellenlänge ist die Wellenausbreitung in guter Näherung durch die Theorie des effektiven Mediums beschrieben. Bei steigender Amplitude oder sinkendem statischem Druck wird der Effekt von Nichtlinearitäten zunehmend stärker bemerkbar. Auf der mikroskopischen Skala resultiert dies aus nichtlinearen, dissipativen und hysteretischen Kontaktkräften und auf der mesoskopischen Skala aus Umlagerungen im Netzwerk der Kraftketten.

Bei niedrigen Amplituden wird schwach-nichtlineares Verhalten im Sinne einer kleinen Korrektur zur linearen Elastizität beobachtet. Dies führt zu Demodulation einfallender Wellen, Frequenz-Mischung und Modenkonversion zwischen longitudinalen und transversalen Wellen. Vibrationen höherer Amplitude überwinden statische Reibung wie auch Vorspannung der Kontakte, sodass irreversible Änderungen im Netzwerk der Kraftketten sowie elastischer Festigkeitsabfall auftreten. In diesem mittleren Amplitudenbereich fällt die Geschwindkeit der Wellenfront ab. Bei hohen Amplituden, wenn der dynamische Druck den Statischen übersteigt, zeigt sich Schockwellen-artiges Verhalten mit charakteristischem Anstieg der Geschwindigkeit der Wellenfront.

In dieser Arbeit wurde ein vollautomatischer experimenteller Apparat für Messungen elastischer Wellen bei niedrigem Einschlussdruck entwickelt und im Rahmen einer Messkampagne auf einer Höhenforschungs-rakete des DLR eingesetzt. Im Laufe der Mikrogravitationsphase während der MAPHEUS 8 Mission wurden Packungen mit Drücken zwischen 20 und 400 Pa präpariert und die Schalltransmission in einem Amplitudenbereich über zwei Größenordnungen gemessen. Bei den niedrigsten Amplituden zeigte sich ein linearer Bereich mit Schallgeschwingkeiten zwischen 60 und 160 m/s. Die Druckabhängigkeit schwankte wie p_0^ν mit ν nahe an 1/3, im Kontrast zum Exponenten 1/6, der bei hohen Drücken gilt, und zu 1/4, dem bisherigen Literaturwert zur Beschreibung des Niedrigdruckverhaltens. Der Vergleich mit Messwerten aus der Literatur bei höheren Drücken suggeriert einen kontinuierlichen Anstieg des Exponenten mit dem Druck, vergleichbar mit dem Befund zum Verhalten zweidimensionaler Systeme in der Literatur. In der vorliegenden Auswertung zeigt sich, dass die logarithmische Ableitung des Exponenten über mindestens 5 Größenordnungen des Drucks konstant ist.

Bei den höchsten Amplituden zeigt sich ein Abfall der Geschwindigkeit der Wellenfront mit steigender Amplitude für p_0 zwischen 100 und 400 Pa, ein Anzeichen für elastichen Festigkeitsabfall, während zwischen 20 und 50 Pa eine steigende Geschwindigkeit der Wellenfront sichtbar wird, ein Anzeichen für Schockwellen-artiges Verhalten. Die Dämpfung der Wellenfront ist bei den höchsten Amplituden erhöht - in Übereinstimmung mit bekannten Resultaten für Schockwellen in Glaskugelpackungen am Boden.

Zur weiteren Untersuchung der Wellenausbreitung jenseits der Theorie des effektiven Mediums und zur Untersuchung möglicher großer Korrelationslängen die in Zusammenhang mit Anisotropie und Verlust der mechanischen Rigidität (engl. 'unjamming') stehen, wurden Versuche zur Mehrfachstreuung elastischer Wellen bei Bodenmessungen mit $p_0 \propto 1$ kPa durchgeführt. In Messungen der Konfigurations-gemittelten inkohärenten Intensität im diffusen Bereich zeigte sich eine mittlere freie Weglänge des Transports zwischen 1,6 und 1,8 Kugeldurchmessern im Falle kleiner Probenhöhe mit einem moderaten hydrostatischen Gradienten sowie ungefähr 5 Kugeldurchmessern im Falle einer größeren Probe mit deutlich größerem Gradienten. Vergleichbare Werte nimmt die mittlere freie Weglänge

der Streuung an, die aus der Dämpfung des koheränten Signals bei verschiedener Probendicke bestimmt wurde. Diese Resultate sind größer als Literaturwerte, gemessen bei wesentlich höherem Druck, bei welchem der hydrostatische Gradient vernachlässigbar ist.

Schließlich wurden Dekonvolutions- und Zeitumkehr-Techniken in einem Aufbau aus zwei Wandlern verwendet um Wellenfokussierung zu messen, um diese als Methode zur Messung mikroskopischer Umordnungen in der Granulatpackung unter externer Anregung zu testen.

Acknowledgements / Danksagung

Here I would like to thank the various people who helped making my PhD thesis possible:

I thank my supervisor Prof. Matthias Sperl and leader of the granular group at DLR for giving me the opportunity to pursue this work and conduct related experiments in the various microgravity environments.

Thanks to Christoph Dreißigacker, the engineer at DLR who not only made GRASCHA flight-worthy but managed the difficult but highly successful sounding rocket campaign in Kiruna with many experiments from our institute.

Special thanks to the engineering students who contributed to the development of granular sound instruments at our institute, especially Alberto Chiengue Tchapnda without whom no GRASCHA rocket module would exist, also Alex Kamphuis and Antoine Micallef, who worked on previous campaigns involving parabolic flight experiments.

A big thank you to Dr. Peidong Yu for proof-reading as well as many in-depth discussions about my work and the experience and knowledge he shared with me based on his previous work on granular sound, a field of research which he introduced at DLR many years ago.

Thanks to the team at the DLR workshop who flawlessly manufactures the required parts for experiments.

Thanks to Dr. Till Kranz for proof-reading and many scientific discussions.

Thanks to Dr. Juan Petit, Dr. Olivier Coquand, Dr. Koray Önder, Dr. Philip Born, Dr. Jan Haeberle, Dr. Nishant Kumar and Dr. Sebastian Pitikaris for interesting scientific discussions. Further thanks to the other current and former members of the granular group, such as Dr. Masato Adachi, Dr. Ali Kaouk, Dr. Miranda Fateri, Dr. Alexandre Meurisse, Olfa Lopez, Merve Seckin-Krüger and many others for further interesting discussions. You made the time at DLR worthwhile and never boring. This also involved many unbelievable kicker games which shall be remembered.

Ich möchte meinen Eltern Alfred und Olympia dafür danken, dass sie mir die Voraussetzungen für ein gutes Leben geschaffen haben und mir von klein auf eine Begeisterung für Wissenschaft und Bildung vermittelt haben. Ihnen, speziell meinem Vater, der das Ergebnis dieser Arbeit leider nicht mehr zu sehen bekommen kann, sei diese Arbeit gewidmet.

Contents

1. List of Figures

List of Abbreviations

DLR	Deutsches Zentrum für Luft- und Raumfahrt (German Aerospace Center)
EMT	Effective Medium Theory
GRASCHA	Granular Sound Characterization experiment / Granulat Schall Experiment
MAPHEUS	Materialphysikalische Experimente unter Schwerelosigkeit (material physics experiments at zero gravity)
ZARM	Zentrum für angewandte Raumfahrttechnologie und Mikrogravitation Center of Applied Space Technology and Microgravity
AWG	Arbitraty Waveform Generator
FFT	Fast Fourier Transform
NUC	Next Unit of Computing (mini-pc by Intel, used in **Grascha**)
SOE	Start of Experiment (signal that indicates the start of the microgravity period)
SODS	(signal that enables the on-board power-supply)
SCP	Secure Copy Protocol
SSH	Secure Shell

List of Symbols

$\mathbf{i}$	$\sqrt{-1}$, unless used as an index, which will be obvious
$\mathbf{c_p}$ and $\mathbf{c_s}$	longitudinal / P-wave sound speed and transverse / S-wave sound speed
$\mathbf{p_0}$ and $\mathbf{p_i}$	static / confinement pressure and dynamic pressure
$\mathbf{a_m}$	geometric mean of peak acceleration of two sensors
$\mathbf{Z}$	mean contact/coordination number
ϕ	volume ratio
λ and μ	(effective) Lamé moduli, unless λ is used for the wavelength
ρ	(bulk material) density
$\mathbf{u}(\mathbf{x},\mathbf{t})$	displacement
$\varepsilon_{\mathbf{ij}}(\mathbf{x},\mathbf{t})$	infinitesimal strain tensor
$\sigma_{\mathbf{ij}}(\mathbf{x},\mathbf{t})$	Cauchy stress tensor
$\epsilon_{\mathbf{ijk}}$	Levi-Civita symbol
$\Psi(\mathbf{x},t)$	(vector-valued) wave function derived from $\mathbf{u}(\mathbf{x},t)$ and $\varepsilon_{ij}(\mathbf{x},t)$
$\mathbf{H}(\mathbf{x})$ and $\delta\mathbf{H}(\mathbf{x})$	time-evolution operator and random inhomogeneity / perturbation operator
$\ell_{\mathbf{c}}$	correlation length
$\ell_{\mathbf{s}}$	scattering mean free path
$\ell_{\mathbf{T}}$	transport mean free path
$\tau_{\mathbf{a}}$	inelastic absorption time
$\mathbf{Q}$	quality factor
ω	angular frequency, or center frequency
Ω	modulation angular frequency
$\mathbf{k_0}$	$= \omega/c$, wave-number in long-wavelength limit of homogeneous wave-equation
$\Sigma(\omega)$	self-energy at angular frequency ω (if no dependence on ω or k_0: then it is used to indicate a sum)

Introduction

Systems of discrete particles of sufficient mass and size, such that no Brownian motion is observed, which are interacting with dissipative forces, such that they come to rest unless externally driven, are referred to as 'granular'[1, 2].

Granular matter is known for having unusual properties that are a currently active field of research. For example, granular gasses show unconventional damping behavior[3] and negative heat capacity[4]. But even when granular material is brought to rest and confined to a volume under pressure, nontrivial behavior can still be found: elastic waves, which propagate through an effective medium[5, 6, 7] provided by the elastic response of the packing in the long wavelength limit, propagate linearly until they are scattered and attenuated by disorder[8], affected slowed down or broadened by dispersion[9] or distorted by demodulation and frequency-mixing at nonlinear contacts[10]. At vanishing confinement pressure, solitons[11, 12] and shock-waves [13, 14] are found. For high frequencies, where the wavelength is comparable to the particle diameter, multiple scattering and diffusive transport is found[15, 16]. At lower frequencies, when the density of state is examined, a cross-over from Debye-like increase to a plateau is found at a characteristic frequency that increases with pressure[17, 18] and implies a diverging length scale at the jamming point.

In this thesis, elastic wave propagation in granular matter beyond effective medium theory is examined by experiments in glass bead packings at low confinement pressure.

In chapter 1 an overview of wave phenomena in granular matter is given, introducing linear waves, dispersion, parametric mixing and demodulation, solitons and scattering, first in the granular chain, later addressing the three-dimensional packing.

In chapter 2 the GRAnular Sound CHAracterization or GRASCHA experiment is presented, as recently published[19]. Measurement results from a sounding rocket campaign in 2019 are shown, which probe linear and nonlinear elastic waves in glass bead packings at low confinement pressure. A universal pressure dependence of the sound speed is suggested.

In chapter 3 measurements of multiply scattered elastic waves are shown. First, the incoherent intensity in ensembles of macroscopically equivalently prepared packings is investigated. Then, the coherent attenuation is measured. Finally, wave focussing techniques are tested.

In chapter 4 an overall conclusion is given.

Bibliography

[1] Heinrich M Jaeger and Sidney R Nagel. Physics of the granular state. *Science*, 255(5051):1523–1531, 1992.

[2] Heinrich M Jaeger, Sidney R Nagel, and Robert P Behringer. Granular solids, liquids, and gases. *Reviews of modern physics*, 68(4):1259, 1996.

[3] Marcus N Bannerman, Jonathan E Kollmer, Achim Sack, Michael Heckel, Patric Mueller, and Thorsten Pöschel. Movers and shakers: Granular damping in microgravity. *Physical Review E*, 84(1):011301, 2011.

[4] Nikolai V Brilliantov, Arno Formella, and Thorsten Pöschel. Increasing temperature of cooling granular gases. *Nature communications*, 9(1):1–9, 2018.

[5] Jacques Duffy and R.D. Mindlin. Stress-strain relation and vibrations of a granular medium. *J. Appl. Mech., ASME*, 24:585–593, 1957.

[6] P. J. Digby. The effective elastic moduli of porous granular rocks. *J. Appl. Mech.*, 48(4):803, 1981.

[7] K. Walton. The effective elastic moduli of a random packing of spheres. *J. Mech. Phys. Solids*, 35(2):213 – 226, 1987.

[8] O Mouraille and Stefan Luding. Sound wave propagation in weakly polydisperse granular materials. *Ultrasonics*, 48(6-7):498–505, 2008.

[9] Christophe Coste and Bruno Gilles. Sound propagation in a constrained lattice of beads: High-frequency behavior and dispersion relation. *Phys. Rev. E*, 77:021302, Feb 2008.

[10] V Tournat, VE Gusev, and B Castagnede. Self-demodulation of elastic waves in a one-dimensional granular chain. *Physical Review E*, 70(5):056603, 2004.

[11] VF Nesterenko. Propagation of nonlinear compression pulses in granular media. *J. Appl. Mech. Tech. Phys. (Engl. Transl.)*, 24(5):733–743, 1983. Translated from Zhurnal Prikladnoi Mekhaniki i Tekhnicheskoi Fiziki, No. 5, pp. 136-148, September-October, 1983.

[12] C. Daraio, V. F. Nesterenko, E. B. Herbold, and S. Jin. Strongly nonlinear waves in a chain of teflon beads. *Phys. Rev. E*, 72:016603, Jul 2005.

[13] Leopoldo R. Gómez, Ari M. Turner, Martin van Hecke, and Vincenzo Vitelli. Shocks near jamming. *Phys. Rev. Lett.*, 108:058001, Jan 2012.

[14] Siet van den Wildenberg, Rogier van Loo, and Martin van Hecke. Shock waves in weakly compressed granular media. *Phys. Rev. Lett.*, 111:218003, Nov 2013.

[15] X. Jia. Codalike multiple scattering of elastic waves in dense granular media. *Phys. Rev. Lett.*, 93:154303, Oct 2004.

[16] XiaoPing Jia, J Laurent, Yacine Khidas, and Vincent Langlois. Sound scattering in dense granular media. *Chinese Science Bulletin*, 54(23):4327–4336, 2009.

[17] Leonardo E Silbert, Andrea J Liu, and Sidney R Nagel. Vibrations and diverging length scales near the unjamming transition. *Physical review letters*, 95(9):098301, 2005.

[18] Eli T Owens and Karen E Daniels. Acoustic measurement of a granular density of modes. *Soft Matter*, 9(4):1214–1219, 2013.

[19] Karsten Tell, Christoph Dreißigacker, Alberto Chiengue Tchapnda, Peidong Yu, and Matthias Sperl. Acoustic waves in granular packings at low confinement pressure. *Review of Scientific Instruments*, 91(3):033906, 2020.

1. Theory of Elastic Waves in Granular Matter

1.1. Introduction

As a stating point for this thesis, a brief theoretical introduction is given to show the various elastic wave phenomena encounterd in granular media. Some instructive calculations and references to the relevant literature are provided. In section 1.2 linear wave propagation, dispersion, weakly-nonlinear effects and solitons are introduced as well as multiple scattering. This is done in a one-dimensional system, the granular chain, which is convenient for calculations and already shows many aspects of the behaviour of granular packings qualitatively. In section 1.3 the three-dimensional case is intruduced, which is more relevant for the experiments in this thesis.

1.2. The Linear Chain

1.2.1. Homogeneous, Free Chain in the Continuum Limit

To demonstrate how wave-like behavior can arise in a granular medium, let us first consider a linear chain of N particles within total length L. Each particle of index i at position x_i has a mass m_i and is interacting with its neighbor at i+1 through a linear spring of stiffness k_i and similarly with its neighbor at i-1 through a spring of stiffness k_{i-1}. The behavior at i=0 and i=N depends on the boundary conditions, which can represent open chains with fixed positions (Dirichlet) or velocities (Neumann) of the particles at the ends or closed chains (periodic boundary conditions). To simplify the calculations in this introductory example we choose the latter and will address the other cases in later chapters when appropriate. Hence, here we let $k_{i-N} = k_i$ as well as $m_{i-N} = m_i$ and $x_{i-N} = x_i$. In the simplest case $k_i = const. = k$ and $m_i = const. = m$. Then in the ground state all particles are evenly spaced at $x_i = i \cdot L/N$ and Newton's equations of motion[1] are given by:

$$m_i \frac{\mathrm{d}^2}{\mathrm{d}t^2} x_i = k \cdot ((x_{i+1} - x_i - L/N) - (x_i - x_{i-1} - L/N)) \tag{1.1}$$

We can express (1.1) in terms of the particle displacement $u_i = x_i - i \cdot L/N$:

$$m_i \frac{\mathrm{d}^2}{\mathrm{d}t^2} u_i = k \cdot (u_{i+1} + u_{i-1} - 2 \cdot u_i) \tag{1.2}$$

Even though the system is discrete, we can always describe the displacement by a continuous function $u(x,t)$ that fulfills $u(x_i,t) = u_i(t)$. Let us assume u varies on a characteristic length scale λ. Then it is convenient to write $u(x,t) = u(x_i + \lambda \cdot \xi, t) = \widetilde{u}(\xi,t)$ with the normalized distance $\xi = \Delta x/\lambda$ relative to any point x_i. Let $\widetilde{u}(\xi,t)$ be an analytic function of ξ with $\widetilde{u}(0,t) = u(x_i,t)$. Then, for any arbitrary fixed x_i

$$u(x,t) = \widetilde{u}(\xi,t) = u(x_i,t) + \left.\frac{\partial \widetilde{u}}{\partial \xi}\right|_{\xi=0} \cdot \xi + \frac{1}{2} \left.\frac{\partial^2 \widetilde{u}}{\partial \xi^2}\right|_{\xi=0} \cdot \xi^2 + \mathcal{O}\left(|\xi|^3\right) \tag{1.3}$$

If we choose $\lambda \cdot \xi = L/N$ then (1.2) can be written in terms of $\widetilde{u}(\xi,t)$ at any x_i:

$$m_i \frac{\partial^2}{\partial t^2} u(x_i,t) = k \cdot (\widetilde{u}(\xi,t) - u(x_i,t) + \widetilde{u}(-\xi,t) - u(x_i,t)) \tag{1.4}$$

After inserting (1.3) in (1.4) we arrive at:

$$\begin{aligned} m_i \frac{\partial^2}{\partial t^2} u(x_i,t) =& k \cdot [\\ & u(x_i,t) + \frac{\partial \widetilde{u}}{\partial \xi} \cdot \xi + \frac{1}{2} \frac{\partial^2 \widetilde{u}}{\partial \xi^2} \cdot \xi^2 - u(x_i,t) \\ & + u(x_i,t) + \frac{\partial \widetilde{u}}{\partial \xi} \cdot (-\xi) + \frac{1}{2} \frac{\partial^2 \widetilde{u}}{\partial \xi^2} \cdot \xi^2 - u(x_i,t) + \mathcal{O}\left(|\xi|^3\right) \\ &] = k \cdot \left(\frac{\partial^2 \widetilde{u}}{\partial \xi^2} \cdot \xi^2 + \mathcal{O}\left(|\xi|^3\right) \right) \end{aligned} \tag{1.5}$$

If λ is large compared to the inter-particle distance we can neglect terms of higher orders in ξ. Then we use $\partial_\xi \widetilde{u} = \lambda \cdot \partial_x u$ and divide (1.5) by the inter-particle distance L/N. After introducing the 1-dimensional mass-density $\rho = m \cdot N/L$ and elastic modulus $\mu = k \cdot L/N$ we get:

$$\rho \frac{\partial^2 u}{\partial t^2} = \mu \frac{\partial^2 u}{\partial x^2} \tag{1.6}$$

Or, after introducing $c = \sqrt{\frac{\mu}{\rho}}$:

$$\frac{\partial^2 u}{\partial t^2} = c^2 \frac{\partial^2 u}{\partial x^2} \tag{1.7}$$

This is a wave equation for the displacement $u(x,t)$. It describes a longitudinal wave travelling at phase speed c. It is valid in the long wavelength limit.

Equation (1.7) is a second-order partial differential equation in time and space for a scalar function. It is equivalent to a first-order equation for a two-component vector-valued function. Thus, similarly to a more general treatment of three-dimensional elastic waves known in the literature[2, 3] that will be used in later sections, we define

$$\Psi(x,t) = \begin{pmatrix} \sqrt{\frac{\rho}{2}} \frac{\partial}{\partial t} u \\ \sqrt{\frac{\mu}{2}} \frac{\partial}{\partial x} u \end{pmatrix} \tag{1.8}$$

and the prefactors are chosen such that we can interpret the squared magnitude as the elastic energy density:

$$\int_0^L |\Psi(x,t)|^2 \, \mathrm{d}x = \int_0^L \Psi^*(x,t) \cdot \Psi(x,t) \mathrm{d}x = \int_0^L \frac{\rho}{2} \left(\frac{\partial u}{\partial t} \right)^2 + \frac{\mu}{2} \left(\frac{\partial u}{\partial x} \right)^2 \mathrm{d}x = E_{total} \tag{1.9}$$

Then Ψ satisfies the classical Schrödinger equation

$$i\frac{\partial}{\partial t}\Psi(x,t) = \mathbf{H}\Psi(x,t) \tag{1.10}$$

$$\text{with } \mathbf{H} = ic\frac{\partial}{\partial x}\begin{pmatrix}0 & 1\\ 1 & 0\end{pmatrix} \tag{1.11}$$

where $i = \sqrt{-1}$. First of all, we notice that inserting Ψ, as defined in (1.8), in (1.10) immediately leads to (1.6). Then we use that (1.6) has plane wave solutions of the form

$$u_k(x,t) = a_k \cdot \cos(kx - \omega_k t) + b_k \cdot \sin(kx - \omega_k t) \tag{1.12}$$

$$= a_k \cdot \mathrm{Re}\left(\mathrm{e}^{ikx - i\omega_k t}\right) + b_k \cdot \mathrm{Im}\left(\mathrm{e}^{ikx - i\omega_k t}\right) \tag{1.13}$$

with the dispersion relation

$$\omega_k^2 = c^2k^2 \text{or } \omega_k = c\,|k| \tag{1.14}$$

Accordingly, (1.10) has a solution

$$\Psi_k(x,t) = \sqrt{\frac{\rho}{2}}\mathrm{e}^{ikx - i\omega_k t}\begin{pmatrix}-i\omega_k\\ ick\end{pmatrix} \tag{1.15}$$

which also solves the eigenvalue equation

$$\mathbf{H}\Psi_k = \omega_k\Psi_k \tag{1.16}$$

with degenerate eigenvalues $\omega_k = \omega_{-k}$. Any $u(x,t)$ that solves (1.6) can be written as linear combination of $u_k(x,t)$ and any Ψ that solves (1.10) can similarly be written as linear combination $\Psi = \sum_{j=0}^{N} a_j\Psi_{k_j}$ with complex coefficients a_j. Therefore we can apply the operator $\mathbf{H}$ on any Ψ by writing it in terms of the eigenfunctions Ψ_k of $\mathbf{H}$:

$$\mathbf{H}\Psi = \sum_{j=0}^{N} a_j\mathbf{H}\Psi_{k_j} = c\sum_{j=0}^{N} a_j\omega_{k_j}\Psi_{k_j} \tag{1.17}$$

Finally, we consider a monochromatic wave with the displacement $u(x,t) = v(x)e^{-i\omega_k t}$ and the corresponding wave function:

$$\Psi_k(x,t) = \sqrt{\frac{\rho}{2}}\mathrm{e}^{-i\omega_k t}\begin{pmatrix}-i\omega_k\\ c\frac{\partial}{\partial x}\end{pmatrix}v(x) \tag{1.18}$$

By inserting (1.18) in (1.10) and using $\omega_k^2/c^2 = k^2$ we arrive at:

$$\left(\frac{\partial^2}{\partial x^2} + k^2\right)v(x) = 0 \tag{1.19}$$

This equation for the space-dependent part $v(x)$ is called the Helmholtz equation.

1.2.2. Homogeneous, Driven Chain in the Continuum Limit

So far no external forces were taken into account. To consider them, we have to include a driving force $\Psi_f(x,t)$ in the wave equation:

$$\left(i\frac{\partial}{\partial t} - \mathbf{H}\right)\Psi(x,t) = \Psi_f(x,t) \tag{1.20}$$

$$\text{with } \Psi_f(x,t) = \begin{pmatrix} \frac{1}{\rho} f(x,t) \\ 0 \end{pmatrix} \tag{1.21}$$

This inhomogeneous equation can be solved by convolution of Ψ_f with a Green's function $G(x,x';t,t')$:

$$\Psi(x,t) = \int_0^L G(x,x';t,t')\Psi_f(x',t')\mathrm{d}x' \tag{1.22}$$

The Green's function shall be invariant upon translations in time and space $G(x,x';t,t') = G(x-x',t-t')$. The latter will be valid only in the long-wavelength limit i.e. when the finite particle spacing can be neglected. Furthermore, $G(t-t') \stackrel{!}{=} 0$ for $t < t'$ to ensure causality i.e. effects cannot precede their causes.

To obtain G we start by demanding it solves the inhomogeneous equation for a point-like driving:

$$\left(i\frac{\partial}{\partial t} - \mathbf{H}\right)G(x,t) = \delta(x)\delta(t) \tag{1.23}$$

Equations of this type (1.23) are conveniently solved after applying a suitable integral transformation, such as a Laplace- or Fourier-transform, which provides us an algebraic equation equivalent to the partial differential equation in the time- and direct space domain. For this purpose we define the Fourier-transform as

$$\mathcal{F} : f(t) \mapsto F(\omega) = \int_{-\infty}^{\infty} f(t)\mathrm{e}^{-i\omega t}\mathrm{d}t \tag{1.24a}$$

$$\mathcal{F} : f(x) \mapsto F(k) = \int_{-\infty}^{\infty} f(x)\mathrm{e}^{ikx}\mathrm{d}x \tag{1.24b}$$

$$\mathcal{F}^{-1} : F(\omega) \mapsto f(t) = \frac{1}{2\pi}\int_{-\infty}^{\infty} F(\omega)\mathrm{e}^{i\omega t}\mathrm{d}\omega \tag{1.24c}$$

$$\mathcal{F}^{-1} : F(k) \mapsto f(x) = \frac{1}{2\pi}\int_{-\infty}^{\infty} F(k)\mathrm{e}^{-ikx}\mathrm{d}k \tag{1.24d}$$

Then, the Fourier-transform of (1.23) in terms of time and space is:

$$\left(-\omega + ck\begin{pmatrix} 0 & 1 \\ 1 & 0 \end{pmatrix}\right)G(k,\omega) = 1 \tag{1.25}$$

After inversion of the matrix representing the sum on the left side we get:

$$G(k,\omega) = \frac{-\begin{pmatrix} \omega & ck \\ ck & \omega \end{pmatrix}}{(\omega - ck)(\omega + ck)} \tag{1.26}$$

To get the time-domain representation of (1.26) we wish to apply the inverse Fourier-transform. However, this would involve integration over two poles of first order at $\omega = \pm ck$. To get any meaningful result, we have to regularize this integral. The choice of the regularization method will determine the causal properties of the Green's function.

First of all, we define the analytic continuation of $G(\omega)$ as $G(z) = G(\omega + i\nu)$. Then we add a small imaginary part $i\varepsilon$ to the position of each pole, which we will later remove by taking the limit $\varepsilon \to 0$:

$$G(z) = \frac{-\begin{pmatrix} z & ck \\ ck & z \end{pmatrix}}{(z - ck - i\varepsilon)(z + ck - i\varepsilon)} \tag{1.27}$$

Then we consider the complex path integral $\oint_\Gamma G(z)dz$ along two possible contours Γ_+ and Γ_- as indicated in figure (1.1). Both contours include the interval $[-r;r]$ on the real axis. Γ_+ is closed by the half-circle $\phi \mapsto re^{i\phi}$ in the upper complex half-plane while Γ_- is closed by the half-circle $\phi \mapsto re^{-i\phi}$ in the lower half-plane.

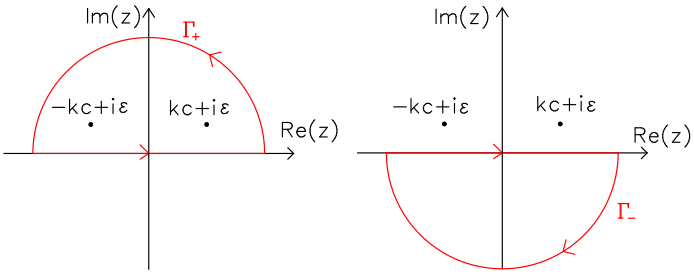

Figure 1.1.: *Two possible integration contours Γ_+ and Γ_- incorporating the real axis, either closed in the upper half-plane including both poles or closed in the lower half-plane without any poles.*

Now we can write the regularized Fourier integral as:

$$G(k,t) = \lim_{\varepsilon\to 0}\lim_{r\to\infty} \frac{-1}{2\pi} \oint_\Gamma \frac{\begin{pmatrix} z & ck \\ ck & z \end{pmatrix} e^{izt}}{(z - ck - i\varepsilon)(z + ck - i\varepsilon)} \mathrm{d}z \quad \text{with} \quad \Gamma = \begin{cases} \Gamma_+ \text{ for } t > 0 \\ \Gamma_- \text{ otherwise} \end{cases} \tag{1.28}$$

With $\nu = \mathrm{Im}(z) = r \cdot \sin(\phi)$ we can write the complex exponential factor

$$e^{izt} = e^{i\omega t} e^{-rt\sin(\pm\phi)} \xrightarrow{r\to\infty} \begin{cases} 0 \text{ for } t > 0 \text{ using } \Gamma_+ \\ 0 \text{ otherwise, using } \Gamma_- \end{cases} \tag{1.29}$$

With this choice of integration contours we can therefore ensure that, in the limit of infinitely large half-circles, only the real-axis interval contributes to the integral. On the other hand, the integral along each of the closed paths Γ_+ and Γ_- can be calculated using Cauchy's residue theorem. First, we notice that Γ_- does not include any poles thus the corresponding integral vanishes. Then, for Γ_+ we have contributions due to both poles in the upper half-plane:

$$\begin{aligned}
&\oint_{\Gamma_+} \frac{\begin{pmatrix} z & ck \\ ck & z \end{pmatrix} \mathrm{e}^{izt}}{(z-ck-i\varepsilon)(z+ck-i\varepsilon)} \mathrm{d}z = 2\pi i \left(\operatorname*{Res}_{z=ck+i\varepsilon} (\ldots) + \operatorname*{Res}_{z=-ck+i\varepsilon} (\ldots) \right) \\
&= 2\pi i \left(\frac{\begin{pmatrix} ck+i\varepsilon & ck \\ ck & ck+i\varepsilon \end{pmatrix} \mathrm{e}^{ickt-\varepsilon t}}{2ck} + \frac{\begin{pmatrix} -ck+i\varepsilon & ck \\ ck & -ck+i\varepsilon \end{pmatrix} \mathrm{e}^{-ickt-\varepsilon t}}{-2ck} \right) \\
&\xrightarrow{\varepsilon\to 0} \pi i \begin{pmatrix} \mathrm{e}^{ickt} - \mathrm{e}^{-ickt} & \mathrm{e}^{ickt} + \mathrm{e}^{-ickt} \\ \mathrm{e}^{ickt} + \mathrm{e}^{-ickt} & \mathrm{e}^{ickt} - \mathrm{e}^{-ickt} \end{pmatrix} = -2\pi \begin{pmatrix} \sin(ckt) & -i\cos(ckt) \\ -i\cos(ckt) & \sin(ckt) \end{pmatrix}
\end{aligned} \tag{1.30}$$

Finally, by inserting (1.30) in (1.28) and applying the inverse Fourier transform we get:

$$G^+(x,t) = \int_{-\infty}^{\infty} \begin{pmatrix} \sin(ckt) & -i\cos(ckt) \\ -i\cos(ckt) & \sin(ckt) \end{pmatrix} e^{-ikx} \mathrm{d}k \cdot \Theta(t) \tag{1.31}$$

By using (1.31 and (1.15) one can easily verify that

$$\int_0^L G^+(x-x',t-t')\Psi_k(x',t')\mathrm{d}x' = \Psi_k(x,t) \;\text{ for }\; t > t' \tag{1.32}$$

$G^+(x,t-t')$ is called the retarded or causal Green's function. Due to (1.32) it is also a propagator. If we use it to solve the inhomogeneous equation (1.22) then its solution at time t describes the emission of a wave originating from an excitation that occurred at a previous time t'. Analogously we could derive the advanced or anti-causal Green's function $G^-(x,t-t')$ by shifting the poles from $\pm ck + i\varepsilon$ to $\pm ck - i\varepsilon$ and switching the roles of Γ_+ and Γ_-. Then, using $G^-(x,t-t')$ we would arrive at a solution of (1.22) describing a wave at time t that is absorbed by a sink or receiver at a later time t'.

1.2.3. High-Frequency Behavior in the Monodisperse Chain

The results from the previous section describe wave propagation in the long wavelength limit $\lambda \gg d$. If we take into account the finite inter-particle distance given by the particle diameter d, we will encounter dispersion at $\lambda \propto d$. The solutions for a linear wave equation of the displacement field $u(x,t)$ with a periodic potential $V(x) = V(x+d)$ are Bloch waves[4]:

$$u(x,t) = \mathrm{e}^{ikx - i\omega t} v(x) \tag{1.33}$$

where $v(x+d) = v(x)$ has the periodicity of the chain. Under discrete translations of d, the displacement is invariant up to a phase-shift:

$$u(x+d,t) = \mathrm{e}^{ikd} u(x,t) \tag{1.34}$$

As the wave equation (1.7) is not valid for short wavelengths, we have to use the equations of motion (1.2) that take into account the particle spacing d and the restoring force at each particle site x_i. After inserting (1.33) in (1.2) we arrive at:

$$-m\omega^2 \mathrm{e}^{ikx-i\omega t} v(x) = K\left(\mathrm{e}^{ikd} + \mathrm{e}^{-ikd} - 2\right) \mathrm{e}^{ikx-i\omega t} v(x) \tag{1.35}$$

We note that by using periodic boundary conditions $u(x_{i+N}) = u(x_i)$ for the displacement at all particle sites and $u(x+N\cdot d) = u(x)$ for the continuous displacement field everywhere we can avoid special treatment of the ends of the chain. The equation is simplified to:

$$\begin{aligned} \omega^2 &= \frac{2K}{m}\left(\cos(kd) - 1\right) \\ &= \frac{4K}{m}\sin^2\left(\frac{kd}{2}\right) \end{aligned} \tag{1.36}$$

As a result, the frequency ω is given by the positive square root:

$$\begin{aligned} \omega &= \sqrt{\frac{4K}{m}}\sin\left(\frac{kd}{2}\right) \\ &= \frac{2}{d}\sqrt{\frac{\mu}{\rho}}\sin\left(\frac{kd}{2}\right) \end{aligned} \tag{1.37}$$

$$\xrightarrow{kd \ll 1} k\sqrt{\frac{K}{m}} = kc \tag{1.38}$$

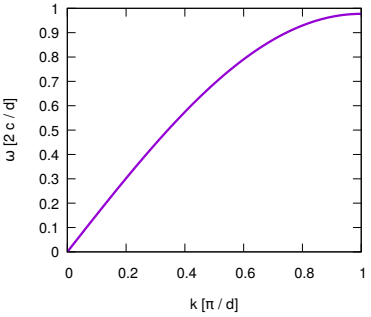

Figure 1.2.: *Dispersion in a linear chain according to Eq. (1.36)*

The dispersion relation is plotted in Fig. 1.2. As we can see, the linear dispersion (1.14) is recovered in the long wavelength limit whereas we get different behavior at short wavelengths that leads us to the definition of two distinct wave speeds: the phase velocity $v_\phi = \omega/k$ that relates the phase difference to the propagated distance Δx during time Δt by

$$\delta\phi = \omega\Delta t = \omega\Delta x/v_\phi \tag{1.39}$$

and the group velocity

$$v_G = \frac{d\omega}{dk} = \Delta x\frac{d\omega}{d\phi} \tag{1.40}$$

which is the speed at which the envelope of a modulated wave propagates. At $k = \pi/d$ or $\lambda = 2d$ we reach the cut-off angular frequency $\omega_c = 2\sqrt{K/m} = 2c/d$ or cut-off frequency $f_c = c/(\pi d)$. At f_c the group velocity is zero and the phase velocity is at its minimum. No propagating (energy-transporting) wave exists for $f > f_c$.

1.2.4. Bidisperse Chain: Bandgaps and Optical Modes

Now, two different species of beads of radii R_1, R_2 and masses m_1, m_2 are arranged in alternating order into a linear chain and connected with springs of stiffness K. Then Newton's equations of motion for the i-th particle are:

$$\begin{aligned} m_1\frac{\mathrm{d}^2x_i^{(1)}}{\mathrm{d}t^2} &= K(x_{i-1}^{(2)} - x_i^{(1)} + x_i^{(2)} - x_i^{(1)}) \\ m_2\frac{\mathrm{d}^2x_i^{(2)}}{\mathrm{d}t^2} &= K(x_i^{(1)} - x_i^{(2)} + x_{i+1}^{(1)} - x_i^{(2)}) \end{aligned} \tag{1.41}$$

where the uppercase index denotes the particle species and the lowercase denotes the unit cell such that in the ground state $x_i^{(2)} - x_i^{(1)} = a$ and $x_{i+1}^{(j)} = x_i^{(j)} + a$ with lattice constant $a = 2\cdot(R_1 + R_2)$. Analogous to section 1.2.1 we define the displacement of each particle as $u_i^{(j)} = x_i^{(j)} - i\cdot a$ and introduce the continuous displacement fields $u^{(j)}(x)$ which satisfy $u^{(j)}(x_i^{(j)}) = u_i^{(j)}$. Then Newton's equations (1.41) are equivalent to:

$$\begin{aligned} \frac{1}{K}\frac{\partial^2}{\partial t^2}u^{(1)}(x,t) &= \frac{1}{m_1}\left(u^{(2)}(x,t) + u^{(2)}(x-a,t) - 2\cdot u^{(1)}(x,t)\right) \\ \frac{1}{K}\frac{\partial^2}{\partial t^2}u^{(2)}(x,t) &= \frac{1}{m_2}\left(u^{(1)}(x,t) + u^{(1)}(x+a,t) - 2\cdot u^{(2)}(x,t)\right) \end{aligned} \tag{1.42}$$

By assuming Bloch wave solutions $u^{(j)}(x) = \mathrm{e}^{ikx}v(x)$ analogous to section 1.2.3 and inserting them into (1.42) we get:

$$-\frac{\omega^2}{K}\begin{pmatrix} u^{(1)} \\ u^{(2)} \end{pmatrix} = \begin{pmatrix} -\frac{2}{m_1} & \frac{1+\mathrm{e}^{-ikd}}{m_1} \\ \frac{1+\mathrm{e}^{ikd}}{m_2} & -\frac{2}{m_2} \end{pmatrix}\begin{pmatrix} u^{(1)} \\ u^{(2)} \end{pmatrix} \tag{1.43}$$

As we can see the mass matrix on the right hand of (1.43) is not diagonal in $u^{(1)}$ and $u(2)$ which is not a surprise since it is particles of alternating species that are interacting. The eigenvalues of this matrix are:

$$\lambda_{1,2} = \left(\frac{1}{m_1} + \frac{1}{m_2}\right) \cdot \left(-1 \pm \sqrt{1 - \frac{4m_1m_2}{(m_1+m_2)^2}\sin^2\left(\frac{ka}{2}\right)}\right) \tag{1.44}$$

After inserting $\lambda_{1,2}$ in (1.43) we arrive at the dispersion relation:

$$\omega = \sqrt{K\frac{m_1+m_2}{m_1m_2}} \cdot \sqrt{1 \pm \sqrt{1 - \frac{4m_1m_2}{(m_1+m_2)^2}\sin^2\left(\frac{ka}{2}\right)}} \tag{1.45}$$

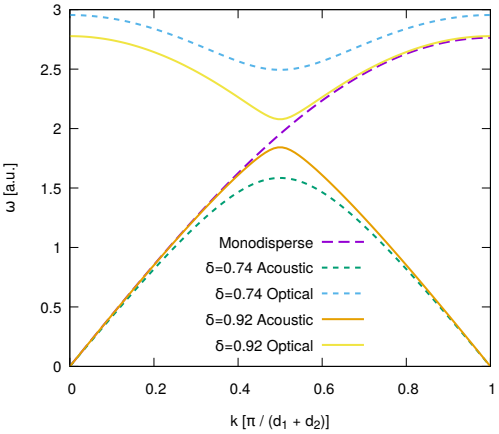

Figure 1.3.: *Dispersion in a linear chain according to Eq. (1.45): bidispersity $\delta = R_2/R_1$ in size leads to emergence of a bandgap between the acoustic and the optical branch. For comparison, the monodisperse case according to Eq. (1.36) is shown (thick dashed line).*

As we can see in (1.45) we get a dispersion relation with two branches. At low frequencies we get behavior as in Eq. (1.36) which is called the acoustic branch as its long wavelength limit describes sound waves in a homogeneous linear medium. The acoustic branch arises from neighboring beads that are oscillating approximately in phase. As the unit cell of our lattice contains two particles, its size is $2 \cdot (R_1 + R_2)$ and the size of the Brillouin zone is $\pi/(R_1 + R_2)$, smaller than the Brillouin zone of a monodisperse chain of either species. If $m_1 > m_2$ then from (1.45) it follows the acoustic cutoff frequency is:

$$\omega_c^{\text{acoustic}} = \sqrt{\frac{2K}{m_1}} \tag{1.46}$$

For higher frequencies, a second branch emerges due to neighboring beads oscillating highly out of phase. This is called the optical branch due to its relation to solid state physics, where it describes the normal modes of oppositely charged ions in a crystal lattice oscillating with opposite phase and thereby

interacting with an electromagnetic wave. In order to treat this as an effective one particle problem, one has to use an effective mass $(1/m_1 + 1/m_2)^{-1}$ to calculate the upper cutoff frequency and the smaller mass m_2 for the lower cutoff frequency of the optical branch:

$$\begin{aligned}\omega_{\text{upper}}^{\text{optical}} &= \sqrt{2K \cdot \left(m_1^{-1} + m_2^{-1}\right)} \\ \omega_{\text{lower}}^{\text{optical}} &= \sqrt{\frac{2K}{m_2}}\end{aligned} \tag{1.47}$$

In Fig. 1.3, a comparison of dispersion relations for particles of size $R_1 = R + \delta R$ and $R_2 = R - \delta R$ for different δR and the monodisperse case is shown. For frequencies between the acoustic cutoff frequency and the lower optical cutoff frequency there is a bandgap. Here, the group velocity v_G is zero and the wavenumber k is purely imaginary. Such modes are called evanescent waves, as their amplitude decays exponentially with distance and they transport no energy. This is also referred to as tunneling, a term more commonly used in quantum mechanics, as it allows the wave to at least partially penetrate a forbidden zone such as a potential barrier of strength greater than the kinetic energy.

Finally we note that despite the qualitatively different dispersion relation, the total number of normal modes is the same as in a monodisperse chain of the same number of beads.

1.2.5. The Hertzian Chain: Linear Waves

Now we consider the contact force between neighboring spherical beads. In the simplest case a sphere is under purely normal load at diametrically opposed contact points and the indentation δ is small enough that the bead retains its spherical shape in good approximation. Then the contact force is given by the Hertz law[5]:

$$F = \sqrt{\frac{4}{9}} \frac{E}{1-\nu^2} \sqrt{R} \delta^{3/2} \Theta(\delta) \tag{1.48}$$

where E is the Young's modulus and ν is the Poisson number of the bead material, R is the sphere radius and $\Theta(\delta) = 1$ if the contact is closed and zero otherwise. Thus, for a known contact force the indentation is:

$$\delta = \left(\frac{9}{4R}\right)^{1/3} \cdot \left(\frac{F \cdot (1-\nu^2)}{E}\right)^{2/3} \tag{1.49}$$

The $F \propto \delta^{3/2}$ force law arises because the contact area increases as the bead is increasingly indented, so additional force is required to maintain the same pressure. A detailed derivation can be found in a textbook[6]. Many nonlinear effects result from this force law. However, approximate linear wave propagation is still possible for pre-compressed chains at static indentation δ_0 if the wave amplitude $\delta(t) - \delta_0$ is very small. Let $\delta(t) = \delta_0 + \delta_1(t)$ with $|\delta_1| \ll \delta_0$. Then the contact force can be expanded in powers of $\xi = \delta_1/\delta_0$:

$$\begin{aligned}F(\delta) &= F(\delta_0) + \xi \cdot \delta_0 \left.\frac{\mathrm{d}F}{\mathrm{d}\delta}\right|_{\delta=\delta_0} + \frac{1}{2}\xi^2 \cdot \delta_0^2 \left.\frac{\mathrm{d}^2F}{\mathrm{d}\delta^2}\right|_{\delta=\delta_0} + \frac{1}{6}\xi^3 \cdot \delta_0^3 \cdot \left.\frac{\mathrm{d}^3F}{\mathrm{d}\delta^3}\right|_{\delta=\delta_0} + \mathcal{O}\left(|\xi|^4\right) \\ &= F(\delta_0) \cdot \left(1 + \frac{3}{2}\xi + \frac{3}{8}\xi^2 - \frac{1}{16}\xi^3 + \mathcal{O}\left(|\xi|^4\right)\right)\end{aligned} \tag{1.50}$$

Linear Waves

We can identify the linear term in (1.50) with the stiffness K:

$$K_{\text{Hertz}} = \frac{E}{1-\nu^2}\sqrt{R\cdot\delta_0} \tag{1.51}$$

For beads made of a material with density ρ we can now calculate the dispersion relation by inserting (1.51) and the bead mass $m = (4\pi/3)\cdot R^3\cdot\rho$ into (1.36) and get

$$\omega = \frac{c_m}{R}\cdot\sqrt{\frac{3}{\pi(1-\nu^2)}}\cdot\left(\frac{\delta_0}{R}\right)^{1/4}\cdot\sin(k\cdot R) \tag{1.52}$$

$$\xrightarrow{k\cdot R\ll 1} k\cdot c_m\cdot\sqrt{\frac{3}{\pi(1-\nu^2)}}\cdot\left(\frac{\delta_0}{R}\right)^{1/4} \tag{1.53}$$

where $c_m = \sqrt{E/\rho}$ is the speed of sound of the bulk material.

For experiments it is often more convenient to express such relations in terms of the contact force which can be measured and adjusted much more accurately than the indentation. Hence, after inserting (1.49) into (1.53) we arrive at the force dependent cutoff frequency:

$$\omega_c = \frac{c_m}{R}\cdot\sqrt{\frac{3}{\pi\cdot(1-\nu^2)}}\cdot\left(\frac{3}{2}\frac{F_0\cdot(1-\nu^2)}{R^2\cdot E}\right)^{1/6} \tag{1.54}$$

Accordingly, the phase and group velocity depend on $(F_0)^{1/6}$.

Weakly Nonlinear Frequency-Mixing and Demodulation

Now we turn our attention to the quadratic term in (1.50). For a real monochromatic wave we let $\xi(t) = |\xi(0)|\cdot\cos(\omega\cdot t)$. Then the quadratic contribution to the contact force is:

$$F^{(2)}(t) = \frac{1}{4}K_{\text{Hertz}}\cdot|\xi(0)|^2\cdot\cos^2(\omega t) = \frac{1}{8}K_{\text{Hertz}}\cdot|\xi(0)|^2\cdot(1+\cos(2\cdot\omega t)) \tag{1.55}$$

As we can see in (1.55), there are two contributions: a constant force and an oscillating term with the doubled frequency. It should be noted that had we replaced the cosine by a sine, the constant term would still have retained the same sign, hence the constant force contribution is always positive.

Another interesting case is the modulated wave $\xi(t) = |\xi(0)|\cdot\cos(\omega t)\cdot\cos(\Omega t)$. We can express it in terms of the sum- and difference frequencies as

$$\xi(t) = \frac{1}{2}|\xi(0)|\cdot(\cos((\omega+\Omega)\cdot t)+\cos((\omega-\Omega)\cdot t)) \tag{1.56}$$

Then the contact force contains the sums and differences of the original sum- and difference frequencies:

$$\frac{F^{(2)}(t)}{|\xi(0)|^2} = \frac{1}{16}K_{\text{Hertz}}\cdot\left(1+\frac{1}{2}\cos(2\cdot(\omega+\Omega)\cdot t)+\frac{1}{2}\cos(2\cdot(\omega-\Omega)\cdot t)+\cos(2\cdot\omega t)+\cos(2\cdot\Omega t)\right) \tag{1.57}$$

Thus, the Hertzian nonlinearity provides a mechanism for mode-conversion and demodulation. An incident high frequency wave with a slowly varying envelope $\Omega \ll \omega$ will be converted to a low frequency wave at $2 \cdot \Omega$. According to (1.57) the amplitude for this process is $16/|\xi(0)|$ times smaller than the amplitude of the linear wave. However, this factor is an upper limit that is only reached if the emmited wave is in phase at all contacts. This is called the phase matching condition. For low enough frequencies there is approximately linear dispersion i.e. $v_\phi(\omega+\Omega) \approx v_\phi(\omega-\Omega)$ hence the phase matching condition is met in a long chain of beads. As the pump frequency $\omega \pm \Omega$ is increased well into the dispersive regime, the number of contacts meeting the phase matching condition and the length fraction of the chain contributing to the coherent emission of the demodulated wave is decreased. The remaining contacts contribute to emission at varying phases, so their contribution is averaged to zero for a long enough chain.

A special case arises for evanescent pump waves: if the pump frequency lies in a bandgap, or simply $\omega \pm \Omega > \omega_c$ in the monodisperse chain, then the wavenumber is imaginary and the amplitude of the incident wave decays exponentially. Thus only one or few beads in the chain contribute to the demodulated wave. Interestingly, while the total demodulation amplitude is small, the demodulation process still gives the leading order contribution for energy transfer into the chain because all higher frequency components are totally reflected back to the source.

Detailed studies of frequency-mixing and demodulation in different frequency regimes can be found in the literature[7].

Strongly Nonlinear Frequency-Mixing and Demodulation

For $|\xi| > 1$ the effect of the Heaviside function in (1.48) has to be considered. In Fig. 1.4 the resulting power density spectra for different ξ are shown. The amplitude of the demodulated or the frequency-doubled contact force experiences a transition from a $|\xi|^2$ dependence at small ξ to a $|\xi|^{3/2}$ dependence at large ξ. One could think of a similar transition in realistic granular material. Existing experimental studies remain inconclusive regarding the high amplitude behavior[8, 9], suggesting that a more detailed treatment of the contact forces be required.

1.2.6. Solitons in the Hertzian Chain

Now we consider nonlinear waves beyond the small amplitude approximation of the previous section. The equation of motion for the i-th sphere in a chain of Hertzian spheres is:

$$\frac{\mathrm{d}^2 u_i}{\mathrm{d}t^2} = \frac{E\sqrt{2R}}{3m(1-\nu^2)} \left((\delta_0 - u_i + u_{i-1})^{3/2} - (\delta_0 - u_{i+1} + u_i)^{3/2} \right) \tag{1.58}$$

Here δ_0 is the static precompression und u_i is the displacement of the sphere at position x_i. As in the previous sections we can introduce the function $u(x)$ in order to discuss the continuum limit of (1.58) for wavelengths $\lambda \gg a$ that are large compared to the bead diameter $a = 2R$. For vanishing precompression $\delta_0 \to 0$ the right-hand side of (1.58) can no longer be written as power-series in the displacement as in the previous section because it would diverge as $\mathcal{O}\left(\left|\frac{1}{\delta_0}\right|\right)$. In this limit, called the sonic vacuum, no linear waves exist. Thus, the full nonlinear equation of motion has to be considered. It was shown by Nesterenko[10] that, in the long-wavelength limit the equation at $\delta_0 = 0$ is given by

$$\frac{\partial^2 u}{\partial t^2} = c^2 \left(\frac{3}{2}\sqrt{-\frac{\partial u}{\partial x}}\frac{\partial^2 u}{\partial x^2} + \frac{a^2}{8}\sqrt{-\frac{\partial u}{\partial x}}\frac{\partial^4 u}{\partial x^4} - \frac{a^2}{8}\frac{\frac{\partial^2 u}{\partial x^2}\frac{\partial^3 u}{\partial x^3}}{\sqrt{-\frac{\partial u}{\partial x}}} - \frac{a^2}{64}\left(\frac{\frac{\partial^2 u}{\partial x^2}}{\sqrt{-\frac{\partial u}{\partial x}}}\right)^3 \right) + \mathcal{O}\left(\left|\frac{a}{\lambda}\right|^3\right) \tag{1.59}$$

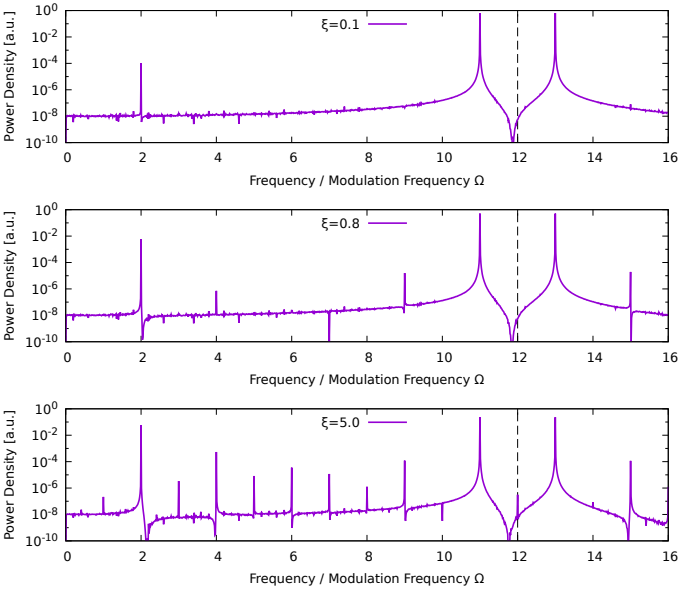

Figure 1.4.: *Numerical calculation of the power density spectrum of the Hertzian contact force for an oscillating indentation at frequency $\omega \pm \Omega$, normalized by the power density at the two incident frequencies. At low amplitude (upper plot) the difference frequency $2 \cdot \Omega$ emerges due to the quadratic term in Eq. (1.50). Increasing the amplitude (center plot) leads to further even multiples of Ω. For very high amplitudes (bottom plot) the contact is opening and closing, which generates also odd multiples of Ω. The vertical dashed line indicates ω.*

,

where we neglect the higher order terms, and it has solitary solutions of the form

$$\xi = \left(\frac{5}{4}\frac{V^2}{c^2}\right)^2 \cos^4\left(\sqrt{10}\frac{x}{5a}\right) \tag{1.60}$$

for $\xi = -\frac{\partial u}{\partial x}$ in the reference frame moving parallel to the soliton at velocity V. This velocity depends on the soliton amplitude such that, at the soliton maximum,

$$\xi_{max} = \left(\frac{5}{4}\frac{V^2}{c^2}\right)^2 \tag{1.61}$$

is satisfied, in contrast to the constant speed of sound found for linear and weakly-nonlinear waves. Remarkably, the spatial width of the soliton $\lambda = \pi \cdot 5a/\sqrt{10} \approx 5a$ depends only on the bead diameter.

Simulations [10] show that, as soon as six particles participate in the wave motion, the soliton reaches a stationary state where a balance of kinetic and potential energy is established, in accordance with the virial theorem of Hertzian particles:

$$\langle E_{kin}\rangle = -\frac{1}{2}\langle \sum_i x_i F_i\rangle \tag{1.62}$$

$$\rightarrow \frac{\langle E_{kin}\rangle}{\langle E_{pot}\rangle} = \frac{5}{4} \tag{1.63}$$

1.2.7. Weak Disorder and Linear Waves

In this section we consider the effect of disorder on linear waves in the long wavelength limit. The treatment of multiple scattering in random media as presented here is established in the literature for acoustic, elastic and electromagnetic waves and, more generally, hyperbolic linear stochastic differential equations[11, 12, 13, 2]. For simplicity, we first consider scattering in the linear chain to give an introduction to the methods which will be later generalized to three-dimensional granular packings in section 1.3.4.

Similar to a method that was previously applied to elastic waves in an inhomogeneous plate[3] and later to granular packings[14], our starting point shall be the classical Schrödinger equation (1.10) from section 1.2.1. The time evolution operator $\mathbf{H}$ in (1.10) depends on "c" which is more explicitly written as $\sqrt{\mu/\rho}$ which we have simply treated as a constant up to this point. Now, we allow both μ and ρ to vary with position. To this end we introduce $\delta\mu(x)$ and $\delta\rho(x)$ as zero centered random processes. Instead of addressing any specific realization of such a process we simply assume it is described by a probability density distribution and its moments, or, equivalently, by its correlation functions. We note that in the special cases $|\delta\mu(x)| \ll |\delta\rho(x)|$ or $|\delta\mu(x)| \gg |\delta\rho(x)|$ or $\delta\mu(x)/\delta\rho(x) = const.$ it is sufficient to consider the resulting $\delta c(x)$ only. Thus $\delta\mathbf{H} = \delta c/c_0 \cdot \mathbf{H}^0$ which is known as the scalar approximation. More generally, $\delta\mu(x)$ and $\delta\rho(x)$ may vary independently and on the same order of magnitude, in which case both contributions to $\delta\mathbf{H}$ must be explicitly taken into account, as I will do in this section. Alternatively, a treatment based on the Helmholtz equation is possible, in which case a perturbation containing both a scalar and an operator-valued potential must be used[15, 16]. The latter approach is briefly covered in appendix E.2.1.

In any case, we assume $|\delta\mathbf{H}| \ll |\mathbf{H}^0|$ with regards to some appropriate norm $|...|$. Then, after averaging over all realizations $\langle\mathbf{H}\rangle = \langle\mathbf{H}^0 + \delta\mathbf{H}\rangle = \langle\mathbf{H}^0\rangle + 0 = \mathbf{H}^0$ we get the ensemble averaged time evolution operator $\mathbf{H}^0$ which in turn can be written in terms of the average density $\langle\rho\rangle = \langle\rho_0 + \delta\rho\rangle = \rho_0$ and stiffness $\langle\mu\rangle = \langle\mu_0 + \delta\mu\rangle = \mu_0$. These average quantities define an effective medium in which the wave propagates in a leading order approximation while the effect of density and stiffness fluctuations shall be addressed by treating $\delta\mathbf{H}$ as a small perturbation.

Coherent Wave

The first goal is to calculate the average Green's function $\langle G(x,t)\rangle$ that determines propagation of the coherent or average wave. As in section 1.2.2 we start with the defining equation for the Green's function. By inserting $\mathbf{H} = \mathbf{H}^0 + \delta\mathbf{H}$ into (1.23) we get:

$$\left(i\frac{\partial}{\partial t} - \mathbf{H}^0\right)\mathbf{G}(x,t) = \delta(x)\delta(t) + \delta\mathbf{H}\mathbf{G}(x,t) \tag{1.64}$$

As in section 1.2.2 it is convenient to switch to the Fourier domain:

$$\left(-\omega + c_0 k \begin{pmatrix} 0 & 1 \\ 1 & 0 \end{pmatrix}\right)\mathbf{G}(\omega,k) = \mathbf{1}_{2x2} + \delta\mathbf{H}\mathbf{G}(\omega,k) \tag{1.65}$$

By multiplying (1.65) from the left with $\mathbf{G}^0$, the Green's function for the equation without $\delta\mathbf{H}$, we get:

$$\mathbf{G}(\omega,k) = \mathbf{G}^0(\omega,k) + \mathbf{G}^0(\omega,k)\delta\mathbf{H}\mathbf{G}(\omega,k) \tag{1.66}$$

Here, $\mathbf{G}(\omega,k)$ is recursively defined such that we can expand the term on the right as:

$$\begin{aligned}\mathbf{G} &= \mathbf{G}^0 + \mathbf{G}^0\delta\mathbf{H}\mathbf{G}^0 + \mathbf{G}^0\delta\mathbf{H}\mathbf{G}^0\delta\mathbf{H}\mathbf{G} \\ &= \mathbf{G}^0 + \mathbf{G}^0\delta\mathbf{H}\mathbf{G}^0 + \mathbf{G}^0\delta\mathbf{H}\mathbf{G}^0\delta\mathbf{H}\mathbf{G}^0 + \mathbf{G}^0\delta\mathbf{H}\mathbf{G}^0\delta\mathbf{H}\mathbf{G}^0\delta\mathbf{H}\mathbf{G} \\ &= \ldots\end{aligned} \tag{1.67}$$

A diagrammatic representation of (1.67) is:

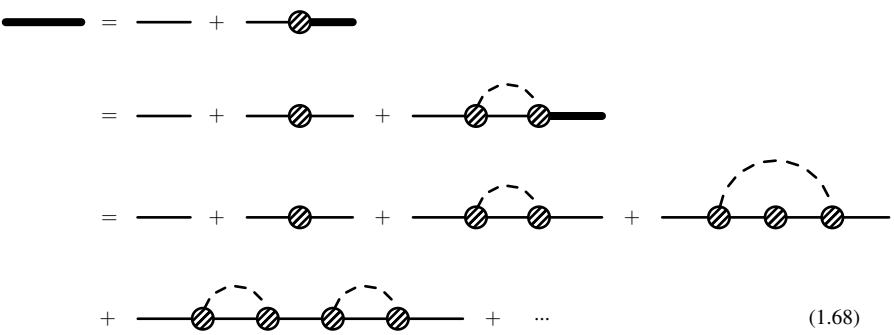

(1.68)

Here a thick line denotes $\mathbf{G}$, a thin line denotes $\mathbf{G}^0$, a dot denotes $\delta\mathbf{H}$ and a dashed line between n points denotes the n-th order correlations of $\delta\mathbf{H}$.

This expansion can be continued to express the full Green's function $\mathbf{G}$ as an infinite series of terms of increasing order in $\mathbf{G}^0$ and $\delta\mathbf{H}$. However, as we are interested only in $\langle\mathbf{G}\rangle$ we only need too include terms that contribute to the ensemble average. Then the leading order contribution to $\langle\mathbf{G}\rangle$ is of second order in $\delta\mathbf{H}$.

We define the self-energy:

$$\Sigma = \langle\delta\mathbf{H}\mathbf{G}^0\delta\mathbf{H}\rangle + \mathcal{O}\left(|\delta\mathbf{H}|^4\right) \tag{1.69}$$

A term of third order in $\delta\mathbf{H}$ would not contribute to the ensemble average, so the next term would be of fourth order and much smaller than the second order term if the disorder is weak. Before we can continue, we introduce the Bourret or smoothing approximation[11] where we only keep terms containing 2-point correlations or the second order moment of $\delta\mathbf{H}$ i.e. we neglect the higher order terms in (1.69. Thus we neglect terms such as diagram four on the right hand side of (1.68) but we include terms like diagram number five. Now we can expand $\langle\mathbf{G}\rangle$ as:

$$\langle \mathbf{G} \rangle = \mathbf{G}^0 + \mathbf{G}^0 \Sigma \langle \mathbf{G} \rangle \tag{1.70}$$

$$= \mathbf{G}^0 + \mathbf{G}^0 \Sigma \mathbf{G}^0 + \mathbf{G}^0 \Sigma \mathbf{G}^0 \Sigma \mathbf{G}^0 + ... \tag{1.71}$$

which, after some arithmetic, we can conveniently rewrite as

$$\begin{aligned} \langle \mathbf{G} \rangle &= \left(\left(\mathbf{G}^0 \right)^{-1} - \Sigma \right)^{-1} \\ &= \left(-\omega + c_0 k \begin{pmatrix} 0 & 1 \\ 1 & 0 \end{pmatrix} - i\varepsilon - \Sigma \right)^{-1} \end{aligned} \tag{1.72}$$

which is called the Dyson equation[17, 18]. Here we have included a small imaginary part to ensure causality as we did in section 1.2.2. It must be emphasized that the Bourret approximation does not neglect higher-order scattering. Rather, we assume all orders of scattering can be treated as a series of uncorrelated single- and double-scattering processes. The Bourret approximation has been shown to be applicable if the disorder is sufficiently weak [12].

Now it's time to write $\delta\mathbf{H}$ in a form such that Σ can be explicitly written in terms of correlation functions of $\delta\mu(x)$ and $\delta\rho(x)$. Up to linear order in $\delta\mu$ and $\delta\rho$ we have

$$\begin{aligned} c = \sqrt{\frac{\mu}{\rho}} &\xrightarrow[\rho \to \rho(x)]{\mu \to \mu(x)} c(x) = c_0 + \delta\mu(x) \cdot \left. \frac{\partial c}{\partial \mu} \right|_{\mu=\mu_0} + \delta\rho(x) \cdot \left. \frac{\partial c}{\partial \rho} \right|_{\rho=\rho_0} + \mathcal{O}\left(|\delta\mu|^2 \right) + \mathcal{O}\left(|\delta\rho|^2 \right) \\ &\xrightarrow[|\delta\rho| \ll \rho_0]{|\delta\mu| \ll \mu_0} c_0 \cdot \left(1 + \frac{\delta\mu(x)}{2\mu_0} - \frac{\delta\rho(x)}{2\rho_0} \right) \end{aligned} \tag{1.73}$$

Thus, the perturbed time evolution operator is:

$$\begin{aligned} \mathbf{H} &= ic(x) \frac{\partial}{\partial x} \begin{pmatrix} 0 & 1 \\ 1 & 0 \end{pmatrix} \\ &= ic_0 \frac{\partial}{\partial x} \begin{pmatrix} 0 & 1 \\ 1 & 0 \end{pmatrix} + ic_0 \left(\frac{\delta\mu(x)}{2\mu_0} - \frac{\delta\rho(x)}{2\rho_0} \right) \frac{\partial}{\partial x} \begin{pmatrix} 0 & 1 \\ 1 & 0 \end{pmatrix} \\ &= \mathbf{H}^0 + \delta\mathbf{H}(x) \;\text{ with }\; \delta\mathbf{H}(x) = \left(\frac{\delta\mu(x)}{2\mu_0} - \frac{\delta\rho(x)}{2\rho_0} \right) \cdot \mathbf{H}^0 \end{aligned} \tag{1.74}$$

As we recall from section 1.2.2 Eq. (1.16) the effect of $\mathbf{H}^0$ on any Ψ can be expressed in terms of its eigenvalues $c\,|k|$ for eigenfunctions Ψ_k^0. For more convenience we introduce new normalized eigenfunctions and suppress the time-dependence unless we need it:

$$\Psi_k^0(x) = \frac{1}{\sqrt{2L}|k|} \begin{pmatrix} |k| \\ k \end{pmatrix} e^{ikx} \tag{1.75}$$

such that they form a complete orthonormal basis:

$$\langle k|l \rangle = \int_0^L \Psi_k^{0*}(x) \Psi_l^0(x) \mathrm{d}x = \delta_{kl} = \begin{cases} 1 & \text{for } k = l \\ 0 & \text{otherwise} \end{cases} \tag{1.76}$$

Here L is the length of the granular chain and we have introduced the Dirac bra-ket notation for scalar products. Then we can write $\mathbf{G}^0$ as:

$$\begin{aligned}
\mathbf{G}^0|\Psi\rangle &= \int_0^L G^0(x-x',\omega)\Psi(x',\omega)\mathrm{d}x' \\
&= \sum_k \int_0^L G^0(x-x',\omega)\Psi_k^0(x')\mathrm{d}x' \cdot \int_0^L \Psi_k^{0*}(x'')\cdot\Psi(x'',\omega)\mathrm{d}x'' \\
&= \sum_k \frac{\Psi_k^0(x)\cdot\langle k|\Psi\rangle}{\omega - c\,|k| - i\varepsilon} \\
&= \left(\sum_k \frac{|k\rangle\langle k|}{\omega - c\,|k| - i\varepsilon}\right)|\Psi\rangle
\end{aligned} \tag{1.77}$$

Then, with the larger, outermost brackets $\langle ...\rangle$ denoting the ensemble average, the self-energy is:

$$\begin{aligned}
&\Sigma_k(\omega) = \left\langle\langle k|\delta\mathbf{H}\mathbf{G}^0\delta\mathbf{H}|k\rangle\right\rangle = \left\langle \sum_l \frac{\langle k|\delta\mathbf{H}|l\rangle\langle l|\delta\mathbf{H}|k\rangle}{\omega - c_0\,|l| - i\varepsilon}\right\rangle \\
&= \sum_l \frac{\left\langle \int_0^L\int_0^L \Psi_k^{0*}(x)\left(\frac{\delta\mu(x)}{2\mu_0} - \frac{\delta\rho(x)}{2\rho_0}\right)\cdot\mathbf{H}^0\Psi_l^0(x)\Psi_l^{0*}(x')\left(\frac{\delta\mu(x')}{2\mu_0} - \frac{\delta\rho(x')}{2\rho_0}\right)\cdot\mathbf{H}^0\Psi_k^0(x')\mathrm{d}x\mathrm{d}x'\right\rangle}{\omega - c_0\,|l| - i\varepsilon} \\
&= \sum_l \frac{\left\langle \int_0^L\int_0^L \Psi_k^{0*}(x)\left(\frac{\delta\mu(x)}{2\mu_0} - \frac{\delta\rho(x)}{2\rho_0}\right)\cdot c_0\,|l|\,\Psi_l^0(x)\Psi_l^{0*}(x')\left(\frac{\delta\mu(x')}{2\mu_0} - \frac{\delta\rho(x')}{2\rho_0}\right)\cdot c_0\,|k|\,\Psi_k^0(x')\mathrm{d}x\mathrm{d}x'\right\rangle}{\omega - c_0\,|l| - i\varepsilon} \\
&= \frac{c_0^2\,|k|}{4}\sum_l \frac{|l|}{\omega - c_0\,|l| - i\varepsilon}\int_0^L\int_0^L \\
&\times\left(\frac{\langle\delta\mu(x)\delta\mu(x')\rangle}{\mu_0^2} - \frac{\langle\delta\rho(x)\delta\mu(x')\rangle}{\rho_0\mu_0} - \frac{\langle\delta\mu(x)\delta\rho(x')\rangle}{\mu_0\rho_0} + \frac{\langle\delta\rho(x)\delta\rho(x')\rangle}{\rho_0^2}\right) \\
&\times\Psi_k^{0*}(x)\Psi_l^0(x)\Psi_l^{0*}(x')\Psi_k^0(x')\mathrm{d}x\mathrm{d}x' \\
&= \frac{c_0^2\,|k|}{4}\sum_l \frac{|l|}{\omega - c_0\,|l| - i\varepsilon}\left(1 + \frac{k\cdot l}{|k|\cdot|l|}\right)^2 \\
&\times\int_0^L\int_0^L\left(\frac{C_{\mu\mu}(x-x')}{\mu_0^2} - 2\frac{C_{\rho\mu}(x-x')}{\rho_0\mu_0} + \frac{C_{\rho\rho}(x-x')}{\rho_0^2}\right)\cdot\frac{\mathrm{e}^{i(x-x')(l-k)}}{4L^2}\mathrm{d}x\mathrm{d}x'
\end{aligned} \tag{1.78}$$

In the last step we inserted the unperturbed eigenfunctions (1.75) and the two-point correlation functions of the fluctuations $C_{\mu\mu}(x,x') = C_{\mu\mu}(x-x') = \langle\delta\mu(x)\delta\mu(x')\rangle$ etc. and we used $C_{\rho\mu}(x-x') = C_{\mu\rho}(x-x')$ which applies if the fluctuations are homogeneous and isotropic. From (1.78) we can see that only intermediate states with $k\cdot l > 0$ contribute to the sum i.e. there are no reflections. So for $k > 0$ the sum only runs over $l > 0$. To further evaluate (1.78) we need to know the correlation functions.

Once the self-energy is obtained from the correlation functions via (1.78), we can determine the ensemble-averaged Green's function via (1.72)

$$\langle G(k,\omega)\rangle = \sum_l \frac{|l\rangle\langle l|}{\omega - c_0|k| - \langle\Sigma_k(\omega)\rangle} \tag{1.79}$$

from which we can immediately identify the effective wavenumber:

$$k_{\text{eff}}(\omega) = \frac{1}{c_0}\left(\omega + \langle\Sigma_{k\approx\omega/c_0}(\omega)\rangle\right) \tag{1.80}$$

Here we have used the on-shell approximation which is valid for sufficiently weak disorder such that $|\Sigma(\omega)| \ll \omega$, thus $k \approx \omega/c_0$ can be used for a zero-th order approximation of the self-energy. In general, k_{eff} is complex. The real part leads to dispersion while the imaginary part leads to extinction of the ensemble-averaged wave as a result of multiple scattering. This attenuation according to $e^{-x\cdot\text{Im}(k_{\text{eff}})} = e^{-x/(2\ell_s)}$ is called Lambert-Beer law. Here $1/\ell_s \approx \text{Im}(\Sigma(\omega))/c_0$ is the scattering mean free path and $1/\tau_s = 2\cdot\text{Im}(\Sigma(\omega))$ is the scattering mean free time. It can be checked that an analogous calculation of ℓ_s based on the Helmholtz equation yields the same result, but then $k_{eff} = \sqrt{k_0^2 - \Sigma}$ must be used due the differently defined Green's function and Dyson equation (see appendix E.2, where explicit calculations with both methods are carried out).

Average Intensity

While the incoherently scattered wave does not contribute to the average amplitude, it still contributes to the average intensity, which we will now focus on. The total intensity of the wave is given by

$$\begin{aligned}\Psi^*(x,t)\cdot\Psi(x,t) &= \int_0^L \Psi^*(x_0,t_0)G^*(x_0-x,t_0-t)\mathrm{d}x_0 \cdot \int_0^L G(x-x_0,t-t_0)\Psi(x_0,t_0)\mathrm{d}x_0 \\ &= \langle\Psi_0|\mathbf{G}^*\otimes\mathbf{G}|\Psi_0\rangle\end{aligned} \tag{1.81}$$

where G^* is the advanced Green's function and $\otimes$ is the dyadic or tensor product. Thus, to get the ensemble-averaged intensity we need to determine $\langle\mathbf{G}^*\otimes\mathbf{G}\rangle$ from the correlation functions. For experiments that measure the intensity profile at a given center-frequency, $\Psi(x_0,t)$ is a pulse or burst whose duration allows for multiple oscillation cycles i.e. it can be thought of as slowly modulated signal of high carrier frequency ω. Accordingly, from now on, we consider modulated waves of modulation frequency $\Omega \ll \omega$ which can be written as superposition of two frequency components at $\omega^+ = \omega+\Omega$ and $\omega^- = \omega-\Omega$. It can be shown [13, 19, 20, 21] that,similar to (1.64) - (1.72), an analogue to the Dyson equation can be derived for the correlation function of the Green's function $\mathbf{G}(\omega^+)\otimes\mathbf{G}^*(\omega^-)$:

$$\langle\mathbf{G}(\omega^+)\otimes\mathbf{G}^*(\omega^-)\rangle = \mathbf{G}(\omega^+)\otimes\mathbf{G}^*(\omega^-) + \mathbf{G}(\omega^+)\otimes\mathbf{G}^*(\omega^-) : \mathbf{U} : \langle\mathbf{G}(\omega^+)\otimes\mathbf{G}^*(\omega^-)\rangle \tag{1.82}$$

This is the Bethe-Salpeter equation[22]. Using the mode basis Ψ_n given by Eq. (1.75) and $\mathbf{G}(\omega^+)\otimes\mathbf{G}^-(\omega^-) = G_k(\omega^+)G_l^*(\omega^-)\delta_{km}\delta_{ln}$ it can be written[3] in terms of $\langle\mathbf{G}(\omega^+)\otimes\mathbf{G}^*(\omega^-)\rangle = \mathcal{L}_{klmn}(\omega,\Omega)$ as:

$$\mathcal{L}_{klmn}(\omega,\Omega) = G_k(\omega^+)G_l^*(\omega^-)\left(\delta_{km}\delta_{ln} + \sum_{ij} U_{klij}(\omega,\Omega)\mathcal{L}_{ijmn}(\omega,\Omega)\right) \tag{1.83}$$

Analogously to the self-energy Σ in the Dyson equation for $\langle\mathbf{G}\rangle$, here we introduce the irreducible vertex function $\mathbf{U}$. It can be written as a series of terms of increasing order in perturbation operators $\delta\mathbf{H}$.

Analogous to the smoothing approximation of the self-energy, we use the ladder approximation[11, 13] which keeps the leading order term contributing to the ensemble average, corresponding to two correlated scattering processes. In this approximation, the irreducible vertex function can be written[3] as:

$$U_{klmn} \approx \langle\langle k|\delta\mathbf{H}|l\rangle\langle m|\delta\mathbf{H}|n\rangle\rangle \tag{1.84}$$

In section 1.3.4 we will use (1.82) and (1.84) as a starting point for a treatment of multiple scattering in the three-dimensional granular medium.

1.3. The Dense Packing

1.3.1. Linear Elasticity in 3D

Now we look at three-dimensional granular media consisting of particles with elastic interactions of nearest neighbors. Let $\mathbf{u}_i = \mathbf{x}_i' - \mathbf{x}_i$ be the displacement of a particle with label i from its equilibrium position $\mathbf{x}_i$. Instead of explicitly treating individual particles, we assume a continuum limit exists similar to the treatment in section 1.2.2 so it suffices to concern ourselves with the continuous displacement field $\mathbf{u}(\mathbf{x},t) = \mathbf{u}(\mathbf{x}_0+\lambda\cdot\xi,t) = \mathbf{u}(\mathbf{x}_0,t) + \left(\xi\cdot\frac{1}{\lambda}\nabla_\xi\right)\mathbf{u}|_{\mathbf{x}_0} + \mathcal{O}\left(|\xi|^2\right)$ as long as it varies on a length scale λ much greater than the inter-particle spacing. Then the distance $s = |\mathbf{x}_1 - \mathbf{x}_2| = |\delta\mathbf{x}|$ between any two neighboring particles will change due to the displacement $\delta\mathbf{u}$ as:

$$\begin{aligned} s'^2 = \left|\delta\mathbf{x}'\right|^2 &= \left(\delta x_i + \delta x_j \frac{1}{\lambda}\frac{\partial u_i}{\partial \xi_j} + \mathcal{O}\left(\left|\frac{\delta\mathbf{x}}{\lambda}\right|^2\right)\right)^2 \\ &= \delta x_i\delta x_i + 2\delta x_i\delta x_j\frac{\partial u_i}{\partial x_j} + \delta x_j\delta x_k\frac{\partial u_i}{\partial x_j}\frac{\partial u_i}{\partial x_k} + \mathcal{O}\left(|\delta\mathbf{x}|\cdot\left|\frac{\delta\mathbf{x}}{\lambda}\right|^2\right) \\ &\xrightarrow{|\delta\mathbf{x}|\ll\lambda} \left(\delta_{ij} + 2\frac{\partial u_i}{\partial x_j} + \frac{\partial u_k}{\partial x_i}\frac{\partial u_k}{\partial x_j}\right)\delta x_i\delta x_j = s^2 + \left(\frac{\partial u_i}{\partial x_j} + \frac{\partial u_j}{\partial x_i} + \frac{\partial u_k}{\partial x_i}\frac{\partial u_k}{\partial x_j}\right)\delta x_i\delta x_j \end{aligned} \tag{1.85}$$

Here we took advantage of the symmetry regarding indices i and j. Now we can define the strain tensor

$$\varepsilon_{ij} = \frac{1}{2}\left(\frac{\partial u_i}{\partial x_j} + \frac{\partial u_j}{\partial x_i} + \frac{\partial u_k}{\partial x_i}\frac{\partial u_k}{\partial x_j}\right) \tag{1.86}$$

such that $s'^2 = s^2 + 2\varepsilon_{ij}\delta x_i\delta x_j$. If the derivative of the displacement and the displacement itself is small[23], as will be assumed in this section, then we can use the approximation

$$\varepsilon_{ij} \approx \frac{1}{2}\left(\frac{\partial u_i}{\partial x_j} + \frac{\partial u_j}{\partial x_i}\right) \tag{1.87}$$

Now we are interested in the forces resulting from small oscillations $\mathbf{u}(\mathbf{x},t)$ of the particles around their equilibrium positions. At leading order they are given by Hooke's law[6]:

$$\sigma_{ij} = C_{ijkl}\varepsilon_{kl} \tag{1.88}$$

Here σ_{ij} is the Cauchy stress tensor and C_{ijkl} is the stiffness tensor. In equilibrium, no net torque is exerted on any volume within the medium:

$$\begin{aligned} 0 = T_i &= \iint_{\partial V} \epsilon_{ijk}\, f_j x_k \mathrm{d}^2 x \\ &= \iint_{\partial V} \epsilon_{ijk}\, \sigma_{jm} n_m x_k \mathrm{d}^2 x = \iiint_V \epsilon_{ijk}\, \partial_m \left(\sigma_{jm} x_k\right) \mathrm{d}^3 x \\ &= \iiint_V \epsilon_{ijk}\, \left(x_k \partial_m \sigma_{jm} + \sigma_{jm} \delta_{km}\right) \mathrm{d}^3 x \end{aligned} \tag{1.89}$$

Here ϵ_{ijk} is the Levi-Civita symbol and $\mathbf{n}$ is the unit normal vector on the boundary surface ∂V. We have used the divergence theorem of vector analysis and the fact that $\partial_i x_j = \delta_{ij}$. The term on the left in the last line of (1.89) vanishes if $\mathbf{x}$ is chosen as the origin. Therefore σ_{ij} is symmetric. As both ε_{ij} and σ_{ij} are symmetric we can also let $C_{ijkl} = C_{jikl}$ and $C_{ijkl} = C_{ijlk}$.

We assume elastic and therefore reversible deformation for which there is a Helmholtz free energy $\mathcal{F}\left[\varepsilon_{ij}\right]$ such that

$$\begin{aligned} \sigma_{ij} &= \frac{\partial \mathcal{F}}{\partial \varepsilon_{ij}} \quad \text{hence} \\ \frac{\partial \sigma_{ij}}{\partial \varepsilon_{kl}} &= \frac{\partial^2 \mathcal{F}}{\partial \varepsilon_{kl} \partial \varepsilon_{ij}} = \frac{\partial^2 \mathcal{F}}{\partial \varepsilon_{ij} \partial \varepsilon_{kl}} = C_{ijkl} \end{aligned} \tag{1.90}$$

Then $C_{ijkl} = C_{klij}$ so the stiffness tensor has only 21 different components out of possible 81. We can take advantage of the symmetries of σ_{ij} and ε_{ij}, which have only 6 independent components each, by introducing the Voigt[24] notation:

$$[\sigma] := \begin{pmatrix} \sigma_1 \\ \sigma_2 \\ \sigma_3 \\ \sigma_4 \\ \sigma_5 \\ \sigma_6 \end{pmatrix} = \begin{pmatrix} \sigma_{11} \\ \sigma_{22} \\ \sigma_{33} \\ \sigma_{23} \\ \sigma_{13} \\ \sigma_{12} \end{pmatrix} \qquad [\varepsilon] := \begin{pmatrix} \varepsilon_1 \\ \varepsilon_2 \\ \varepsilon_3 \\ \varepsilon_4 \\ \varepsilon_5 \\ \varepsilon_6 \end{pmatrix} = \begin{pmatrix} \varepsilon_{11} \\ \varepsilon_{22} \\ \varepsilon_{33} \\ 2 \cdot \varepsilon_{23} \\ 2 \cdot \varepsilon_{13} \\ 2 \cdot \varepsilon_{12} \end{pmatrix} = \begin{pmatrix} \partial_x u_x \\ \partial_y u_y \\ \partial_z u_z \\ \partial_y u_z + \partial_z u_y \\ \partial_x u_z + \partial_z u_x \\ \partial_x u_y + \partial_y u_x \end{pmatrix}$$

$$[C] := \begin{pmatrix} C_{1111} & C_{1122} & C_{1133} & C_{1123} & C_{1131} & C_{1112} \\ C_{2211} & C_{2222} & C_{2233} & C_{2223} & C_{2231} & C_{2212} \\ C_{3311} & C_{3322} & C_{3333} & C_{3323} & C_{3331} & C_{3312} \\ C_{2311} & C_{2322} & C_{2333} & C_{2323} & C_{2331} & C_{2312} \\ C_{3111} & C_{3122} & C_{3133} & C_{3123} & C_{3131} & C_{3112} \\ C_{1211} & C_{1222} & C_{1233} & C_{1223} & C_{1231} & C_{1212} \end{pmatrix} \tag{1.91}$$

To keep the notation clear, indices i, j, k, l always run from 1 to 3 or x to z and indices a, b, c, d always run from 1 to 6. Then Hooke's law is:

$$\sigma_a = C_{ab} \varepsilon_b \tag{1.92}$$

If we now assume the medium is isotropic then the stiffness tensor can be written in terms of only two independent components:

$$C_{ijkl} = \lambda \delta_{ij}\delta_{kl} + \mu \left(\delta_{ik}\delta_{jl} + \delta_{il}\delta_{jk}\right) \tag{1.93}$$

$$\text{And thus} \quad \sigma_{ij} = C_{ijkl}\varepsilon_{kl} = \lambda \delta_{ij}\varepsilon_{kk} + 2 \cdot \mu \cdot \varepsilon_{ij} \tag{1.94}$$

Or, in Voigt notation:

$$[C] = \begin{pmatrix} \lambda+2\mu & \lambda & \lambda & 0 & 0 & 0 \\ \lambda & \lambda+2\mu & \lambda & 0 & 0 & 0 \\ \lambda & \lambda & \lambda+2\mu & 0 & 0 & 0 \\ 0 & 0 & 0 & \mu & 0 & 0 \\ 0 & 0 & 0 & 0 & \mu & 0 \\ 0 & 0 & 0 & 0 & 0 & \mu \end{pmatrix} \tag{1.95}$$

The strain tensor ε_{ij} can be decomposed into its two irreducible parts: the scalar part proportional to the trace of ε times the Kronecker delta, which is called the volumetric (volume-changing) strain or dilatation, and the traceless symmetric tensor, called the deviatoric (shape-changing) or pure shear tensor:

$$\begin{aligned} \varepsilon_{ij} &= \frac{1}{3}\varepsilon_{kk}\delta_{ij} + \left(\varepsilon_{ij} - \frac{1}{3}\varepsilon_{kk}\delta_{ij}\right) \\ &= \frac{1}{3}\mathrm{Tr}(\varepsilon)\delta_{ij} + s_{ij} \end{aligned} \tag{1.96}$$

Similarly, we can decompose the stress tensor:

$$\begin{aligned} \sigma_{ij} &= \frac{1}{3}\mathrm{Tr}(\sigma)\delta_{ij} + \left(\sigma_{ij} - \frac{1}{3}\mathrm{Tr}(\sigma)\delta_{ij}\right) \\ &= \left(\lambda + \frac{2}{3}\mu\right) \cdot \mathrm{Tr}(\varepsilon)\delta_{ij} + 2 \cdot \mu \cdot s_{ij} \\ &= K \cdot \mathrm{Tr}(\varepsilon)\delta_{ij} + 2 \cdot G \cdot s_{ij} \end{aligned} \tag{1.97}$$

Here we have used the constitutive relation (1.94) and in the last step we have replaced the Lamé coefficients λ and μ by the compressional modulus K and the shear modulus G. Now we can write the Helmholtz free energy as:

$$\mathcal{F}[\varepsilon] = \frac{1}{2}K \cdot (\mathrm{Tr}(\varepsilon))^2 + G \cdot s_{ij}s_{ij} \tag{1.98}$$

The term $-K \cdot \mathrm{Tr}(\varepsilon) = -K \cdot \nabla \cdot \mathbf{u} =: p$ is called pressure and $2 \cdot G \cdot s_{ij}$ is called shear stress.

Linear Wave Equation

Now we are interested in the various modes of wave propagation within the three-dimensional medium. To this end we apply Newton's second law of motion to a volume V within the medium. (An alternative derivation is shown in appendix E.1) We limit the motion of the particles constituting the medium to small oscillations such that the number of particles and hence the effective density $\rho(\mathbf{x})$ of the medium within V stays constant in time but may still vary in space. On the boundary surface ∂V with normal vector $\mathbf{n}$ a force is acting proportional to the stress tensor field σ_{ij}. In addition there can be a body force

density $\mathbf{f}(\mathbf{x},t)$ such as gravity (with $\mathbf{f} = -\mathbf{g}\cdot\rho$) acting on the medium within V. Then the equation of motion is:

$$\begin{aligned}\frac{\partial}{\partial t}\iiint_V \rho(\mathbf{x})\partial_t u_i(\mathbf{x},t)\mathrm{d}^3x &= \iiint_V f_i(\mathbf{x},t)\mathrm{d}^3x + \iint_{\partial V}\sigma_{ij}(\mathbf{x},t)\cdot n_j(\mathbf{x})\mathrm{d}^2x \\ &= \iiint_V f_i(\mathbf{x},t) + \partial_j\sigma_{ij}(\mathbf{x},t)\mathrm{d}^3x \end{aligned} \tag{1.99}$$

Here we used the divergence theorem of vector analysis. Finally, we get an equation for the integrand:

$$\rho(\mathbf{x})\partial_t^2 u_i(\mathbf{x},t) = \partial_j\sigma_{ij}(\mathbf{x},t) + f_i(\mathbf{x},t) \tag{1.100}$$

For the linear isotropic medium we can now insert the constitutive relation (1.94) into (1.100) to get:

$$\begin{aligned}\rho(\mathbf{x})\partial_t^2 u_i(\mathbf{x},t) &= \partial_j\left(\lambda(\mathbf{x})\delta_{ij}\varepsilon_{kk}(\mathbf{x},t) + 2\cdot\mu(\mathbf{x})\varepsilon_{ij}(\mathbf{x},t)\right) + f_i(\mathbf{x},t) \\ &= \varepsilon_{kk}(\mathbf{x},t)\left(\partial_i\lambda(\mathbf{x})\right) + 2\varepsilon_{ij}(\mathbf{x},t)\left(\partial_j\mu(\mathbf{x})\right) \\ &\quad + \left(\lambda(\mathbf{x}) + 2\mu(\mathbf{x})\right)\partial_i\partial_j u_j(\mathbf{x},t) - \mu(\mathbf{x})\partial_j\left(\partial_i u_j(\mathbf{x},t) - \partial_j u_i(\mathbf{x},t)\right) + f_i(\mathbf{x},t)\end{aligned} \tag{1.101}$$

To more clearly emphasize the meaning of the terms in this equation we can divide (1.101) by $\rho(\mathbf{x})$, move the terms with derivatives of the Lamé coefficients and the external force to the right hand side and all other terms to the left hand side and use index-free notation:

$$\begin{aligned}&\frac{\partial^2}{\partial t^2}\mathbf{u}(\mathbf{x},t) - \frac{\lambda(\mathbf{x})+2\mu(\mathbf{x})}{\rho(\mathbf{x})}\nabla\left(\nabla\cdot\mathbf{u}(\mathbf{x},t)\right) + \frac{\mu(\mathbf{x})}{\rho(\mathbf{x})}\nabla\times\nabla\times\mathbf{u}(\mathbf{x},t) \\ &= \frac{1}{\rho(\mathbf{x})}\left(\left(\nabla\lambda(\mathbf{x})\right)\left(\nabla\cdot\mathbf{u}(\mathbf{x},t)\right) + 2\left(\nabla\mu(\mathbf{x})\right)\varepsilon(\mathbf{x},t) + \mathbf{f}(\mathbf{x},t)\right)\end{aligned} \tag{1.102}$$

Now we can see (1.102) is an inhomogeneous linear wave equation for the three-dimensional displacement field $\mathbf{u}(\mathbf{x},t)$ in a medium of spatially varying density and elastic coefficients.

Homogeneous Medium

In the simplest case, ρ, λ and μ are just constants. Then the right hand side of (1.102) contains only the external force term:

$$\frac{\partial^2}{\partial t^2}\mathbf{u}(\mathbf{x},t) - \frac{\lambda+2\mu}{\rho}\nabla\left(\nabla\cdot\mathbf{u}(\mathbf{x},t)\right) + \frac{\mu}{\rho}\nabla\times\nabla\times\mathbf{u}(\mathbf{x},t) = \frac{1}{\rho}\mathbf{f}(\mathbf{x},t) \tag{1.103}$$

For a more explicit interpretation of the homogeneous equation we now consider the Helmholtz decomposition of the displacement vector field:

$$\begin{aligned}&\mathbf{u}(\mathbf{x},t) = \mathbf{P}(\mathbf{x},t) + \mathbf{S}(\mathbf{x},t) \\ \text{such that }\ &\nabla\times\mathbf{P}(\mathbf{x},t) = 0 \\ &\nabla\cdot\mathbf{S}(\mathbf{x},t) = 0\end{aligned} \tag{1.104}$$

The last two equalities are satisfied for

$$\begin{aligned}\mathbf{P}(\mathbf{x},t) &= \nabla\phi(\mathbf{x},t)\\ \mathbf{S}(\mathbf{x},t) &= \nabla\times\mathbf{A}(\mathbf{x},t)\end{aligned} \tag{1.105}$$

We notice that the displacement vector has three components, one of which, $\mathbf{P}(\mathbf{x},t)$ being fully determined by $\phi(\mathbf{x},t)$. Then $\mathbf{S}(\mathbf{x},t)$ can only have two linearly independent components. Therefore $\mathbf{A}(\mathbf{x},t)$ has an extra degree of freedom left undetermined by the wave equation (1.103). To fix it, we impose on it an arbitrary additional equation:

$$\nabla\cdot\mathbf{A}(\mathbf{x},t) = 0 \tag{1.106}$$

This is called the Coulomb gauge condition, which is also known for its usage in electrodynamics. After inserting $\mathbf{P}(\mathbf{x},t)$ and $\mathbf{S}(\mathbf{x},t)$ into the homogeneous part of (1.103) while using (1.105) and (1.106) we get:

$$\begin{aligned}\frac{\partial^2}{\partial t^2}\mathbf{P}(\mathbf{x},t) - \frac{\lambda+2\mu}{\rho}\Delta\mathbf{P}(\mathbf{x},t) = 0\\ \frac{\partial^2}{\partial t^2}\mathbf{S}(\mathbf{x},t) - \frac{\mu}{\rho}\Delta\mathbf{S}(\mathbf{x},t) = 0\end{aligned} \tag{1.107}$$

Here $\Delta = \partial_i\partial_i = \nabla\cdot\nabla$ and we have used $\nabla\times\nabla\times\mathbf{S} = \nabla\times\nabla\times\nabla\times\mathbf{A} = \nabla\times(\nabla(\nabla\cdot\mathbf{A}) - \Delta\mathbf{A}) = -\nabla\times\Delta\mathbf{A} = -\Delta\mathbf{S}$. Each of $\mathbf{P}$ and $\mathbf{S}$ is a solution of the homogeneous wave equation. Solutions $\mathbf{P}$ are called P-waves, pressure waves or longitudinal waves. They propagate at phase velocity $\sqrt{(\lambda+2\mu)/\rho}$. Solutions $\mathbf{S}$ are called S-waves, shear waves or transversal waves. Their phase velocity is $\sqrt{\mu/\rho}$. Due to both λ and μ being non-negative, P-waves are always faster than S-waves by at least a factor of $\sqrt{2}$. As the wave equation is linear, any linear combination of $\mathbf{P}$ and $\mathbf{S}$ is also a solution. In general, the full solution of the inhomogeneous equation will be a superposition of P- and S-waves which will be important in later sections where we will examine inhomogeneities that lead to coupling between P- and S-waves.

3D Schrödinger Equation

As we have seen already in section 1.2 it is useful to re-write the wave equation into a set of equations of first order derivatives in time so we can treat multiple scattering problems in a perturbative approach. Completely analogous to my treatment in 1D in section 1.2 the following definitions are found in the literature[3]:

$$\Psi(\mathbf{x},t) = \begin{pmatrix}\sqrt{\frac{\lambda(\mathbf{x})}{2}}\mathbf{p}\cdot\mathbf{u}\\ \sqrt{\frac{\rho(\mathbf{x})}{2}}i\frac{\partial u_k}{\partial t}\\ -i\sqrt{\mu(\mathbf{x})}\varepsilon_{ij}\end{pmatrix} \tag{1.108}$$

which is a 13 component vector-valued wave function. Here $\mathbf{p} := -i\nabla$. However, since $\mathrm{Tr}(\varepsilon) = \nabla\cdot\mathbf{u}$ and $\varepsilon_{ij} = \varepsilon_{ji}$ this leaves only 9 independent components. In this definition Ψ is normalized such that the norm induced by its scalar product equals the total elastic energy within the medium of volume V:

$$\begin{aligned}\langle\Psi|\Psi\rangle &= \iiint_V \Psi^*(\mathbf{x},t)\cdot\Psi(\mathbf{x},t)\mathrm{d}^3x \\ &= \iiint_V \frac{1}{2}\rho(\mathbf{x})\left(\frac{\partial\mathbf{u}}{\partial t}\right)^2 + \frac{1}{2}\lambda(\mathbf{x})\left(\nabla\cdot\mathbf{u}\right)^2 + \mu(\mathbf{x})\varepsilon^*_{ij}\varepsilon_{ji}\mathrm{d}^3x \end{aligned} \tag{1.109}$$

Using $L_{ijk} = \frac{1}{2}\left(p_i\delta_{jk} + p_j\delta_{ik}\right)$ we can define the time evolution operator:

$$\mathbf{H} = \begin{pmatrix} 0 & \sqrt{\lambda(\mathbf{x})}p_k\frac{1}{\sqrt{\rho(\mathbf{x})}} & \mathbf{0}_{1\times9} \\ \frac{1}{\sqrt{\rho(\mathbf{x})}}p_k\sqrt{\lambda(\mathbf{x})} & \mathbf{0}_{3\times3} & \frac{1}{\sqrt{\rho(\mathbf{x})}}L_{ijk}\sqrt{2\mu(\mathbf{x})} \\ \mathbf{0}_{9\times1} & \sqrt{2\mu(\mathbf{x})}L_{ijk}\frac{1}{\sqrt{\rho(\mathbf{x})}} & \mathbf{0}_{9\times9} \end{pmatrix} \tag{1.110}$$

Then Ψ satisfies the Schrödinger equation:

$$i\frac{\partial}{\partial t}\Psi(\mathbf{x},t) = \mathbf{H}\Psi(\mathbf{x},t) + \Psi_f(\mathbf{x},t) \tag{1.111}$$

Here $\Psi_f(\mathbf{x},t) = (0,\mathbf{f}(\mathbf{x},t)/\rho(\mathbf{x}),\mathbf{0}_{1\times9})^T$ contains the external force. A simple calculation shows that (1.111) implies the wave equation (1.102).

As the careful reader may notice, $\mathbf{H}$ as defined in (1.110) and evaluated at constant density and Lamé coefficients is symmetric and has 6 positive real eigenvalues plus the eigenvalue zero of multiplicity 7. The latter result from redundant components in our definition of Ψ given by (1.108). A similar treatment in the literature by Ryzhik et al[2] based on an equivalent hydrodynamic theory as presented here uses a definition of Ψ with only 10 components where only the 6 independent components of ε are included. The related time evolution operator has only 10 eigenvalues, 4 of which are zero. As Ryzhik argues, the latter correspond to non-propagating modes having frequency zero.

Now, one could think of omitting yet another redundant component of Ψ by splitting ε in its trace and the remaining 5 independent components of its traceless symmetric part. Then only three zero eigenvalues would be left. However, there is an even better treatment[25]:

Christoffel Equation

Instead of making up arbitrary redundant vector fields, we use (1.100) with a stiffness tensor that can be arbitrarily anisotropic:

$$\rho(\mathbf{x})\partial_t u_i(\mathbf{x},t) = \partial_j C_{ijkl}\varepsilon_{kl} + f_i(\mathbf{x},t) \tag{1.112}$$

It is convenient to define the gradient in Voigt notation:

$$[\nabla]_{ia} = \begin{pmatrix} \partial_x & 0 & 0 & 0 & \partial_z & \partial_y \\ 0 & \partial_y & 0 & \partial_z & 0 & \partial_x \\ 0 & 0 & \partial_z & \partial_y & \partial_x & 0 \end{pmatrix}_{ia} \tag{1.113}$$

Now we can write (1.112) in Voigt notation:

$$\rho(\mathbf{x})\partial_t^2\mathbf{u}(\mathbf{x},t) = [\nabla]\cdot[C(\mathbf{x})]:[\nabla]\,\mathbf{u}(\mathbf{x},t) + \mathbf{f}(\mathbf{x},t) \tag{1.114}$$

Then we take the spatial and temporal Fourier transform:

$$-\omega^2\rho(\mathbf{k})\mathbf{u}(\mathbf{k},\omega) = -[\mathbf{k}]\cdot[C(\mathbf{k})]:[\mathbf{k}]\,\mathbf{u}(\mathbf{k},\omega)+\mathbf{f}(\mathbf{k},\omega) \tag{1.115}$$

It is convenient to split the wave-vector into its magnitude and a unit vector of its direction:

$$[\mathbf{k}] = k\cdot[\mathbf{I}] = k\cdot\begin{pmatrix} I_x & 0 & 0 & 0 & I_z & I_y \\ 0 & I_y & 0 & I_z & 0 & I_x \\ 0 & 0 & I_z & I_y & I_x & 0 \end{pmatrix} \tag{1.116}$$

The homogeneous equation can now be written with Cartesian and Voigt indices:

$$\rho(\mathbf{k})\omega^2 u_i(\mathbf{k},\omega) = k^2 I_{ia} C_{ab}(\mathbf{k}) I_{bj} u_j(\mathbf{k},\omega) \tag{1.117}$$

After introducing $\Gamma_{ij} = I_{ia}C_{ab}I_{bj}$ we can write simply:

$$\left(k^2\Gamma_{ij}(\mathbf{k}) - \omega^2\rho(\mathbf{k})\delta_{ij}\right)u_j(\mathbf{k},\omega) = 0 \tag{1.118}$$

This is called the Christoffel equation. In case of constant density and Lamé coefficients we realize immediately that (1.118) is an eigenvalue equation for plane wave eigenfunctions $\mathbf{u}(\mathbf{x},t) = \mathbf{u}^{(p)}\mathrm{e}^{i\omega t - ik\mathbf{I}\cdot\mathbf{x}}$ where $\mathbf{u}^{(p)}$ is the polarization vector:

$$k^2\Gamma_{ij}u_j^{(\mathbf{k},p)}(\mathbf{x},t) = \omega^2\rho\,\delta_{ij}u_j^{(\mathbf{k},p)}(\mathbf{x},t) \tag{1.119}$$

Here the superscripts indicate $\mathbf{u}^{(\mathbf{k},p)}$ is a plane wave of wave-vector $\mathbf{k} = k\cdot\mathbf{I}$ and polarization p.

1.3.2. Effective Medium Theory

In the previous section only a linear continous medium was adressed which is not immediately applicable to the behaviour of a granular packing. A continuum limit, in which stress and strain fields on a length scale much larger than the particle size can be defined such that the usual concepts of linear elasticity can be applied as an approximation for the system's response to applied stress or perturbations on that large length scale if some strong simplifying conditions are met: The packing is initially in a jammed state where each bead is in contact with Z neighboring beads. The contact force between neighboring beads is described by the Hertzian model[5], taking into account only normal forces, or the Hertz-Mindlin model[26, 27] that also accounts for tangential forces. Only two-particle interaction is considered i.e. the total force acting on one bead due to contacts to its Z neighbors is the sum of the contact forces of Z bead pairs, which is not valid in general but may be a good approximation if the bead remains approximately spherical under load. As the beads may be randomly but homogeneously distributed in space, the contact number may vary from bead to bead. Here, we only consider the average contact number or coordination number Z. When a continous strain field $\varepsilon_{ij}(\mathbf{x})$ is introduced, it may affect the existing contacts by changing the distance of between bead center-point, and thus the bead overlap, according to the displacement field, but no contacts are broken or newly created. Then, it can be shown[28, 29, 30] that elastic moduli such as the effective Lame moduli λ^* and μ^* or compressional K^* and shear moduli G^* arise, that, under hydrostatic compression $\varepsilon_{ij} = \varepsilon\delta_{ij}$, or under the equivalent pressure p, are proportional to $\phi^{2/3}Z^{2/3}p^{1/3}$ where ϕ is the volume ratio filled by the beads. This approach is reffered to as effective medium theory (EMT). Special cases can be treated exactly, such as random packings of monodisperse, infinitely rough or infinitely smooth Hertz-Mindlin spheres,

for which longitudinal and transverse sound speeds $c_p = \sqrt{(\lambda^* + 2\mu^*)/(\phi\rho)}$ and $c_s = \sqrt{\mu/(\phi\rho}$ can be calculated [29]:

$$c_{p,\text{rough}} = \sqrt{\frac{E}{\rho}}\phi^{-1/6}Z^{1/3}\left(\frac{p}{E}\right)^{1/6}\sqrt{\frac{1}{10}\frac{10-7\nu}{2-\nu}\left(\frac{12}{\pi}\frac{1}{(1-\nu^2)^2}\right)^{1/3}} \tag{1.120}$$

$$c_{s,\text{rough}} = \sqrt{\frac{E}{\rho}}\phi^{-1/6}Z^{1/3}\left(\frac{p}{E}\right)^{1/6}\sqrt{\frac{1}{10}\frac{5-4\nu}{2-\nu}\left(\frac{12}{\pi}\frac{1}{(1-\nu^2)^2}\right)^{1/3}} \tag{1.121}$$

$$c_{p,\text{smooth}} = \sqrt{\frac{E}{\rho}}\phi^{-1/6}Z^{1/3}\left(\frac{p}{E}\right)^{1/6}\sqrt{\frac{3}{10}\left(\frac{12}{\pi}\frac{1}{(1-\nu^2)^2}\right)^{1/3}} \tag{1.122}$$

$$c_{s,\text{smooth}} = \sqrt{\frac{E}{\rho}}\phi^{-1/6}Z^{1/3}\left(\frac{p}{E}\right)^{1/6}\sqrt{\frac{1}{10}\left(\frac{12}{\pi}\frac{1}{(1-\nu^2)^2}\right)^{1/3}} \tag{1.123}$$

Here, the bulk material density ρ, elastic (Young's) modulus E and Poisson ratio ν are used. The $c \propto p^{1/6}$ dependence results from the Hertzian force law $F \propto \delta^{3/2}$. The pressure dependence has been tested with sound speed measurements and was confirmed for high confinement pressures $\propto 100 - 1000$ kPa in glass bead packings (for comparison: $E_{glass} \approx 50$ GPa) but deviations are found at lower pressures $\propto 10$ kPa, where $c \propto p^{1/4}$, corresponding to $\lambda^* \propto \mu^* \propto p^{1/2}$ is in much better agreement with the data[31, 32, 33]. Further deviations from EMT are found in the non-constant ratio of effective bulk and shear moduli, which may be related to non-affine deformations, leading to a non-constant but pressure-dependent coordination number[34].

1.3.3. Jiang-Liu Elasticity

Analogously to the linear medium, for which the the Helmholtz free energy is given by Eq. (1.98), in the granular medium we can use a similar expression, but it must take into account the dependency of the elastic moduli on the compression of the packing $\Delta = 1 - \rho_0/\rho = -\text{Tr}(\varepsilon)$, here expressed in terms of the density. If we assume the compressional and shear moduli be proportional to some power of Δ as proposed by Jiang and Liu[35, 36] then we get:

$$F = \frac{1}{2}\tilde{K}\Delta^b\left(\text{Tr}(\varepsilon)\right)^2 + \tilde{G}\Delta^a s_{ij}s_{ij} \tag{1.124}$$

The numerical value of the exponents a and b is not a priori clear. Several possible cases are of special interest: for $a = b = 0$ we note that (1.124) reduces to the free energy of linear elasticity (1.98). More generally, it can be shown[37] that $a = b = 1/2$, which arises from Hertzian contact forces, leads to a pressure dependent sound speed $c_p \propto p_0^{1/6}$ and $a = b = 1$ leads to $c_p \propto p_0^{1/4}$. The former case is empirically found for packings at high confinement pressure while the latter case is found for low pressure[33]. As pointed out by Trujillo et al[37] one could think of a general $c_p \propto p_0^{\nu}$ power-law with an exponent $\nu = \frac{b}{2(b+1)}$ that depends on the order of magnitude of p_0. Based on the empirical data available so far, however, it is not clear, how a and b and thus ν depend on confinement pressure when the latter is varied by many orders of magnitude. In two-dimensional systems, a continous change of ν with pressure was shown in [38] based on experiments in disordered monolayers[39], where it the deviation from Hertzian behaviour was shown to originate from stress disorder which becomes increasingly important as the pressure is decreased. For three-dimensional systems, measurements of the sound speed at much lower pressure than previously reported in the literature could provide necessary new insight here. In chapter 2 of this thesis such measurements are shown.

1.3.4. Disorder and Multiple Scattering

Based on the Jiang-Liu elasticity from the previous section 1.3.3 the perturbative treatment of scattering on random disorder from section 1.2.7 can be used for a treatment of multiple scattering in the three-dimensional granular medium. Following Trujillo et al[21, 14] we introduce a time-evolution operator similar to (1.110) in section 1.3.1 that is consistent with the Jiang-Liu model:

$$\mathbf{H} = \begin{pmatrix} 0 & \sqrt{\lambda(\mathbf{x})}p_k \frac{1}{\sqrt{\rho(\mathbf{x})}} & \mathbf{0}_{1\times 9} \\ \frac{5}{4\sqrt{\rho(\mathbf{x})}} p_k \sqrt{\lambda(\mathbf{x})} & \mathbf{0}_{3\times 3} & \frac{1}{\sqrt{\rho(\mathbf{x})}} \left(L_{ijk}\sqrt{2\mu(\mathbf{x})} - p_k \frac{1}{2\Delta}\sqrt{\frac{\mu(\mathbf{x})}{2}}\varepsilon_{ij}(\mathbf{x}) \right) \\ \mathbf{0}_{9\times 1} & \sqrt{2\mu(\mathbf{x})}L_{ijk}\frac{1}{\sqrt{\rho(\mathbf{x})}} & \mathbf{0}_{9\times 9} \end{pmatrix} \tag{1.125}$$

As appropriate for Hertzian contacts, $\lambda(\mathbf{x}) = \lambda_0\sqrt{\Delta(\mathbf{x})}$, $\mu(\mathbf{x}) = \mu_0\sqrt{\Delta(\mathbf{x})}$. Compared to (1.110) there is a new Δ-dependent term on the included in (1.125) as first introduced by Trujillo to account for dilatancy, yield and stress anisotropy consistent with Jiang-Liu elasticity. After introducing $\Delta_1 = 1 + 5\Delta(\mathbf{x})/(4\delta_0)$ and $\Delta_2 = 1 - \Delta(\mathbf{x})/\delta_0$ we can write the perturbation operator:

$$\delta\mathbf{H} = \begin{pmatrix} 0 & \frac{1}{4}\sqrt{\frac{\lambda_0}{\rho_0}}\frac{\Delta(\mathbf{x})}{\delta_0}p_k & \mathbf{0}_{1\times 9} \\ \frac{1}{4}\sqrt{\frac{\lambda_0}{\rho_0}}p_k\Delta_1(\mathbf{x}) & \mathbf{0}_{3\times 3} & \frac{1}{2\sqrt{2}}\sqrt{\frac{\lambda_0}{\rho_0}}\left(L_{ijk}\frac{\Delta(\mathbf{x})}{\delta_0} - \frac{p_k\varepsilon_{ij}}{\delta_0}\Delta_2(\mathbf{x}) \right) \\ \mathbf{0}_{9\times 1} & \frac{1}{2\sqrt{2}}\sqrt{\frac{\mu_0}{\rho_0}}\frac{\Delta(\mathbf{x})}{\delta_0}L_{ijk} & \mathbf{0}_{9\times 9} \end{pmatrix} \tag{1.126}$$

It is woth noting that in this approach, the disorder is fully defined by $\Delta(\mathbf{x})$ and is thus a scalar random process which has only one correlation function, which is the simplest case that can be studied. In [21, 14] a delta correlated Gaussian process with zero mean is assumed, which, at least for isotropic granular packings at high confinement pressure, is supported by measurements[40, 41]. In a more general treatment, to be studied in the future, independent small fluctuations of ρ, λ and μ are possible, as long as the Helmholtz free energy is kept convex so mechanical stability is ensured, as well as anisotropy. For example, for two-dimensional packings under shear and anisotropic load there is already evidence of a finite correlation length[42].

Radiative Transport Equation

In section 1.2.7 the Bethe-Salpeter (1.82) and irreducible vertex function (1.84) was introduced. While it can often not be solved exactly, a radiative transfer equation for elastic waves in granular media can be derived that describes transport of the wave intensity. A detailed derivation is found in [21]. The resulting equation is:

$$\left(\frac{\partial}{\partial t} + \mathbf{v}_j\cdot\nabla + \frac{1}{\tau_{j\mathbf{k}_j}} \right) L_{j\mathbf{k}_j}(\mathbf{x},t) = \left| S_{j\mathbf{k}_j}(\omega) \right|^2 \delta(\mathbf{x})\delta(t) + \omega^2 \sum_i \int W(j\mathbf{k}_j, i\mathbf{k}_i) L_{i\mathbf{k}_i}(\mathbf{x},t) n_i \frac{\mathrm{d}^2 k_i}{2\pi} \tag{1.127}$$

In this notation $j\mathbf{k}_j$ denotes the mode with wavevector $\mathbf{k}_j$ on the branch j. Here $L_{j\mathbf{k}_j}(\mathbf{x},t)$ is the specific intensity received at position $\mathbf{x}$ at time t after excitation at frequency ω from a source $S_{j\mathbf{k}_j}(\omega)$ at the origin. $\frac{\partial}{\partial t}$ is the Lagrangian time derivative, $\mathbf{v}_j\cdot\nabla$ is a hydrodynamic convective flow term and $\tau_{j\mathbf{k}_k} = -1/(2\mathrm{Im}(\Sigma_n(\omega)))$ is the extinction time of the average amplitude (here n is the same mode

as $j\mathbf{k}_j$). The $W(j\mathbf{k}_j, i\mathbf{k}_i)$ term is derived from $\left\langle \langle \Psi_n | \delta \mathbf{H} | \Psi_m \rangle^2 \right\rangle$ and describes the scattering. Here, $n_i(\omega) = k_i(\omega)/v_i$ is a spectral weight per unit surface in phase space with $v_i = \frac{\mathrm{d}\omega_i}{\mathrm{d}k_i}$ being the group velocity. For a realistic granular medium, inelastic absorption contributes to the losses, which can be accounted for by replacing $\frac{1}{\tau_{j\mathbf{k}_j}}$ by $\frac{1}{\tau_{j\mathbf{k}_j}} + \frac{1}{\tau_a}$ with the absorption time τ_a.

Diffusive Transport

A particularly simple case arises for large sample thickness with low absorption such that the received signal corresponds to a wave affected by many scattering processes, which can be described by a diffusion approximation of (1.127). After many scattering processes, the incident wave energy is distributed evenly along all accesible modes with largest contribution contained in the shear wave modes at a ratio $E_s/E_p = 2(c_p/c_s)^3 \geq 10$ compared to the longitudinal modes due to $c_p/c_s \geq \sqrt{3}$ and two shear wave polarizations in three dimensions[43, 44, 41]. Then a diffusion equation for the elastic energy density $U(\mathbf{x},t)$ arises[21]:

$$\left(\frac{\partial}{\partial t} - D(\omega)\nabla^2 + \frac{1}{\tau_a} \right) U(\mathbf{x},t) = S(\omega)\delta(\mathbf{x})\delta(t) \tag{1.128}$$

Shock-Waves

Similar to the solitons in one-dimensional systems, as discussed in section 1.2.6, strongly nonlinear waves are found in two- and three-dimensional granular packings. We assume that for plane wave problems a quasi-one-dimensional model can be applied.

Let the potential energy due to the particle overlap δ be $U \propto \delta^\alpha$. The initial overlap and overlap in front of the shock is δ_0 and the overlap behind the shock-front is $\delta_s > \delta_0$. It can be shown[45, 46] that conservation of mass and momentum across the shock-front implies the shock velocity v_{shock} depends on δ_s according to:

$$\frac{v_{\text{shock}}}{c_p} = \sqrt{\frac{1}{\alpha - 1} \frac{(\delta_s/\delta_0)^{\alpha-1} - 1}{\delta_s/\delta_0 - 1}} \tag{1.129}$$

For Hertzian contacts $\alpha = 5/2$. Then the pressure in front and behind the shock-front is $p_0 \propto \delta_0^{3/2}$ and $p_i \propto \delta_s^{3/2}$. The shock velocity in terms of pressure is then given by

$$\frac{v_{\text{shock}}}{c_p} = \sqrt{\frac{2}{3} \frac{p_i/p_0 - 1}{(p_i/p_0)^{2/3} - 1}} \xrightarrow{p_i/p_0 \to \infty} \sqrt{\frac{2}{3}} \left(\frac{p_i}{p_0} \right)^{1/6} \tag{1.130}$$

where the sonic vacuum limit is taken in the last step. When the shock has reached a stationary state, the kinetic and potential energy are of the same order of magnitude[46], thus the particle velocity at the shock-front is related to the overlap by $v_p^2 \propto \delta_s^{5/2}$. Then the amplitude dependence of the shock velocity in the sonic vacuum can also be written in terms of the particle velocity: $v_{\text{shock}} \propto v_p^{1/5}$.

Bibliography

[1] Goldstein Herbert. *Classical Mechanics*. Addison Wesley Publishing Company, 1980.

[2] Leonid Ryzhik, George Papanicolaou, and Joseph B Keller. Transport equations for elastic and other waves in random media. *Wave motion*, 24(4):327–370, 1996.

[3] Nicolas P Tregoures and Bart A Van Tiggelen. Quasi-two-dimensional transfer of elastic waves. *Physical Review E*, 66(3):036601, 2002.

[4] Neil W Ashcroft, N David Mermin, et al. *Solid state physics*. New York: Holt, Rinehart and Winston,, 1976.

[5] H Hertz. Über die berührung fester elastischer körper und über die harte. *Gesammelte Werke. Bd*, 1, 1882.

[6] L D Landau, L. P. Pitaevskii, A. M. Kosevich, and E.M. Lifshitz. *Theory of Elasticity: Volume 7 (Theoretical Physics)*. Butterworth-Heinemann, 1986.

[7] V Tournat, VE Gusev, and B Castagnede. Self-demodulation of elastic waves in a one-dimensional granular chain. *Physical Review E*, 70(5):056603, 2004.

[8] Vincent Tournat, Vladimir Zaitsev, Vitalyi Gusev, Veniamin Nazarov, Philippe Béquin, and Bernard Castagnède. Probing weak forces in granular media through nonlinear dynamic dilatancy: clapping contacts and polarization anisotropy. *Physical review letters*, 92(8):085502, 2004.

[9] Thomas Brunet, Xiaoping Jia, and Paul A Johnson. Transitional nonlinear elastic behaviour in dense granular media. *GEOPHYSICAL RESEARCH LETTERS*, 35:L19308, 2008.

[10] VF Nesterenko. Propagation of nonlinear compression pulses in granular media. *J. Appl. Mech. Tech. Phys. (Engl. Transl.)*, 24(5):733–743, 1983. Translated from Zhurnal Prikladnoi Mekhaniki i Tekhnicheskoi Fiziki, No. 5, pp. 136-148, September-October, 1983.

[11] Uriel Frisch. Wave propagation in random media. *Institue d'Astrophysique centre national de la recherche, Paris, Academic Press Inc., New York, USA, Card Nr. 68-18657*, 1968.

[12] SM Rytov, Yu A Kravtsov, and VI Tatarski. Principles of statistical radiophysics, vol. 1 springer-verlag, 1987.

[13] Ping Sheng. *Introduction to wave scattering, localization and mesoscopic phenomena*, volume 88. Springer Science & Business Media, 2006.

[14] Leonardo Trujillo, Franklin Peniche, and Xiaoping Jia. Multiple scattering of elastic waves in granular media: Theory and experiments. In Ruben Pico Vila, editor, *Waves in Fluids and Solids*, chapter 5. IntechOpen, Rijeka, 2011.

[15] G Ross and RC Chivers. A note on the helmholtz equations for acoustic waves in inhomogeneous media. *The Journal of the Acoustical Society of America*, 80(5):1536–1539, 1986.

[16] Ibrahim Baydoun, Diego Baresch, Romain Pierrat, and Arnaud Derode. Radiative transfer of acoustic waves in continuous complex media: Beyond the helmholtz equation. *Physical Review E*, 94(5):053005, 2016.

[17] Freeman J Dyson. The s matrix in quantum electrodynamics. *Physical Review*, 75(11):1736, 1949.

[18] Julian Schwinger. On the green's functions of quantized fields. i. *Proceedings of the National Academy of Sciences*, 37(7):452–455, 1951.

[19] Ad Lagendijk and Bart A Van Tiggelen. Resonant multiple scattering of light. *Physics Reports*, 270(3):143–215, 1996.

[20] MCW van van Rossum and Th M Nieuwenhuizen. Multiple scattering of classical waves: microscopy, mesoscopy, and diffusion. *Reviews of Modern Physics*, 71(1):313, 1999.

[21] Leonardo Trujillo, Franklin Peniche, and Leonardo Di G Sigalotti. Derivation of a schrödinger-like equation for elastic waves in granular media. *Granular Matter*, 12(4):417–436, 2010.

[22] Edwin E Salpeter and Hans Albrecht Bethe. A relativistic equation for bound-state problems. *Physical Review*, 84(6):1232, 1951.

[23] G Lámer. Notes on the theory of large displacement with small strain. *Periodica Polytechnica Civil Engineering*, 29(1-2):53–65, 1985.

[24] Woldemar Voigt et al. *Lehrbuch der kristallphysik*, volume 962. Teubner Leipzig, 1928.

[25] Bertram Alexander Auld. Acoustic fields and waves in solids. *Wiley Interscience Pub.*, 1973.

[26] Raymond D Mindlin. Elastic spheres in contact under varying oblique forces. *J. Applied Mech.*, 20:327–344, 1953.

[27] Raymond David Mindlin. Compliance of elastic bodies in contact. *J. Appl. Mech., ASME*, 16:259–268, 1949.

[28] Jacques Duffy and R.D. Mindlin. Stress-strain relation and vibrations of a granular medium. *J. Appl. Mech., ASME*, 24:585–593, 1957.

[29] K. Walton. The effective elastic moduli of a random packing of spheres. *J. Mech. Phys. Solids*, 35(2):213 – 226, 1987.

[30] P. J. Digby. The effective elastic moduli of porous granular rocks. *J. Appl. Mech.*, 48(4):803, 1981.

[31] Joe Goddard. Nonlinear elasticity and pressure-dependent wave speeds in granular media. *Proceedings of The Royal Society A: Mathematical, Physical and Engineering Sciences*, 430:105–131, 07 1990.

[32] SN Domenico. Elastic properties of unconsolidated porous sand reservoirs. *Geophysics*, 42(7):1339–1368, 1977.

[33] X. Jia, C. Caroli, and B. Velicky. Ultrasound propagation in externally stressed granular media. *Phys. Rev. Lett.*, 82:1863–1866, Mar 1999.

[34] Hernán A Makse, Nicolas Gland, David L Johnson, and Lawrence M Schwartz. Why effective medium theory fails in granular materials. *Physical Review Letters*, 83(24):5070, 1999.

[35] Yimin Jiang and Mario Liu. Granular elasticity without the coulomb condition. *Physical review letters*, 91(14):144301, 2003.

[36] Yimin Jiang and Mario Liu. A brief review of "granular elasticity". *The European Physical Journal E*, 22(3):255–260, 2007.

[37] Leonardo Trujillo, Vanessa Torres, Franklin Peniche, and Leonardo Di G Sigalotti. Towards a mathematical model for elastic wave propagation in granular materials. 2012.

[38] B Velickỳ and C Caroli. Pressure dependence of the sound velocity in a two-dimensional lattice of hertz-mindlin balls: Mean-field description. *Physical Review E*, 65(2):021307, 2002.

[39] B Gilles and C Coste. Powders and grains 2001. 2001.

[40] X. Jia. Codalike multiple scattering of elastic waves in dense granular media. *Phys. Rev. Lett.*, 93:154303, Oct 2004.

[41] XiaoPing Jia, J Laurent, Yacine Khidas, and Vincent Langlois. Sound scattering in dense granular media. *Chinese Science Bulletin*, 54(23):4327–4336, 2009.

[42] Trushant S Majmudar and Robert P Behringer. Contact force measurements and stress-induced anisotropy in granular materials. *Nature*, 435(7045):1079–1082, 2005.

[43] George C Papanicolaou, Leonid V Ryzhik, and Joseph B Keller. Stability of the p-to-s energy ratio in the diffusive regime. *Bulletin of the Seismological Society of America*, 86(4):1107–1115, 1996.

[44] Richard L Weaver. Diffusivity of ultrasound in polycrystals. *Journal of the Mechanics and Physics of Solids*, 38(1):55–86, 1990.

[45] Leopoldo R. Gómez, Ari M. Turner, Martin van Hecke, and Vincenzo Vitelli. Shocks near jamming. *Phys. Rev. Lett.*, 108:058001, Jan 2012.

[46] Leopoldo R Gómez, Ari M Turner, and Vincenzo Vitelli. Uniform shock waves in disordered granular matter. *Physical Review E*, 86(4):041302, 2012.

2. Acoustic Wave Measurements at Low Confinement Pressure

2.1. Introduction

When a jammed packing of granular material is kept under confinement pressure p_0, it exhibits an effective compressional modulus K and shear modulus G and acts as an effective medium for elastic waves [1, 2] (see section 1.3.2). Then, for a packing of spheres with Hertzian contacts, the sound speed of longitudinal waves is:

$$c_p = \sqrt{\frac{E}{\rho}}\phi^{-1/6}Z^{1/3}\left(\frac{p}{E}\right)^{1/6}\sqrt{\frac{1}{10}\frac{10-7\nu}{2-\nu}\left(\frac{12}{\pi}\frac{1}{(1-\nu^2)^2}\right)^{1/3}} \tag{2.1}$$

(2.2)

Here Φ is the volume fraction, Z is the coordination number, E_m is the elastic modulus of the sphere material, ν is the Poisson ratio of the sphere material and c_m is the longitudinal speed of sound in glass. We note that this effective sound speed can be orders of magnitude smaller than the sound speed of the bulk material. Shear and compressional wave speeds according $c \propto \Phi^{-1/6}Z^{1/3}p_0^{1/6}$ for more general granular materials such as sands and soils are well documented in the literature of soil mechanics, geophysics and engineering[3, 4]. However, the $p_0^{1/6}$ pressure dependence seems accurate only at sufficiently high pressure such that Hertzian contacts between neighboring particles can be assumed in good approximation, while for lower pressures a $p_0^{1/4}$ power-law is found for packings of glass beads and other granular materials[5, 4]. Experiments with glass beads, with bulk material elastic modulus ≈ 50 GPa, show a transition from the 1/4 to the 1/6 exponent in the $p_0 \propto 1$ MPa range[6]. Whether or not the 1/4 exponent remains valid as the pressure is decreased much further is not a priori clear and shall motivate measurements at the lowest experimentally feasible pressure.

As we increase the wave amplitude, the nonlinear terms in the expansion of the contact force become increasingly important, as do opening and closing of contacts as well as hysteresis from fictional sliding and viscoelastic damping[7]. For vanishing confinement pressure linear waves are no longer supported but the equation of motion can still be solved, yielding solitons and shock-waves, that propagate at amplitude-dependent velocity[8, 9] (see section 1.2.6). In packings of Hertzian beads close to jamming, the wavefront of a shock-wave due to a jump from the initial pressure p_0 to p_i is found to propagate at the velocity

$$\frac{v_\mathrm{shock}}{c_p} = \sqrt{\frac{2}{3}\frac{p_i/p_0-1}{(p_i/p_0)^{2/3}-1}} \xrightarrow{p_i/p_0\to\infty} \sqrt{\frac{2}{3}}\left(\frac{p_i}{p_0}\right)^{1/6} \tag{2.3}$$

The limit in the last step shows the power-law scaling due to the Hertzian contact force. Simulations[9, 10] show a cross-over from constant wavefront speed corresponding to the sound speed c_p for small p_i to the $p_i^{1/6}$ power-law at a characteristic pressure $\propto p_0$. On the other hand, experiments with continuous harmonic excitation showed a drop in sound speed corresponding to elastic weakening at large

amplitudes[7]. Thus, wave transmission at high amplitudes in terms of large dynamic to static pressure $p_i/p_0 \gg 1$ deserve to be investigated in more detail to identify under which conditions shock-like behavior arises.

In experiments of glass bead packings impacted by a piston at various speeds, shock-waves were found to be generated[11], whose wavefront speed matched Eq. (2.3) and whose dynamic pressure decayed with a power-law, not exponentially with distance:

$$p(x) = p^* \cdot \left(\frac{p(0)}{p^*} \right)^{\beta}$$
$$\beta = \mathrm{e}^{-\varepsilon x/d} \tag{2.4}$$

Here d is the bead diameter, $p^* \approx 50$ Pa and $\varepsilon \approx 0.02$. The pressure scale in this empirical attenuation model follows neither from the confinement pressure, which is in the range 1 - 10 kPa, nor from p_i, which is in the range 100 Pa - 1 MPa[11]. Experiments with shocks in the $p_i \propto 10$ Pa range and similar or smaller p_0 can give new insight into the attenuation behavior.

As measurements at low confinement pressure are obstructed by the hydrostatic gradient, it is worth considering experiments in a microgravity environment, as provided by a drop tower, an aircraft undergoing parabolic flight or a sounding rocket. Previously, sound measurements in granular media were conducted in a drop tower [12] but these experiments lacked any adjustment or even just measurement of pressure during free fall.

In this chapter of the thesis measurements of acoustic or longitudinal waves under much lower confinement pressure than previously reported are shown that were conducted in microgravity. For this purpose, an experimental setup was developed for operation on-board the *Mapheus* sounding rocket of *DLR*[13]. In June 2019, a flight was conducted, providing six minutes of measurement time under microgravity, during which sound measurements at 20 - 400 Pa confinement pressure were conducted to address the open questions mentioned above.

2.2. Preliminary Developments

Previous work at *DLR* on the measurement of elastic waves in granular media under microgravity consists of several drop tower and parabolic flight campaigns. The experimental apparatus varied from campaign to campaign but always included manual packing preparation under normal gravity and acoustic excitation by a motor-driven or electro-magnetically driven hammer hitting a plunger in contact with the packing. The technical limitations of these experiments led to inconsistent confinement pressure and poor control of the wave amplitude and shape of the excitation signal. Those were the main problems preventing meaningful elastic wave measurements.

As found by Peidong Yu (personal communication) the confinement pressure would often drop to zero upon entering the microgravity phase within seconds even when the packing was kept under compression by an adjustable piston. Such a piston could however only be adjusted manually before the drop or in-between parabolas. During the microgravity phase itself the pressure was only monitored by static force sensors without any means of performing readjustments. Various methods of preparation protocols involving multiple compression cycles and tapping by manually hitting the sample cell on all sides were used in an attempt to reach a packing configuration that would remain stable after the transition to microgravity. These methods still showed inconsistent results with the packing often getting completely unjammed even when the initial pressure after the preparation under normal gravity seemed 'large'. No pressure value under normal gravity could be found as a consistent threshold for a stable packing in microgravity.

The acoustic excitation based on a stepper-motor driven hammer suffered from limited accuracy in terms of hammer hit strength. While the stepper motor provided high torque and angular velocity and thus was well-suited for high-amplitude excitation, it lacked accuracy at the lowest amplitudes. At low

velocity, the motion of the motor and hammer is no longer well-approximated as continuous motion but rather step-like behavior with sharp corner acceleration. Additionally the absolute position of each step was unknown. This could be marginally improved by calibration techniques. However, as the absolute position changes each time the stepper-motor is power-cycled, such calibration would have to be performed before each measurement campaign. Doing this immediately before a drop or catapult shot in the drop tower without manual access to the experiment is difficult even though it has been done by the author, with limited accuracy (by repeatedly power-cycling the stepper-motor controller via remote control over a network connection until the desired signal amplitude was received). Additionally, the stepper-motor itself creates vibrations that are small compared to hammer hits at the largest used velocities but large compared to the hits at the smallest velocities. In the latter case, elastic waves are excited in the packing by these vibrations, but in a poorly controlled way and with different signal shape compared to the excitation by hammer hits. It can also be expected that the vibrations affect the packing irreversibly as they are of similar strength as hammer hits typically used in tapping protocols.

Based on the experiences in these earlier experimental campaigns it can be concluded that a new experimental apparatus must meet two requirements: firstly, the capability for not only monitoring but readjustment of confinement pressure during the microgravity phase, and secondly, an acoustic excitation system with more accurate control over the entire amplitude range without any ill-defined additional vibrations.

2.3. The Grascha 2 Apparatus

2.3.1. Requirements

The constraints of the *Mapheus* module allow for a sample cell of 12 cm x 12 cm x 13 cm size (or at least similar) which is used as the starting point for quantitative estimates.

Confinement Pressure

The lowest possible confinement pressure that can be obtained in microgravity is determined by the accuracy of the pressure control loop. A preliminary test was performed in the *ZARM* drop tower facility in Bremen in July 2017, where 10 catapult shots were performed providing 9 s of time under microgravity. The first successful algorithm for microcontroller-based re-adjustments of confinement pressure provided an accuracy around 20 Pa. It was mainly limited by noise-related uncertainty in the static force sensor readings. Based on that, an improved accuracy by one order of magnitude seemed reasonable through the use of better shielding and high-resolution dataloggers.

The largest possible pressure is determined by the range of the static force sensors and the chosen reference voltage for the ADC. As the ADC has a limited resolution (10 bit for the *Arduino Uno* and 24 bit for the *Picolog* ADC-24) a compromise must be found between high precision at low pressure and maximum range at high pressure. Another constraint is the required time resolution during readjustment of the piston. Even though high resolution measurements can be taken for later analysis, during packing preparation the 10 bit resolution of the microcontroller limits the precision. This results in a range of three orders of magnitude. We can choose the reference voltage such that the upper limit is ≈ 1 kPa, corresponding to a typical pressure in a ground-based experiment using a glass bead packing of 12 cm depth. Then the lowest pressure is ≈ 1 Pa. However, further measurement uncertainties must be considered such as accuracy of the force sensors (stability of offsets, linearity) and noise. Test measurements showed fluctuating readings within few Pa. Therefore the lowest reasonable pressure is chosen as 5 Pa.

Expected Sound Speed

We consider loose packings of volume fraction $\Phi \approx 0.63$ and coordination number $Z \approx 4$. The packings are composed of glass beads with elastic modulus $E_{\text{glass}} = 68$ GPa s and Poisson ratio $\nu = 0.24$ as well as longitudinal sound speed $c_{\text{glass}} = 5660$ m/s. Then we expect the effective sound speed in the granular medium according to (2.2) to be:

$$c_p = 3300 \frac{\text{m}}{\text{s}} \left(\frac{p_0}{7.7\text{GPa}} \right)^{1/6} \tag{2.5}$$

Therefore on ground, at $p_0 = 1$ kPa $c_p \approx 230$ m/s while in microgravity, at $p_0 = 5$ Pa $c_p \approx 100$ m/s. However, c_p could be even lower due to deviations from the $p_0^{1/6}$ power-law close to the jamming point.

Acoustic Excitation Amplitude

To reach the shock-wave regime, the excitation system must be capable of providing sufficient dynamical pressure $p_i >> p_0$. This can be expressed in terms of acceleration: a calibration measurement using a dynamical force sensor and an accelerometer of 1 cm^2 cross-section area and 5 g mass embedded in the same glass bead packing at the same distance from a vibrating wall shows a peak pressure of 245 Pa per 1 m/s^2 acceleration for short pulses of few 100 μs duration, a typical signal shape for time-of-flight measurements. This calibration result is used throughout this thesis whenever it is useful to express peak acceleration in terms of an equivalent dynamic pressure. Then, based on (2.5) and (2.3), a first estimate of the predicted wave-front speed as a function of amplitude for a variety of confinement pressures can be given, as shown in Fig. 2.1. Here, the amplitude range accessible by a stepper-motor driven hammer, a voice-coil and a single piezo transducer is also indicated, as measured in preliminary tests with accelerometers as receivers within a glass bead packing.

Based on the obtainable static pressure range of 5 - 1000 Pa we arrive at a required amplitude range of 0.02 - 4 m/s^2 in terms of peak acceleration. This can be reached using a voice-coil driven vibrating wall.

Frequency Range and Signal Shape

Furthermore, the capability of harmonic wave excitation is desirable for the measurement of frequency-dependent behavior such as attenuation and dispersion. The relevant frequency range is determined by the bead material, bead diameter, static pressure and overall sample cell size. The lowest frequency at which we can meaningfully talk about travelling waves is given by the criterion that the wavelength be much smaller than (twice) the sample cell length $\lambda \ll 2L$. The largest frequency is the cutoff frequency of the granular medium $f_c = c/(\pi d)$ as given by the estimate using the granular chain as a simplified model (see section 1.2.3).

The bead diameter must be at least several mm in order to avoid mechanical problems such as beads getting stuck in any small gaps between moving parts. For a diameter of 3 mm the cutoff frequency in a linear chain at 27 kHz at 1 kPa where c is given by Eq. (2.5) or, equivalently, by Eq. (1.54). To avoid crystallization, a bidisperse mixture of 3 and 4 mm beads with mass ratio 1:1 is chosen, making the experiments closely comparable to previous work in the literature at higher static pressures [11]. For such a mixture, being a disordered system, no clear cutoff frequency is defined. An estimation based on a bidisperse chain (see section 1.2.4) gives an estimated acoustic cutoff frequency of 15 kHz followed by a band-gap with optical cutoff frequencies 23 and 28 kHz.

According to these estimates, approximately linear dispersion is expected at few kHz. At such frequencies, pulses for time-of-flight measurements can be used, as only weak pulse-broadening will take place. Here, the excitation system must provide the amplitudes required to probe strongly-nonlinear

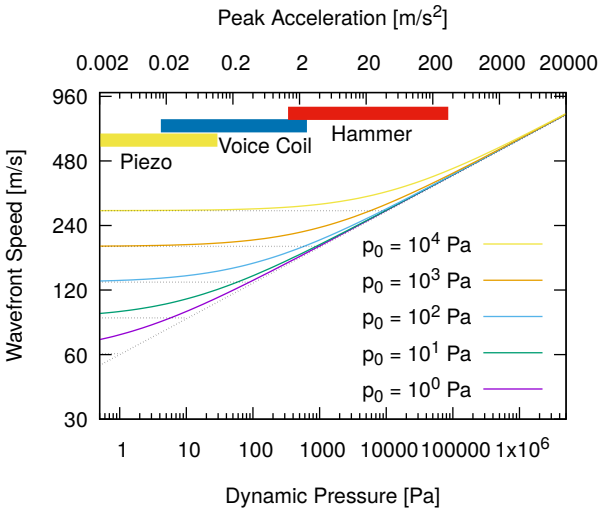

Figure 2.1.: *Estimated wavefront speed based on (2.5) and (2.3) vs. peak amplitude in terms of dynamic pressure and acceleration for different confinement pressures. Typical amplitude ranges found attainable via piezo, voice-coil and stepper-motor driven hammer are also indicated.*

wave propagation, as mentioned above. Higher frequencies, up to at least 30 kHz must also be accessible, but much smaller amplitudes are required for measurements of transmitted bandwidth, weakly-nonlinear effects and multiple scattering. Reducing the bead diameter further increases the cutoff frequencies accordingly. The low frequency limit at 5 Pa is given, following the argument in the previous paragraph, by $f_{\text{low}} = 100$ m/s $/2L = 400$ Hz. As will be shown in section 2.3.4, this frequency range can be reached with a voice-coil and power-amplifier electronics commercially available for audio applications.

Finally it is required to have the capability of excitation various waveforms suitable for various types of measurements, such as Gaussian or half-sinusoidal pulses, Gaussian tone-bursts of various width and center frequency, continuous sinusoidal signals and white noise. All of them should be available individually or as a series of increasing amplitude or frequency. Then long waveforms covering large parameter ranges can be measured at once to use the limited time in microgravity as efficiently as possible. Superpositions of harmonic signals of different frequencies can also be useful to probe weakly-nonlinear frequency mixing. Ideally, any arbitrary conceivable signal shape should be possible to use. Then numerical techniques such as inverse filtering can be used to improve the frequency response of the excitation system to make it at least as well-defined as piezo-based solutions at the high frequencies. This is actually implemented, as will be shown in section 2.3.5.

2.3.2. Setup Overview

Based on the requirements in section 2.3.1, an experimental apparatus suitable for measurements in microgravity on-board the *Mapheus* sounding rocket was built at *DLR*[14].

As shown in Fig. 2.2, the apparatus consists of two modular parts, each mounted either on top or below a base plate, which, in turn, is mounted at the center of the module container. The upper

part contains the sample cell with all sensors, the acoustic excitation system and a linear-motor driven movable side-wall that provides adjustable confinement force. The lower part contains the power-supply and Data acquisition electronics. In principle the two parts can be separated and arranged in a different configuration suitable for other types of measurements campaigns. This was done at an early stage of the development, where the module parts were used in a parabolic flight rack. This enabled us to test the pressure control loop in March 2018 under parabolic flight on-board a modified aircraft by *Novespace*. Afterwards, the module was rearranged into the configuration shown in Fig. 2.2 and prepared for the sounding rocket flight.

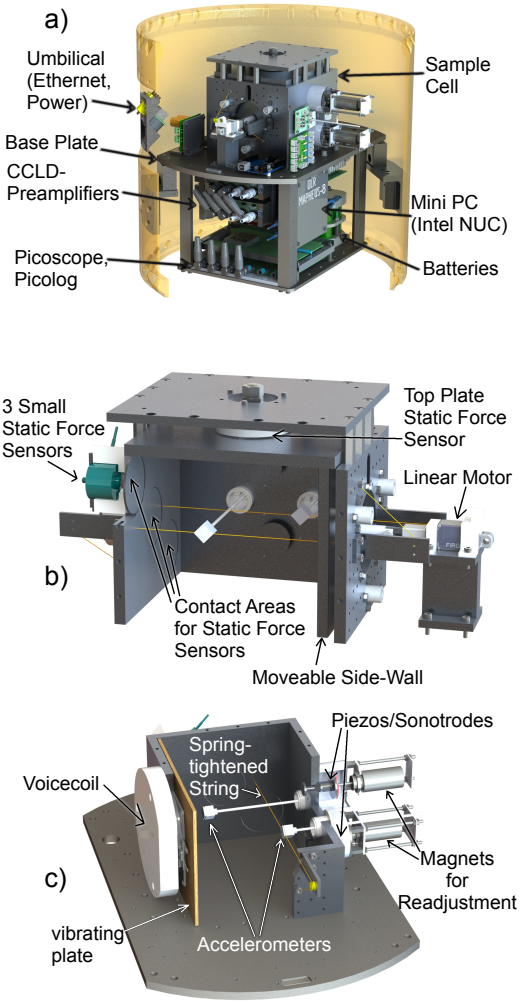

Figure 2.2.: Granular Sound module: (a) *complete apparatus inside the module container for the Mapheus sounding rocket. The upper part contains the sample cell, sensors, excitation system and pressure control system. The lower part contains pre-amplifiers, data-logger, oscilloscope and mini-PC as well as and batteries.* (b) *pressure control system with three force sensors embedded in a side-wall, one force sensor on the top and a linear-motor driven movable side-wall to compress the packing up to the desired confinement pressure.* (c) *sound measurement system with voice-coil-driven vibrating wall, two accelerometers inside the packing at 33 and 88 mm distance from the vibrating wall and two piezoelectric sensors mounted at the side-wall opposite to the vibrating wall with different areas in contact with the packing.* Taken from [14].

Upper Module Part

The upper part contains the sample cell of inner dimensions 12 cm x 12 cm x 13 cm. It is directly mounted on the base plate, which forms the bottom plate of the cell. All sample cell walls as well as the base plate are made from aluminium. The cell is closed from the top by an internal top plate mounted to a strain-gauge static force sensor (*Burster* 8432-5050) which, in turn, is mounted on a structure on top of the cell. This enables us to use the full cross-sectional area to measure the confinement pressure in terms of the static vertical force. In measurements on ground, this pressure is close to zero when the module is standing upright, or close to the hydrostatic pressure from the full weight of the packing when the module is turned upside-down. Additional static force sensors (*Burster* 8432-5005) are embedded in one of the side-walls. Three sensors are arranged in a diagonal pattern across the wall to enable measurements of the vertical pressure gradient on ground and a possible horizontal gradient in microgravity. Each sensor is in contact with the packing via a circular aluminium plate of diameter 43 mm. The pre-amplifier (*Burster* 9236) for all four force sensors is also mounted on the upper module part.

The sample cell contains an inner movable side-wall (henceforth called pressure wall). Its position can be moved inwards by up to 11 mm using a linear motor (*Actuonix* L12). This corresponds to a maximum increase in volume fraction by 9 %. The motor driver is also mounted on the upper module part along with circuit boards containing optocouplers that convert 28 V signals from the rocket's service module to 5 V signals as well as low-pass filters of 16 Hz corner frequency, used to filter the static force signals from the pre-amplifier. The filtered signals are then fed to a microcontroller (*Arduino Uno*) that is also mounted on the upper module part. The microcontroller also receives the converted service module signals and controls the linear motor driver.

A voice-coil (*Visaton* EX 80 S) is mounted on the outside of one side-wall of the sample cell such that it can drive a thin internal wall (henceforth called vibrating wall) for acoustic excitation (see section 2.3.4). The voice-coil is driven by a power-amplifier based on the *TDA* 7294 IC, a commonly used audio amplifier.

The inner surfaces of the sample cell, including the surfaces contributing to static force measurements but excluding the vibrating wall for acoustic excitation, are padded with 4 mm thick soft plastic foam. In indentation tests where the foam was compressed between flat aluminium plates by steel weights, we found a linear stiffness of ≈ 50 kPa for small indentations $\propto 10\mu$m. At ≈ 2.5 kPa applied pressure the foam was found to yield abruptly but expand back to its original shape when the pressure is released. Therefore, we deemed the foam useful in the planned pressure range < 1 kPa for measurements in microgravity. Due to its stiffness which is smaller than the effective stiffness of the granular packing, the foam provides boundary conditions of approximately constant pressure acting on the packing, as opposed to constant volume. For a more quantitative estimate, we assume an effective granular stiffness in the range 4 - 144 MPa, corresponding to a speed of sound of roughly $\approx \sqrt{E_{\mathrm{EMT}}/(\Phi \cdot \rho_{\mathrm{glass}})}$ between 50 and 300 m/s. Then we find that for the indentation of a granular chain between two foam boundaries $\delta_{\mathrm{chain}} = (120 - 2 \cdot 4\mathrm{mm}) \cdot p/E_{\mathrm{EMT}}$ and the foam indentation at the same pressure p, $\delta_{\mathrm{foam}} = (2 \cdot 4\mathrm{mm}) \cdot p/E_{\mathrm{foam}}$ the ratio $\delta_{\mathrm{chain}}/\delta_{\mathrm{chain}} \in [0.005; 0.175] \ll 1$ is small in the entire plausible pressure range. The position of the adjustable wall for a given pressure is then overwhelmingly determined by the foam indentation $\propto 10\mu$m which is well under control in the experiment, in contrast to the much smaller glass bead indentation. This shall help to reach a stable packing at any of the specified pressure settings (see section 2.3.3).

Within the sample cell, two accelerometers (*Brüel&Kjær* 4508-B) are mounted at 33 and 88 mm distance from the vibrating wall. They are located at the same height, in the center of the cell, but at different transversal distance, i.e. 2 cm off-axis distance in opposite direction, to keep them far apart from each other to avoid any interaction or shadowing. The sensors are kept in place by thin strings that are transversally crossing the sample cell. The string diameter $\ll 1$ mm is much smaller than the glass bead diameter to minimize any possible impact on sound transmission through scattering and to minimize any effect on the packing structure. Each string is kept under constant tension by a pair of

metal springs that are mounted on the outside of the sample cell. The string tension is sufficient to keep each sensor reliably within 1 mm of its specified position. However, the tension is low enough to still allow the sensor to vibrate along with the surrounding granular packing. To verify this, the restoring force upon transversal elongation of 5 mm was measured. It is found to be 0.4 N. Then, for a plausible elongation $\propto 1\mu$m due to sound transmission, the restoring force would be $\approx 80\mu$N, which is much smaller than the force acting on the sensor due to the peak dynamic pressure of the sound wave. For the latter we find $\propto 1$ mN for a $\propto 100\mu$s short pulse at the lowest amplitude setting at 88 mm distance according to calibration experiments.

Two piezo-electric sensors are embedded in the side-wall opposite to the vibrating wall. Each consists of a piezo-ceramic disk of 25 mm diameter, 2 nF capacitance and fundamental modes at 105 kHz (radial) and 1.8 MHz (thickness). The disk is glued to a machined aluminium sonotrode width a circular area of either 12.5 or 25 mm exposed to the granular packing. The larger (smaller) surface area shall provide enhanced sensitivity to the (in-)coherent part of the wave. The piezo disk itself and most of the aluminium part are contained in a cylindrical housing outside the sample cell, with plastic foam filling the space between the sonotrode or disk and the housing wall such that direct mechanical contact to the aluminium structure is prevented in order to suppress (high frequency) sound transmission through the structure to the piezo. If any adjustment of the sonotrode position is required (to prevent direct contact with the structure) or in case any glass beads get stuck between the sonotrode plate and the foam covering the sample cell wall, they can be shaken off by briefly but strongly agitating the piezo with a holding magnet mounted on the outside of the cell. The distance between the exposed sonotrode surfaces and the vibrating wall for acoustic excitation is 122 mm.

Lower Module Part

The lower module part contains the on-board power-supply containing a series of LiFePo batteries providing a nominal voltage of 24 V. The capacity of the batteries allows for up to 20 minutes of continuous operation of the experiment, whereas 7 minutes are required between liftoff to reentry. Before launch, they are charged the rocket umbilical. A second umbilical provides the ground-based power supply which is used for payload checkout tests during the countdown or for ground-based measurements in the laboratory. At liftoff, the umbilical cables are disconnected. To ensure uninterrupted power to all devices, a diode-based circuit is used to switch from external to internal power when the voltage of the external power-supply, typically at 28 V, drops below the battery voltage. The battery is connected to the module through a relay that is switched on minutes before liftoff and switched off before reentry by the *SODS* signal from the service module. During the countdown, this switching process between external and internal power is tested during payload checkout tests.

Two CCLD-preamplifiers (*Brüel&Kjær* 1704-A-002), one for the two accelerometers and one for the piezos, are mounted on the lower module part. For the accelerometers the constant current supply is used. The amplified sensor signals are recorded by an USB-oscilloscope (*Picoscope* 5442B). The oscilloscope has four channels plus an extra channel for an external trigger source (EXT) and an arbitrary wave generator (AWG) output. The AWG provides the input signal for the power-amplifier driving the voice-coil. It is connected via a T-piece to the EXT channel which enables us to trigger on the precisely known and reproducible electrical excitation signal. Therefore, even when measuring waveforms of 200 ms duration we can trigger at μs accuracy. This trigger method is also unaffected by noise or distortions that might affect the sensor signals. Due to the well-defined trigger point we have an absolute reference time available which can be useful in time-of-flight measurements.

A 24 bit ADC and datalogger (*Pico Technology* ADC-24) is used to convert and record the static force sensor signals. It allows for higher resolution but lower sample rate than the ADC of the microcontroller. Also, its input voltage range includes negative voltages. This is relevant during ground tests and laboratory measurements, where the force sensor on top of the sample cell is affected by the tensile force from the weight of the top plate. In general, both ADCs are used in parallel.

Any recorded data from the oscilloscope, the high resolution datalogger and the microcontroller is

sent to a mini-PC (*Intel* NUC i5) via USB. The NUC is equipped with a solid state hard-disk of 500 GB capacity, where data from all test runs and measurement campaigns is saved. The NUC has an Ethernet port that is exposed as umbilical connection on the module container. This enables us to have a network connection from the launch control room to the experiment just until liftoff. Similarly, in laboratory measurements, any PC can be directly connected via Ethernet to provide access to the measured data and software on the NUC. If the module is removed from its container, it is possible to connect further peripheral hardware to the NUC such as input devices, an external hard-drive and a monitor. This is however only necessary during setup of the operating system and network settings. Under normal circumstances the experiment is operated from the remote computer via SSH/SCP, RDP and a web-interface. A brief overview of the software is provided in appendix B.

As different input voltages are required for the various devices listed above, a number of DC-DC converters (*Traco*) is in use. Two of the converters are connected in series on the output side to provide the bipolar power-supply needed by the power-amplifier driving the voice-coil. The converters are installed such that heat conduction to the base plate of the module is permitted. The entire module was tested for 15 minutes in thermal vacuum using a realistic granular sound measurement protocol. All critical parts such as ICs on the NUC, oscilloscope and ADC were monitored with a thermal camera to ensure they don't overheat during the flight.

2.3.3. Packing Preparation

To enable automatic adjustment of confinement pressure under microgravity, a control loop is implemented on the microcontroller which uses the static force sensor readings as input and directs the linear motor to drive the movable inner side-wall until a specified pressure is reached. The specific algorithm for packing preparation was developed over the course of many test measurements on ground, in a drop tower campaign and in a parabolic flight campaign.

Preliminary Test in *ZARM* Drop Tower

In July 2017 the first tests of packing preparation under microgravity were conducted during a drop tower campaign at the *ZARM* facility in Bremen. Thanks to the pneumatic catapult of *ZARM*, nine seconds of microgravity time were available during each flight in the drop tower. We used 10 flights to test different implementations of the pressure control loop.

In the first attempts, the following problems were identified: Firstly, the required distance to move the pressure wall inward until a jammed packing emerges is difficult to predict based on the fill height of the sample cell. Even for a seemingly completely filled cell, once in microgravity, all static force readings drop to zero when the pressure wall is driven to its outermost position. In one case, the wall needed to be driven ≈ 1 cm inwards until the set pressure of 50 Pa was reached, which took almost nine seconds. In most other cases, after emptying and completely refilling the sample cell, the set pressure was reached within one second. While in all cases the available range of displacement of the pressure wall, as provided by the capabilities of the linear motor, was sufficient to reach a jammed packing, the adjustment was too slow. This was caused by the second problem: the raw signals of the (amplified) static force sensors contained noise such that averaging over 50 readings was necessary to get reliable values with few Pa accuracy. As these readings were taken after each iteration of the loop, the entire process of adjusting the pressure wall position could take seconds, leaving little or no time for sound measurements. The main source of this noise was found to be the DC-DC converters which operate in the 100 kHz range. Thus, all voltage measurements in the experiment (static force, acceleration, digital input pins to trigger measurements, etc.) suffer from high-frequency noise which needs to be mitigated by low-pass filtering and averaging. Proper grounding and shielding can marginally reduce the noise level but not completely remove it.

In the final configuration, we introduced 16 Hz RC-circuit low-pass filters between the force sensor preamplifier output and the ADC input. As a result, only two values were needed for averaging, yielding

similar accuracy as previously achieved with 50 readings. Then, for each loop iteration 10 ms were used, including 0.1 ms for the pressure measurement alone. The set pressure was then reliably reached within several 10 iterations, within a fraction of a second. This enabled us to perform a series of sound measurements and readjustments of confinement pressure during a single flight in the drop tower.

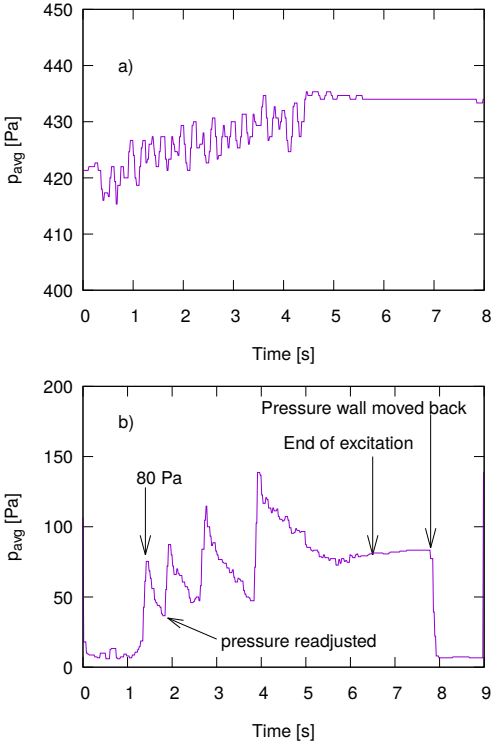

Figure 2.3.: Evolution of packing pressure as measured by force sensors in a side-wall. (a) *On ground, at initial pressure 420 Pa, it increases by 15 Pa during repeated acoustic excitation.* (b) *In microgravity, after the initial pressure of 80 Pa is reached at 2 s, the pressure decreases during excitation of the same strength as in (a) until the lower threshold of the pressure control loop is reached. Then the pressure is readjusted and the measurement is repeated three times.* Taken from [14].

In Fig. 2.3 the measured pressure acting on the side-wall containing three force sensors is shown. The actual value of the pressure was determined from the average of the three sensor readings. After the adjustment of the pressure wall was complete, the pressure was monitored under the effect of strong acoustic excitation. In this early version of the experiment we still used a stepper-motor driven hammer to generate $\propto 100\mu$s long pulses of $\propto 1$ m/s^2 peak acceleration or several 100 Pa peak dynamic pressure, as measured in the center of the packing. As can be seen in Fig. 2.3, the measured static pressure did not remain stable during the pulse transmission. In ground-based measurements close to 500 Pa a slow rise in pressure was found during acoustic excitation. In microgravity, at ten time smaller

pressure, a decrease in pressure was found during excitation at the same amplitude. Once the average pressure dropped below a specified limit, the microcontroller stopped triggering the stepper-motor and readjusted the pressure wall before continuing the sound measurement. In the drop tower flight shown in Fig. 2.3 three such readjustments were performed. After performing 20 planned hammer hits, the excitation was stopped, resulting in constant static pressure. Finally, one second before the end of the drop, the pressure wall was driven back to its outermost position, resulting in loss of confinement pressure.

Final Protocol for Mapheus sounding rocket flight

During extensive testing in 2018, a new protocol was for packing preparation was developed that reliably leads to packings exhibiting pressure that remains stable even under acoustic excitation. In Fig. 2.4 the final protocol is shown. Since a *Mapheus* sounding rocket flight provides much more time in microgravity, around six minutes, than what is available in the drop tower, we can relax use a more elaborate protocol involving multiple compression cycles and tapping, implemented by strong vibrations using the voice-coil driven wall. The time constraints for the pressure measurement can also be relaxed in favor of more accuracy. The latter is done by averaging over five readings, each taken every 10 ms.

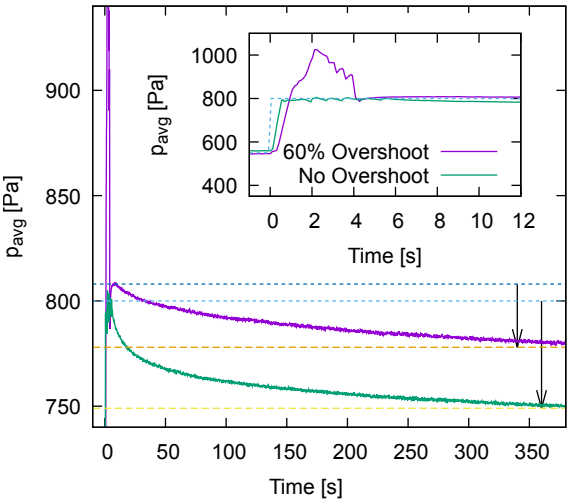

Figure 2.4.: *Confinement pressure vs. time after packing preparation with two different protocols: a side wall position is adjusted continuously with a linear-motor while the packing is vibrated by a voice-coil until the specified pressure is reached and remains stable within a specified threshold. Within few minutes a continuous pressure drop is observed. When a pressure overshoot is used (violet, upper curve) the drop is much smaller than in the case of no overshoot (green, lower curve). The inset shows both protocols in detail.* Taken from [14].

At each iteration of the control loop the motor run time is adjusted between 5 and 50 ms, instead of using just a constant value of 10 ms, as used in the drop tower campaign. Within this time range, the

run time is proportional to the error of the actual pressure, again, determined from the average of the three sensors in the side-wall, with respect to a set value. The set value is an exponentially decaying (rising) pressure with time, that approaches a constant specified value that is larger (smaller) than the initial actual value at the beginning of the readjustment. Thereby we impose a pressure overshoot (undershoot) at the start of the packing preparation if the new desired pressure is larger (smaller) than the previous pressure. An overshoot of 60 % is found to reliably result in a stable packing pressure that remains constant under acoustic excitation such as strong pulses, as typically used for time-of-flight measurements. Similarly stable packings are also found after few repetitions of the packing preparation protocol without any overshoot, but this require two or three times as much time.

The readjustment is stopped once the pressure error is found in an interval of 5 Pa or when a maximum number of iterations of 180 is reached. To ensure convergence toward a final pressure, the gain factor that multiplies the error is decaying exponentially with the number of iterations, resulting in smaller readjustment steps towards the end of the packing preparation. This is found necessary if the voice-coil based "tapping" or vibration is used simultaneously to the pressure wall position adjustment, as in general, the vibrations will affect the actual pressure, especially in the beginning of the packing preparation. To coordinate the tapping, the microcontroller sends a request for a series of strong pulses to the NUC, which then sends the appropriate commands to the oscilloscope, which uses its built-in AWG to generate the pulses, which are then fed to the power-amplifier driving the voice-coil. This mode of operation is found more reliable than an alternative method, where the NUC alone controls the timing of the pulses. The request is repeated every 200 ms until a minimum of 50 requests was sent and either the packing is found to be stable or a maximum of 100 requests was sent. The packing is considered stable if the pressure error is within 5 Pa. Until then, the pressure wall is being readjusted according to the error, as described above, but without applying any overshoot.

The protocol described so far is used for measurements on ground and in microgravity. However, extra steps and precautions are added for packing preparation in microgravity. First of all, to ensure accuracy of pressure measurements around few Pa, it must be ensured that sensor offsets do not occur or are precisely enough known. On ground, calibration measurements with force meters or known weights are performed before the measurement campaign. In microgravity, an additional calibration is performed by moving the pressure wall to its outermost position, such that the packing is unjammed and the pressure drops to zero. Any remaining sensor voltages are then identified as offsets. The microcontroller stores them in memory and subtracts them from further sensor readings. The offsets are also sent to the NUC which stores them in a logfile. Independently of this, the high resolution datalogger keeps recording the raw voltages during the entire measurement campaign. The offset calibration is performed before the preparation of each new packing. It takes three seconds.

On top of the pressure readjustment implemented on the microcontroller there are additional pressure checks implemented in the software running on the NUC, specifically *sound-control* (see appendix B). It shall be pointed out, that the above protocol does not guarantee the pressure error to be < 5 Pa. If the pressure wall readjustment was stopped due to one of the timeout criteria, *sound-control* has to decide to either accept the actually reached pressure or to direct the microcontroller to repeat the packing preparation. The pressure is accepted if the error lies within 100 Pa and the absolute pressure is larger than 5 Pa. The latter ensures the packing is jammed at all. Additional pressure checks are performed by *sound-control* before any sound-measurement i.e. before each waveform. Such a check fails if the pressure error is larger than 20 Pa or if the absolute pressure is smaller than 5 Pa. Then *sound-control* directs the microcontroller to repeat the packing preparation. In any case, no more than three consecutive preparations are allowed, to prevent an endless loop.

2.3.4. Acoustic Excitation

The voice-coil is driving a 2 mm thick glass-fibre reinforced plastic (GFRP) wall covering the full internal cross-sectional area of the sample cell. The GFRP wall is mounted to the moving part of the voice-coil exciter by four screws. In test measurements, where the wall is driven at different frequencies and the response is measured with an accelerometer (*Brüel&Kjær* 4508-B) that is mounted on the GFRP wall, the first fundamental frequency is found at 20 kHz. Thus, for smaller frequencies $\propto$ 1 kHz and pulses of width $\propto 100\mu$s, as used for time-of-flight measurements, every point on the vibrating wall is in phase within $\Delta\varphi \ll \pi$. Therefore plane waves can be excited in this frequency range in good approximation.

Test Measurements of the wall motion were conducted with the entire experimental setup placed in a vacuum chamber. Under vacuum the accelerometer signal was distorted compared to measurements under atmospheric pressure because air was trapped in two internal sealed volumes within the voice-coil. This was resolved by drilling millimeter-sized holes in the voice-coil case to let the air escape during evacuation. New measurements with the modified voice-coil showed an improved signal shape.

The excitation signal is provided by the built-in signal generator of the oscilloscope which provides elementary signal types such as sine, half-sine, steps and Gaussian pulses as well as white noise. In addition it has buffer for arbitrary waveforms of 16 k samples. In most cases, we use the latter. The software on the *NUC* (see appendix B) prepares several waveforms and loads the appropriate one for the specific measurement into the AWG buffer. For the measurement of one waveform, the software has to prepare the oscilloscope and AWG with the appropriate time-base, resolution, voltage ranges, signal amplitude, frequency and trigger settings. Depending on the wave attenuation in the granular packing and the frequency-response of the excitation system, all or many of these settings have to be adjusted for each excitation signal according to its amplitude, frequency and width, in order to provide a measurement at reasonable signal-to-noise ratio without clipping. To perform each measurement, the software arms the oscilloscope trigger, sends a trigger command for the AWG and waits for the recorded data to arrive, which is then stored to disk. For the AWG trigger command, a *UNIX*-timestamp with millisecond precision is stored, which uniquely identifies each waveform.

2.3.5. Inverse Filtering

In the previous section it was pointed out that our excitation system exhibits a resonance at 20 kHz, thus it can a priori can only provide well-defined signals at much lower frequencies. More generally, multiple sources give rise to a nontrivial frequency-response: Firstly, the vibrating wall has vibrational modes determined by its geometry. Secondly, the voice-coil, being an inductive load, exhibits increasing impedance with increasing frequency, thus acting as a low-pass filter. Furthermore, the voice-coil itself has a mechanical resonance due to the stiffness of elastic membranes providing the restoring force for the coil upon displacement against the fixed magnetic core and due to any mass, such as the vibrating wall, attached to the coil. Finally, the power-amplifier driving the voice-coil necessarily exhibits nonlinear behavior as it relies on semiconductor junctions in transistors and diodes which have nonlinear (such as exponential) voltage-current relationships. Clever circuit design with proper biasing can mitigate nonlinear distortions and provide an effective linear voltage-current relationship close to a working point in good approximation. However, signal distortions can never be completely removed and they might become significant at sufficiently large amplitudes.

While all issues mentioned above leading to a non-trivial frequency response can be mitigated through careful selection and optimization of hardware components, the extend to which this is feasible is limited if a compromise is needed for engineering reasons or to provide access to a large parameter space such as two orders of magnitude of amplitude range. In this section, another approach of improving the excitation signal is shown, which is based on digital signal processing.

Here, we treat the entire chain of power-amplifier, voice-coil and vibrating wall as a linear system with impulse response $h(t)$ such that for a given input signal $x(t)$, provided by the AWG, we obtain

an output signal $y(t)$ describing the motion of the vibrating wall, as measured by an accelerometer mounted on the wall, such that:

$$y(t) = (x * h)(t) = \int_{-\infty}^{t} x(t') \cdot h(t - t') \mathrm{d}t' \tag{2.6}$$

For convenience and to later allow faster numerical calculations, we use the convolution theorem:

$$(x * h)(t) = \mathcal{F}^{-1}[X(\omega) \cdot H(\omega)] = \frac{1}{2\pi} \int_{-\infty}^{\infty} X(\omega) \cdot H(\omega) \mathrm{e}^{i\omega t} \mathrm{d}\omega \tag{2.7}$$

where $X(\omega) = \mathcal{F}[x(t)]$ denotes the Fourier transform of the input signal and $H(\omega) = \mathcal{F}[h(t)]$ is the frequency response related to the impulse response. Then (2.6) is simply a product in the Fourier domain:

$$Y(\omega) = X(\omega) \cdot H(\omega) \tag{2.8}$$

To get the desired excitation signal $y(t)$, we wish to find the input signal $x(t)$ that solves (2.6), thus we need to calculate the inverse convolution of $y(t)$ with $h(t)$. Before we can do that, the impulse response needs to be estimated from the measurement of a probe signal $x_0(t)$ (input) and $y_0(t)$ (output). In the Fourier-domain we can naively write the empirical transfer function estimate (ETFE) as:

$$H(\omega) = \frac{Y_0(\omega)}{X_0(\omega)} \tag{2.9}$$

In real measurements we have a finite signal-to-noise ratio (SNR) as well as zeros in $X_0(\omega)$. The latter lead to isolated singularities at frequencies ω_i where $X_0(\omega_i) = 0$, which seem like resonances of the system but are only artifacts of a particular probe signal. Both issues can be mitigated by using a better estimate. Before we continue, we express (2.9) in terms of the auto- and cross-correlations or rather the respective power-densities $R_{XX}(\omega) = X^*(\omega) \cdot X(\omega)$ and $R_{YX}(\omega) = X^*(\omega) \cdot Y(\omega)$:

$$H(\omega) = \frac{R_{YX}(\omega)}{R_{XX}(\omega)} \tag{2.10}$$

To reduce the impact of isolated zeros of $X_0(\omega)$ we smoothen the power-densities by apply a Gaussian convolution kernel:

$$H_{\text{smooth}}(\omega) = \frac{(R_{YX} * W)(\omega)}{(R_{XX} * W)(\omega)} = \frac{\int_{-b}^{b} R_{YX}(\omega - \omega') \cdot W(\omega') \mathrm{d}\omega'}{\int_{-b}^{b} R_{XX}(\omega - \omega') \cdot W(\omega') \mathrm{d}\omega'} \tag{2.11}$$

Here, b is the width of the Gaussian kernel $W(\omega)$. In addition to regulating the divergent ETFE, we achieve a noise reduction of $\propto 1/\sqrt{N_b}$ if N_b frequency bins are contained in the interval $[-b; b]$ and the noise contributing to $y_0(t)$, such as white noise originating from the electronics, is uncorrelated with the input signal $x_0(t)$. We also note that, as convolution with $W(\omega)$ in the Fourier-domain corresponds to

multiplication in the time-domain with an envelope function that decays for large positive and negative time, we get a suppression of anti-causal contributions (that might arise from signal artifacts and noise) to the impulse response for $t \ll -1/b$.

In test measurements we heuristically found that introducing a term N_X, resembling a constant power-density for the input signal noise, to lead to a more accurate estimate of the frequency response:

$$H_{\text{smooth,noise}}(\omega) = \frac{(R_{YX} * W)(\omega)}{N_X + (R_{XX} * W)(\omega)} \tag{2.12}$$

If the output noise bandwidth is larger than the input signal bandwidth, the ETFE (2.10) suffers from large or infinite noisy contributions outside the input signal bandwidth. The N_X term in (2.12) suppresses such contributions.

To verify the estimated impulse response, the forward convolution of the input signal with the impulse response is calculated and the result is compared to the output signal. In addition, a visual inspection should show that $h(t)$ is roughly concentrated around $t = 0$.

All numerical calculations are implemented in *quick* (see appendix C) which uses a FFT algorithm for all Fourier-domain calculations.

Possible probe signals $x_0(t)$ are short pulses, chirps or white noise. In principle the probe signal can be of arbitrary but precisely known shape. Its bandwidth, and the bandwidth of the corresponding output signal $y_0(t)$, must be at least as large as the bandwidth of any desired excitation signal $y(t)$. In the simplest case, $y(t)$ itself is used as probe signal. An initial measurement is taken to obtain the impulse response. Then the desired signal is inversely filtered i.e. inversely convolved by the impulse response and the result is used as the new input signal, resulting in a new output signal, the motion of the vibration wall, being a much better approximation of the desired signal. In Fig. 2.5 the result is shown for a short pulse and harmonic excitation in the form of a linear chirp signal. It is shown that the inverse filtering method not only mitigates the low-pass filter and 20 kHz resonance of the excitation system but it provides an effective flat frequency response up to 40 kHz. The cost of this effective increase in accessible bandwidth is a reduction in signal amplitude. Therefor it is not suitable for excitation of strongly nonlinear waves but can be potentially useful for measurements of linear and multiply scattered waves (see chapter 3).

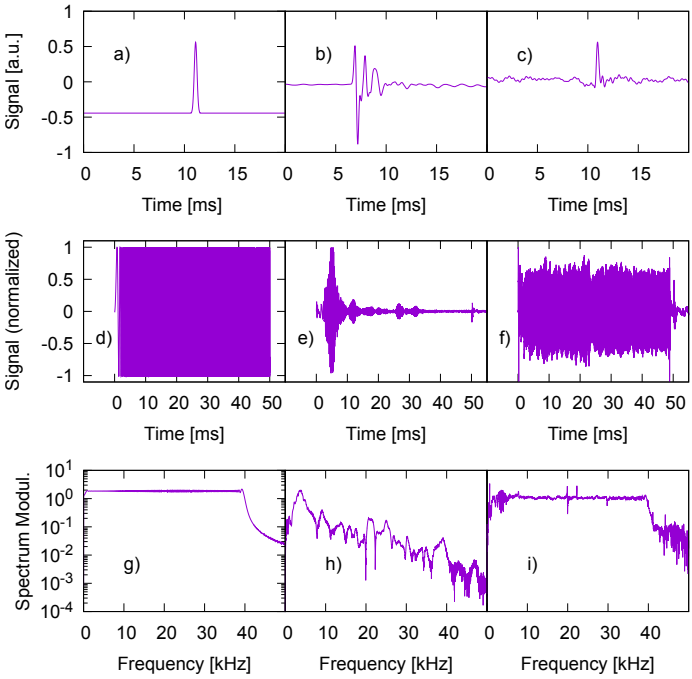

Figure 2.5.: *Desired (a,d) and measured excitation signals without (b,e) and with (c,f) inverse filtering before applying the waveform to the signal generator. The narrow pulse (a) is distorted by the excitation system (b). A much cleaner pulse (c) is obtained using inverse filtering by the system's transfer function. A similar improvement is shown for a linear chirp (d-f). The flat spectrum of this signal (g) is lost due to the system's resonances and its low-pass filter behavior (h) but can be almost recovered using the inverse filtering method (i). Taken from [14].*

2.3.6. Measurement Sequence in Microgravity

During the *Mapheus* 8 flight, six minutes were available for measurements in microgravity. To make optimal use of the time, it was planned to prepare packings at confinement pressure settings of 100, 200, 400, 50 and 20 Pa with an optional setting at 10 Pa. Additionally, a packing at 800 Pa was prepared during payload checkout tests before the launch, and again, during the flight, to prepare for reentry after the six minute period in microgravity was over.

At each pressure setting, a list of sound measurements with different signal types is conducted. To determine the speed of sound and the propagation speed of possible shock-waves, an excitation signal containing eight short pulses within 200 ms is used. In each waveform the amplitude increases by integral powers of two from pulse to pulse, spanning in total a factor of 128. This measurement is repeated 15 times for each pressure setting. The signal shape of each pulse is a half-sine of frequency 550 Hz, which is found to result in a much shorter pulse at the leading edge of the received wave, corresponding to 1.5 kHz. For a given packing configuration, the received signal shape is up to noise independent of the amplitude, with small distortions only noticeable at the largest or the largest two amplitudes. In any case, a clear pulse of 100 - 300 μs width is always received at both the close and far accelerometer in the packing. This makes the half-sine signal suitable for time-of-flight measurements.

Additional measurements are performed with serieses of Gaussian tone-bursts of fixed amplitude but increasing center-frequency of 2 - 11 kHz (40 bursts) and 10 - 29 kHz (20 bursts). Each 200 ms long series is measured four times. Additionally a 200 ms long series of eight 4 kHz Gaussian tone-bursts of increasing amplitude is measured three times. In contrast to the half-sine signal, where the oscilloscope triggers on the AWG signal that is fed to the external trigger channel, a less accurate trigger method is used for the tone-burst measurements. During the preparations of the *Mapheus* 8 mission, no reliable trigger settings for the AWG signal were found, as the signal contains no dominating peak but rather many oscillation cycles of similarly strong bursts. Therefore a software-based trigger method was used (see appendix B) that provides only ms accuracy, thus no absolute reference time is available here.

All types of sound measurements are tested before launch using the initial packing at 800 Pa. The pressure readings and measured waveforms are plotted and made available for a quick preview on the web-interface. More detailed inspection of the data is possible with command-line tools over SSH. Once the test measurements are complete and proper operation of all devices, such as the microcontroller, the oscilloscope and the high-resolution datalogger, is verified, the software enters a waiting period during which the status of all devices and the status of the signals from the service module is monitored. If necessary, additional measurements can be performed or settings for the flight can still be changed at this point. During the waiting period, and later during the flight, the software keeps all devices and related programs in a well-defined state according to the settings files. If any deviation occurs, such as a temporary loss of USB-connection or an unresponsive program, it will be corrected without the need of human intervention. Once the rocket launch occurs and the *Liftoff* signal is sent from the service module, the software anticipates the *SOE* signal within 72 s. When *SOE* is received (whether or not *Liftoff* has been received earlier) or when the timeout is reached, the preparation of the first packing in microgravity is initiated.

Each packing is prepared and measured within a time slot of 90 s. All planned waveforms must be measured within this time limit, which is feasible unless multiple readjustments of the pressure wall are necessary due to an unstable packing. Once all measurements are complete or the timeout is reached, the next packing will be prepared. If the global timeout of 366 s is reached, the software directly jumps to the last pressure setting. Therefore the optional 10 Pa setting is skipped unless much less time is needed for packing preparation and readjustments in microgravity than on ground. That setting file also contains instructions to move and compress all measured data, stop all programs and cleanly shutdown the NUC computer in preparation for reentry and landing. At 9 minutes after *SOE* the NUC is turned off, before battery power to the entire *Grascha 2* module is it cut off when the *SODS* signal is turned off by the service module.

2.4. Results

2.4.1. Force Distribution on Ground

Any granular packing prepared on on ground shows force anisotropy due to the hydrostatic gradient as well as the Janssen effect[15, 16]. To quantify it we mounted the *Grascha* module in its module container and turned it upside-down such that the large static force sensor attached to the top wall of the sample cell was at the bottom. As it covers the full cross-sectional area of the sample cell the sensor measured the full weight of the packing apart from a fraction carried by the sidewalls through frictional forces. The cell was filled with a bidisperse mixture of 3 and 4 mm glass beads at volume ratio 1:1 resulting in a total mass of 2.846 kg for the entire packing, as determined by weighing the beads with a separate scale. The force sensor in the module however showed only 20.1 N vertical force or 1.27 kPa pressure on the bottom. Therefore 28% of the packing's weight was carried by frictional forces. The average of the readings of the three static force sensors in the side-wall gives 0.45 kPa or 0.35 times the vertical force per area, compared to $\frac{1}{2}$ as expected for a perfect fluid.

Further measurements showed varying side-wall pressure results for newly prepared packings of the same total mass. The average side-wall pressure was found to vary between 400 and 600 Pa yielding a ratio of vertical to horizontal forces between 2 and 3.

2.4.2. Wavefront Speed on Ground

The test measurements of glass bead packings on ground showed wavefront speeds in the range 200 - 250 m/s with a slight increase at the largest amplitudes, as shown in Fig. 2.6. Due to the force anisotropy (see section 2.4.1) a quantitative analysis is difficult. If the pressure values are used that were obtained by averaging over the side-wall force sensors, the wavefront speed seems to roughly follow a $p_0^{1/4}$ power-law, rather than $p_0^{1/6}$. However, repeating the measurements after refilling the sample cell leads to different numerical values for the wavefront speed differing by several 10 m/s, and the minimum obtainable pressure, ranging from 400 to 600 Pa.

The group velocity for tone-burst waves, as obtained with the deconvolution method, is found in good agreement with the wavefront speed of short pulses, as obtained from the first maxima.

Further tests measurements were performed in a vacuum chamber, as shown in Fig. 2.7, where a consistent wavefront speed is found for a loose packing under atmospheric air pressure and under vacuum. Therefore the influence of interstitial air in the packing is negligible in our elastic wave measurements.

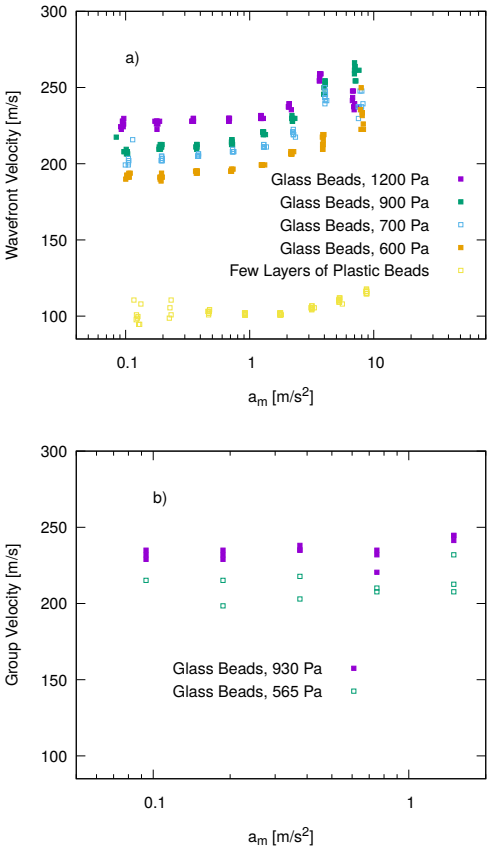

Figure 2.6.: *On-ground measurement of wavefront speed vs. amplitude for packings of glass beads at different static pressure as measured in the side-wall. Taken from [14].*

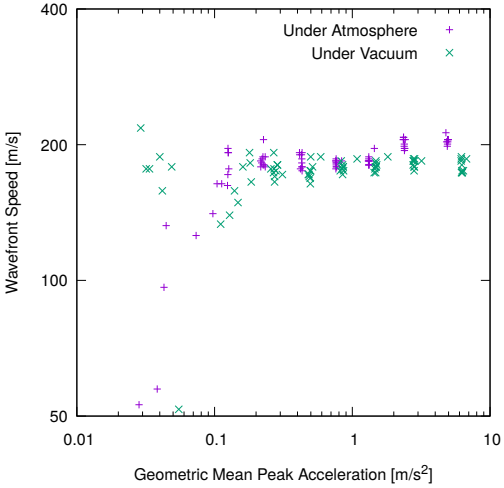

Figure 2.7.: *Wavefront speed vs amplitude in a loose granular packing, measured in a vacuum chamber under atmospheric pressure (blue crosses) and under vacuum at* $3 \cdot 10^{-3}$ *mbar (green and violet crosses). The amplitude is given in terms of peak dynamic pressure. The resulting wavefront speed is independent of air pressure.*

2.4.3. Force Distribution in Microgravity

In microgravity, the confinement pressure is determined from the normal force acting either on the side-wall, containing the three small static force sensors, or on the top wall, connected to the large area static force sensor. The resulting pressure after offset subtraction is shown in Fig. 2.8. The average of the three small sensors is in good agreement with the readings from the large sensor, indicating a much more isotropic force-distribution than in the ground-based experiments. The ratio of the pressure obtained from the top- and side-wall is shown in Fig. 2.9. In contrast to the ground-based measurement in section 2.4.1, where the ratio was close to 2.8, it is much closer to 1 for the packings prepared in microgravity.

However, the readings of the three side-wall sensors did not match exactly. In particular, one sensor close to a corner of the wall showed consistently lower force readings than the other two. The normalized standard deviation is given by:

$$\frac{\sigma_p}{p_{\text{avg}}} = \frac{1}{p_{\text{avg}}} \sqrt{\frac{\sum_{n=1}^{3} \left(p_n - p_{\text{avg}}\right)^2}{2}} \tag{2.13}$$

The standard deviation is shown in Fig. 2.10.

2.4.4. Wavefront Speed in Microgravity

Results based on time delay between the two accelerometers are shown in Fig. 2.11. Here, three analysis methods are used for comparison. Firstly, the time of arrival is obtained from the maxima of the first peak above a threshold of 0.3 relative to the maximum of each sensor signal within a region of interest of few ms around the peak. Here, the peaks are identified independently for each sensor by looking for the first local maximum of three successive data-points. Then the time difference is taken. In the second method the first peak above a relative threshold of 0.75 is identified. Here, a peak is identified as the point in a series of five points such that the average slope of the preceding two points is positive and the average slope of the remaining points is negative. The peak of the second sensor signal is obtained accordingly but with the additional condition that the peak position of the first sensor must precede the second. This method, which was found more robust against noise during ground tests, yield practically the same results as the first method, as can be seen in Fig. 2.11. Finally, a third method is used which determines the time of arrival not by the peak maximum but by a threshold for the sensor signal after DC-removal. In Fig. 2.11 a threshold of 1/e was used.The choice of the threshold in terms of a fraction of the signal maximum with a region of interest of several ms slightly influences the numerical value of the wavefront speed but it is always close to the result of the first two methods based on the peak maxima.

Ambiguities in the signal shape for different pressure settings and signal-to-noise ratio for different amplitude settings lead to uncertainty in the time-of-arrival. This affects all analysis methods mentioned above. The obtained wavefront speed is affected by uncertainties from both sensor signals. This can however be avoided by considering the time-of-arrival for each sensor separately and taking the difference with respect to a fixed reference time. In the measurements the oscilloscope used the precisely known electrical excitation signal as trigger source. Therefore a such a fixed reference time common to all waveforms is available. If we now take the fixed, known sensor positions into account, we can obtain estimates of the wavefront speed at each sensor position. In Fig. 2.12 the result is shown for the two accelerometers and one of the piezos embedded in the wall opposite to the vibrating wall. Here, the first peak maximum above a threshold of 0.75 of the signal maximum within a region of interest of few ms was used for each sensor. The obtained wavefront speed is similar to the result obtained from two sensors, but it suffers from much less spread for any given pressure and amplitude.

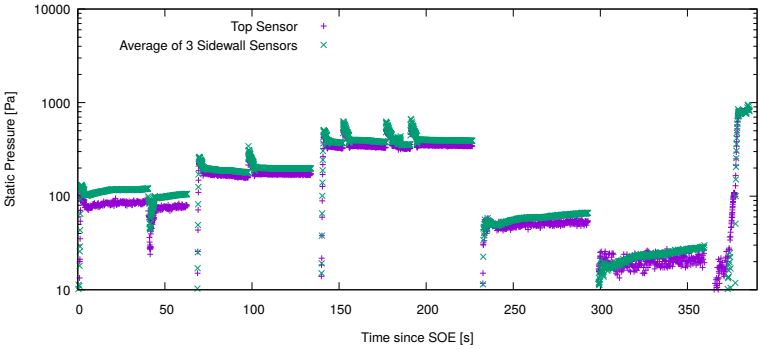

Figure 2.8.: *Static pressure during the microgravity phase of the Mapheus 8 flight as measured using the force sensor at the top of the sample cell covering the full cross-sectional area of the cell (violet crosses) and in terms of the average of the three sensors of smaller area in the side-wall (green crosses). The different pressure settings can be clearly distinguished: 100, 200, 400, 50 and 20 Pa. At the end of the microgravity phase a high pressure setting of 800 Pa was used in preparation for reentry. During the measurement phases, a few readjustment were performed: once at 100 Pa, once at 200 Pa and three times at 400 Pa. The packing pressure remained otherwise stable within the set tolerance of 20 Pa.*

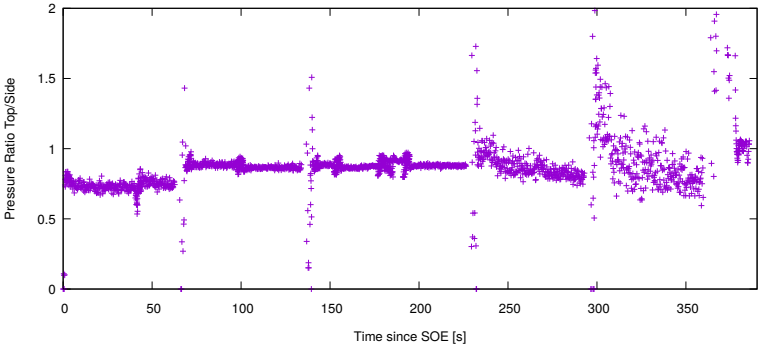

Figure 2.9.: *Force anisotropy in microgravity in terms of the ratio of pressures measured at the top and side wall. At the top wall the large static force sensor covering the full cross-sectional area of the sample cell was used, while at the side wall the average over the three sensors of smaller area was taken. Similar measurements on ground in an upside-down configuration yielded a ratio around 2.8 (see section 2.4.1).*

It is noteworthy that, at low pressure, the obtained speed at the closest accelerometer is smaller than for the far accelerometer. For the ground base measurement the opposite is true. For all pressures the speed determined from the far accelerometer and the piezo are in good agreement except at 20 Pa at the largest amplitudes.

Pressure Dependence of Sound Speed and Pulse Width

For further analysis, all received signal peaks at the wavefront were fitted by a Gaussian using the amplitude, peak position and full width at 1/e of the peak amplitude as fit parameters. This was implemented as a least-squares fit in the analysis software (see appendix section C). To keep the amplitude and width positive, only their logarithms were used in the fit algorithm. From the resulting peak positions and pulse widths an analysis of the wavefront speed was conducted resembling either the previously mentioned method using the peak maximum or the threshold method. Here the threshold 1/e is chosen, matching the value of the Gaussian at the time of the peak minus half the full width. The results from the Gaussian fit (see appendix A) are in good agreement with the above mentioned results of the signals themselves. Therefore we can treat the results from the Gaussian fit as equivalent to the results from the other methods.

The wavefront speed measurements clearly show a consistent trend of increasing speed with increasing confinement pressure. For a more quantitative analysis we shall focus on the lower amplitude settings, where the wavefront speed does not change with amplitude and can be identified with the sound speed. For highest accuracy we use the single sensor data with the peak maximum method and take advantage of the absolute timestamps of each waveform in order to determine the measured confinement pressure for each waveform separately. In Fig. 2.13(top row and bottom left) the results for second-lowest to fifth-lowest amplitude settings are shown. The lowest amplitude is omitted to avoid noise-related artifacts. The results for each of the sensors shows a pressure dependence steeper than $p^{1/6}$ and much close to either $p^{1/4}$ or $p^{1/3}$. The latter power-law fits the accelerometer data even better than the $p^{1/4}$ law, which in turn seems more accurate for the piezo data. However, to clearly distinguish between the two exponents, these measurements are not accurate enough.

The small but noticeable discrepancy in the wavefront speed determined either from the threshold or peak maximum implies a change of signal shape, more specifically, the pulse width, as a function of propagated distance. In Fig. 2.13(bottom right) the width is plotted against the confinement pressure. To focus only on weakly nonlinear wave propagation and also avoid noise-related artifacts, only the second-lowest to fifth-lowest amplitude settings are shown. If the pulse broadening is related to wave dispersion then it must scale like the cutoff frequency and the sound speed. For comparison with the power law behavior of the sound speed fits for hypothetical pressure dependency $p^{1/4}$ and $p^{1/3}$ are shown also in Fig. 2.13 (bottom right).

Amplitude Dependence of Wavefront Speed

If the amplitude is normalized by the static pressure and the wavefront speed is normalized by the linear sound speed for low-amplitude waves, all points should be described by the dimensionless shock-wave speed given by Eq. (2.3). In Fig. 2.14 the results are shown in case of a linear sound speed of 125 m/s $\cdot(p_0/400\text{Pa})^{1/3}$ at the close accelerometer and 160 m/s $\cdot(p_0/400\text{Pa})^{1/3}$ at the far accelerometer. For each sensor the peak position relative to the fixed reference time from the trigger point was used. The normalized data points do not fully collapse on the prediction (2.3. Deviations arise especially at the higher pressure settings, where the wavefront speed at high amplitudes is found to drop below its value at low amplitudes.

2.4.5. Attenuation of Wavefront

In Fig. 2.15 the attenuation of the wavefront is plotted in terms of the peak amplitude at the close and far accelerometers. The amplitudes are expressed as dynamical pressure with $p_{\mathrm{dyn}} \approx 245. \frac{\mathrm{Pa}}{\mathrm{m/s^2}} \cdot a$. A fit of the power-law attenuation model (2.4) to data points from all pressure settings shows good agreement for $p^* = 10$ Pa and $\varepsilon = 0.02$ while using an average particle diameter of 3.5 mm and the distance 56 mm between the close and far sensors.

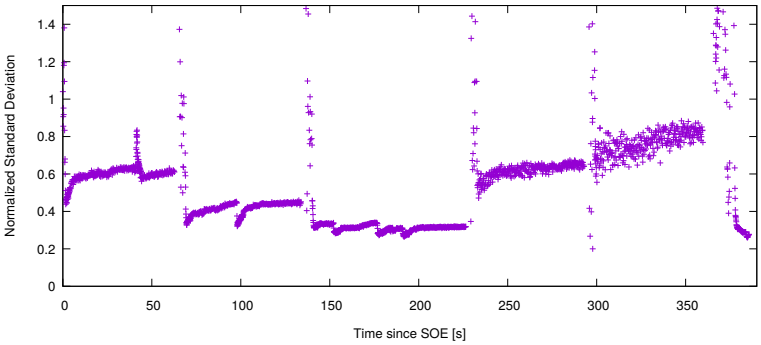

Figure 2.10.: *Standard deviation of static force at different positions at the side-wall in microgravity as given by Eq. (2.13).*

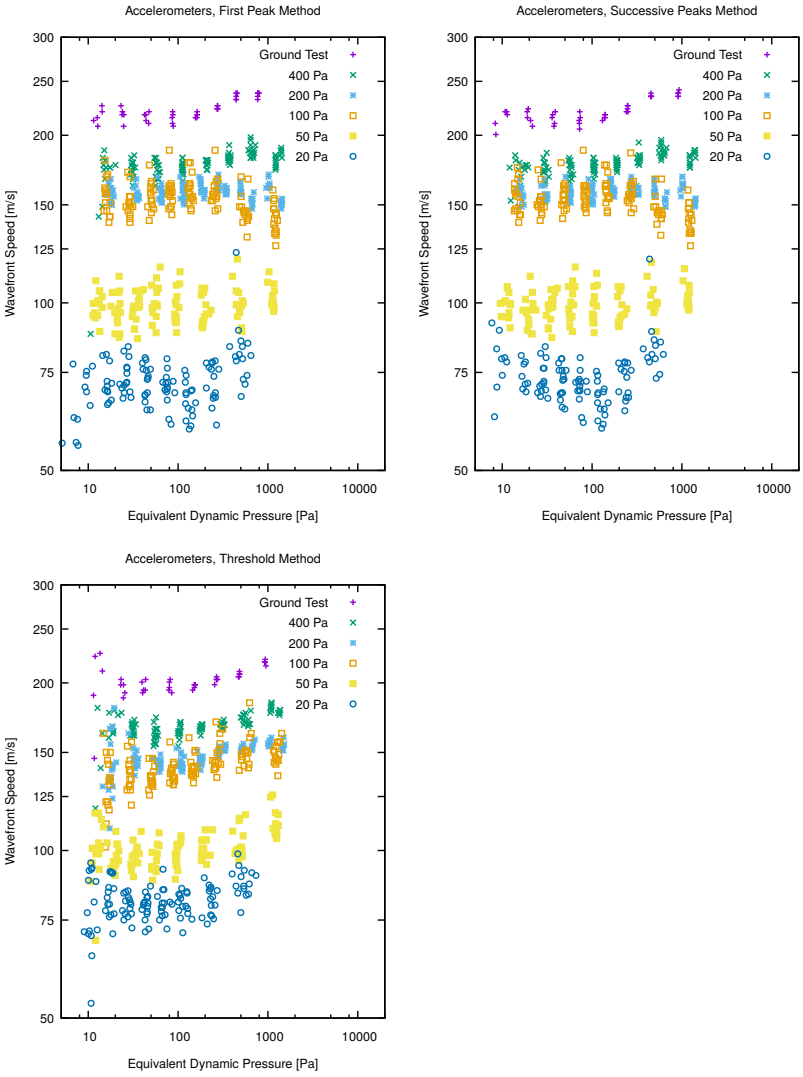

Figure 2.11.: *Wavefront speed determined from two accelerometers within the packing. Using the either the first peak position for each sensor signal or the first two successive peak position for the two signals gives the same result. Using a relative threshold of 1/e instead results in slightly lower speed especially at the highest pressure settings. All three methods suffer from inaccuracy due to uncertainties of the close accelerometer signal, especially effecting measurement of higher speeds.*

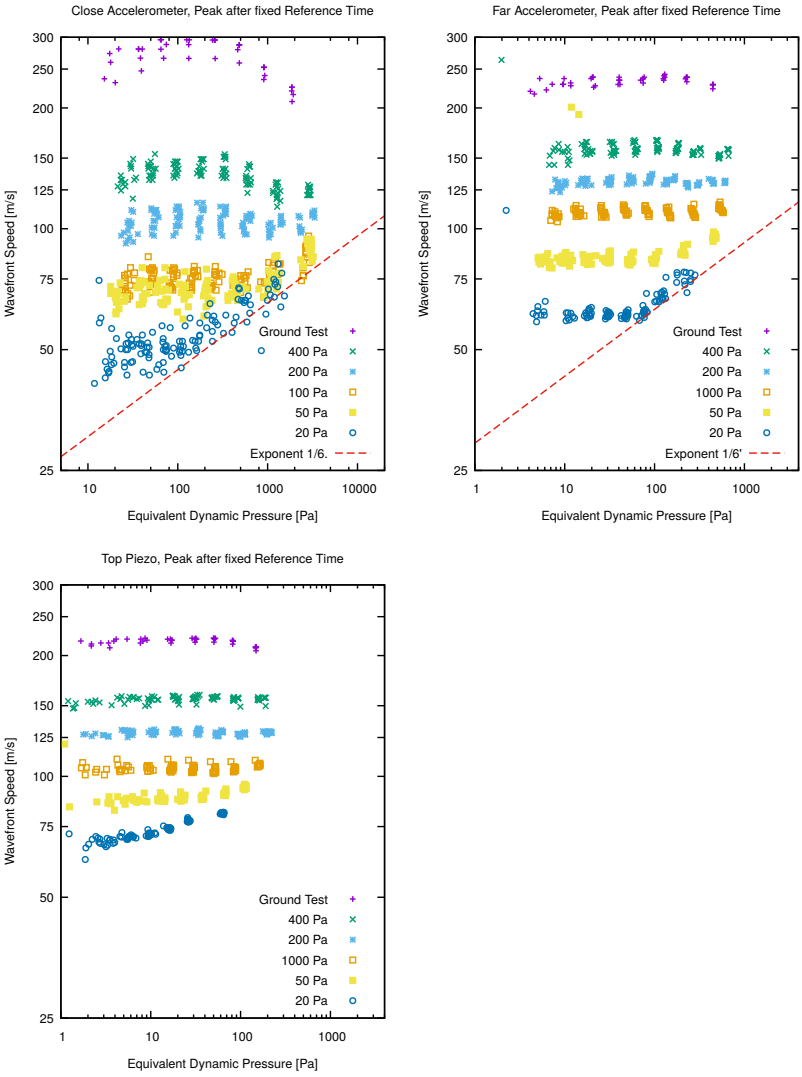

Figure 2.12.: *Wavefront speed determined from peak of each single sensor signal relative to fixed reference time given by the oscilloscope trigger point on the AWG excitation signal. Shown are results for the accelerometers at 33 and 88 mm distance from the vibrating wall as well as one of the piezos at 122 mm. For the lowest pressure setting and the highest amplitude settings an increase of speed with amplitude is found as indicated by a power-law fit of exponent 1/6 according to the shock-wave model.*

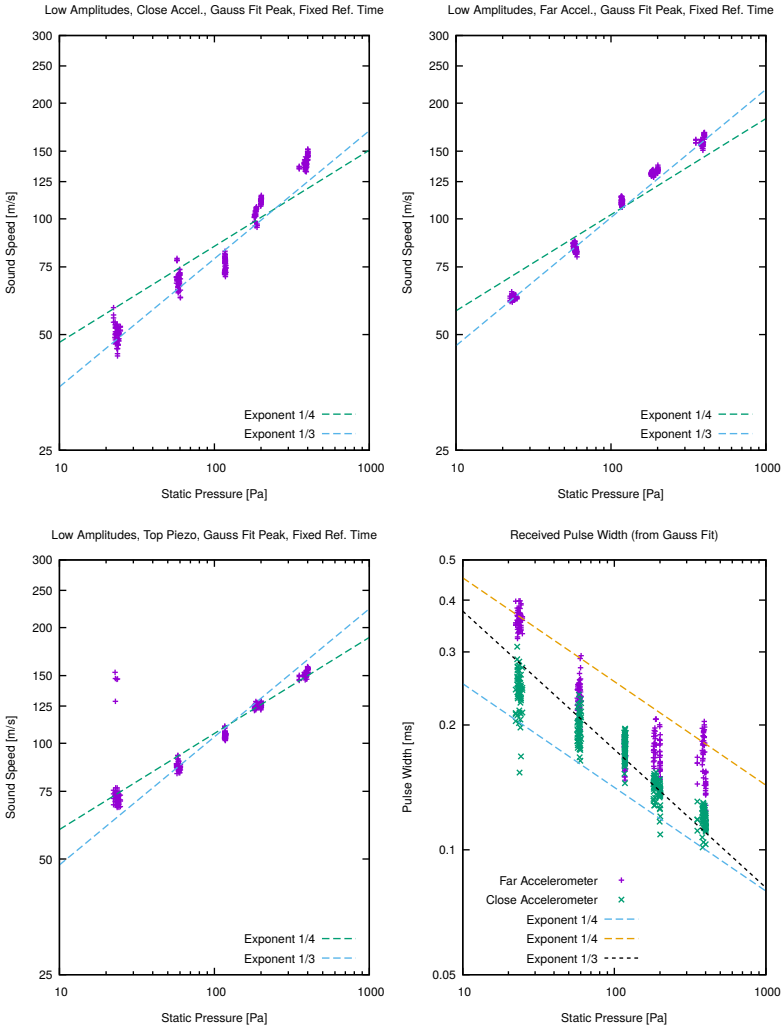

Figure 2.13.: Top row and bottom left: *Linear wave speed vs static pressure as determined from amplitude settings* $\propto 2^{-6}$ *to* 2^{-3} *relative to maximum amplitude. The speed wave determined from the peak position of each sensor relative to the fixed reference time. To make the peak position more accurate and robust against noise and distortions, a Gaussian was fitted to the signal. For comparison, power-law dependencies on the static pressure with exponents 1/3 and 1/4 are shown as is characteristic for low-pressure elastic behavior of granular packings.* Bottom right: *Pulse-width vs. static pressure as determined from Gaussian fit of accelerometer signals as amplitude settings* $\propto 2^{-6}$ *to* 2^{-3} *relative to maximum amplitude. Similarly to the power-law behavior of the low-amplitude wave speed, an exponent between 1/4 and 1/3 fits the data.*

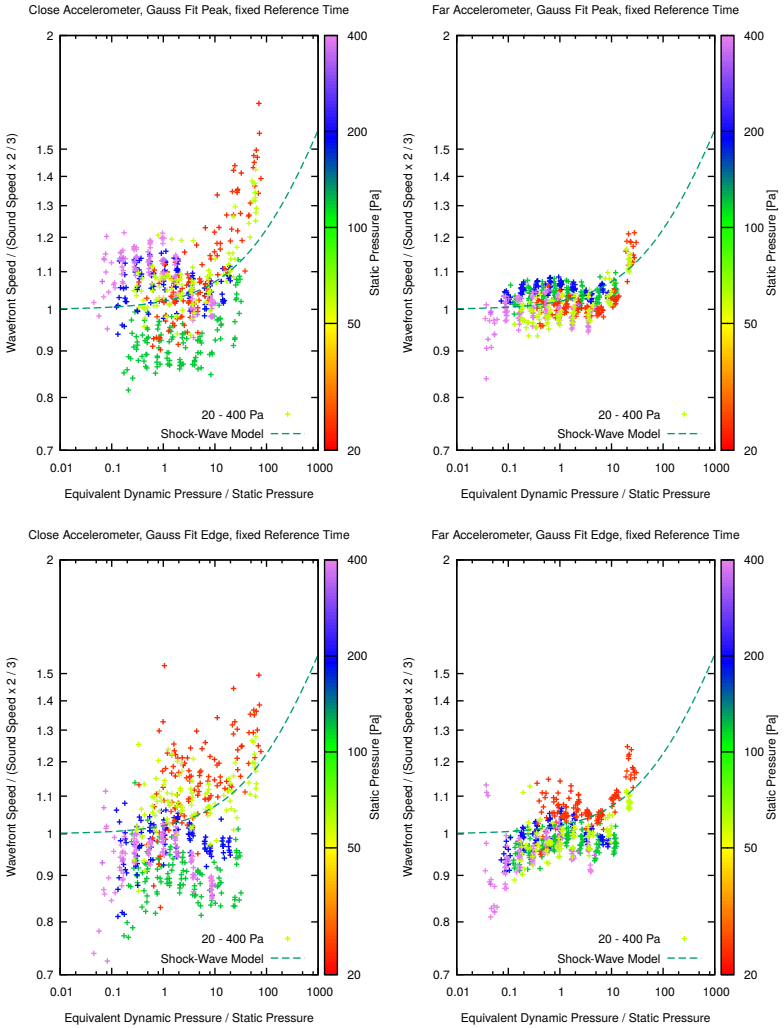

Figure 2.14.: Top row: *Normalized wavefront speed from peak position of Gaussian fit relative to reference time is plotted against normalized amplitude.* Bottom row: *Results for the edge (1/e threshold) based method of the same Gaussian fits. The linear sound speed is assumed to follow a pressure power-law of exponent 1/3 and its prefactor is taken from the low amplitude fit shown in Fig. 2.13 and similar fits for the edge-based method. Despite considerable spread of the measured data around the prediction of the shock-wave model (dashed line, following Eq. (2.3)) the lowest two pressure settings show the onset of the strongly nonlinear regime characterized by rising wavefront speed at the largest amplitude settings.*

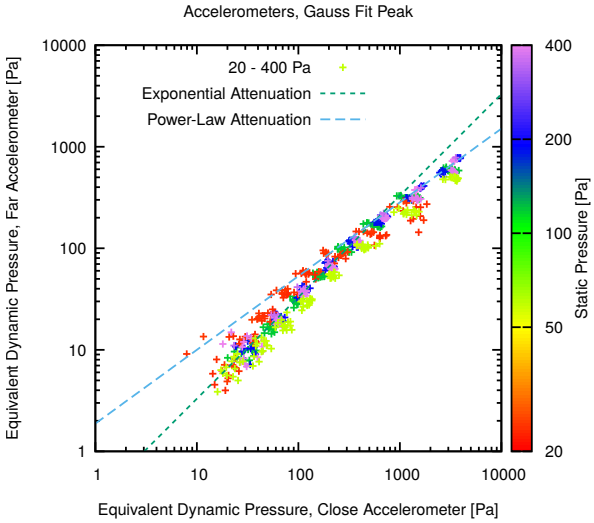

Figure 2.15.: *Attenuation of wavefront amplitude in terms of peak dynamical pressure that is proportional to peak signal of accelerometers within the packing at different static pressure settings. The peak was determined from the Gaussian fits. Most of the amplitude range exhibits a constant attenuation factor (dashed line of slope 1). Only the highest amplitude settings show a deviation, as indicated by the dashed line of slope* $e^{-0.02x/d} \approx 0.726$ *similar to the power-law behavior postulated by v.d. Wildenberg et al.[11].*

2.5. Discussion

2.5.1. Linear Regime

For Hertzian contacts the sound speed follows a $c_p \propto p_0^{\nu}$ power-law dependence with exponent $\nu = 1/6$. The ground-based measurements of the low-amplitude wave speed in section 2.4.2 show a stronger pressure dependence close to $\nu \approx 1/4$. An even stronger pressure dependence with $\nu \approx 1/3$ appears at the smallest pressures as measured in microgravity in section 2.4.4. When we also take into account literature values for ν measured at much higher confinement pressure[6] we find that all results are well-described by

$$\nu(p_0) = \nu(p_{ref}) - \beta_0 \cdot \log\left(\frac{p_0}{p_{ref}}\right) \tag{2.14}$$

such that in any small pressure range the sound speed is approximated by a power-law, so its logarithmic derivative is given by

$$\frac{\mathrm{d}(\log(c_p))}{\mathrm{d}(\log(p_0))} = \nu(p_0) \tag{2.15}$$

from which we obtain for any pressure p_0:

$$\frac{c_p(p_0)}{c_{ref}} = \mathrm{e}^{\nu_{ref}\log(\frac{p_0}{p_{ref}}) - \frac{1}{2}\beta_0\left(\log(\frac{p_0}{p_{ref}})\right)^2} \tag{2.16}$$

where $\nu_{ref} = \nu(p_{ref}) = 1/6$ corresponds to the exponent resulting from Hertzian contact forces, which is known to be valid at sufficiently high pressure p_{ref}. Equivalently, the pressure p_0 and exponent $\nu(p_0)$ at that pressure can be inserted in (2.16) if it is known from measurements, while β_0 remains unchanged. In Fig. 2.16 a fit is shown that indicates the slope $\frac{\mathrm{d}\nu(p_0)}{\mathrm{d}(\log(p_0))} = \beta_0 \approx 0.012 \pm 0.002$ is constant across at least five orders of magnitude of confinement pressure. The equivalent fit of (2.16) to the sound speed, taking into account the low-amplitude results from the close and far accelerometers (see Fig. 2.13) as well as literature results (see Fig. 4 in [6]), is shown in Fig. 2.17.

This fit model can be interpreted in terms of the Jiang-Liu elasticity (see [17] and section 1.3.3) if we assume a and b in (1.124) and thus also ν to be monotonous functions of p_0. Then, for a given reference pressure scale $\log_{10}(p_{ref})$ we get an effective theory of elasticity. Small deviations of the confinement pressure p_0 lead to deviations of the effective elastic moduli proportional to $(p_0/p_{ref})^{\nu}$ where ν is given by (2.14). For large deviations the power-law is modified by terms arising from the non-constant ν. The continuous pressure dependence of the exponents ν or a and b at any pressure implies a continuous transformation between any effective Jiang-Liu theories defined at different reference pressures. Then, if one assumes the exponents $a = b = b(p_0)$ and uses $\nu(p_0) = 1/(2+2/b(p_0))$ as in [17] then (2.14) leads to

$$b(p_0) = \frac{1}{\frac{1}{\frac{1}{1+\frac{1}{b_{ref}}} + 2\beta_0\log(\frac{p_0}{p_{ref}})} - 1} \tag{2.17}$$

which tends to zero at high pressure $\propto 10$ GPa, comparable with the elastic modulus of the bulk material (glass), implying linear elasticity, and to infinity at small pressure $\ll 1$ Pa, implying $c_p \propto p_0^{1/2}$

at the jamming point. If p_{ref} is arbitrarily chosen close to the bulk material elastic modulus, then $b_{ref} = 0$ and (2.17) reaches its simplest form.

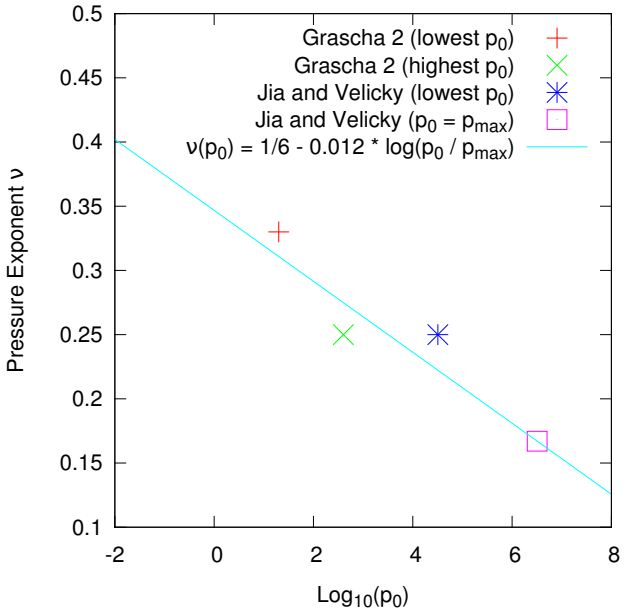

Figure 2.16.: *Exponent ν for $c_p \propto p_0^{\nu}$ pressure dependence vs logarithm of confinement pressure. The points show the exponents obtained from measurements in microgravity (see section 2.4.4) and on ground (see section 2.4.2) as well as the smallest and largest values obtained by Jia et al.[6]. The line shows a fitted trend according to Eq. (2.14) corresponding to a constant slope (see Eq. 2.15).*

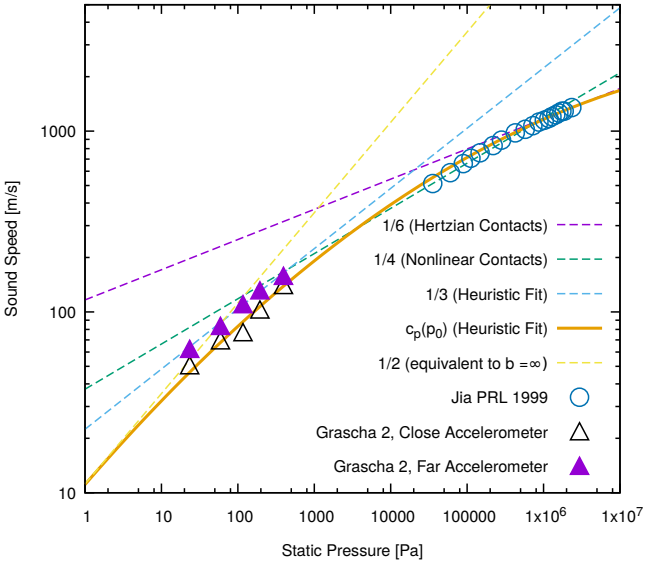

Figure 2.17.: *Pressure dependence of the sound speed (measured in section 2.4.2, see Fig. 2.13, here shown as triangles, and literature values from Fig. 4 in [6], shown as circles) fitted with local power-laws of exponents 1/6, corresponding to Hertzian contacts at high pressure, as well as 1/4 and 1/3 at low pressure (dashed lines). The heuristic model denoted $c_p(p_0)$, given by Eq. (2.16), fits the entire pressure range (solid line). A hypothetical 1/2 power-law is also shown (yellow dashed line).*

2.5.2. Nonlinear Regime

The results in Fig. 2.14 are not as clear as in previous measurements on ground reported in the literature[11]. Qualitatively, a transition from near constant wavefront speed at low p_i/p_0 to rising speed at p_i/p_0 is found. The fit of the shock-wave speed based on Hertzian contacts (2.3) corresponds to a $p_i^{1/6}$ dependence at high amplitudes. However, a similar fit can be applied to the data in Fig. 2.14 based on the amplitude in terms of particle velocity, which is obtained from integrating the measured acceleration signals. Then the high amplitude asymptotic would be $v_{particle}^{1/5}$, assuming a constant ratio of kinetic and potential energy for Hertzian contacts (as in Eq. (1.63) in section 1.2.6). However, examining the peak acceleration, used to estimate p_i, and the peak particle velocity (see Fig. A.3 in appendix A) shows they can not be distinguished from the available data.

Deviations from (2.3) at the highest two pressure settings are found, especially when the analysis considers only the signals from the close accelerometer in Fig. 2.14, where the wave amplitude is about five times larger than at the far accelerometer. There, a drop in the wavefront speed occurs at the highest amplitude settings. An analysis of the resemblance of successively measured waveforms, which could provide evidence for microscopic changes of packing configuration related to elastic weakening[7], was attempted (see Fig. A.1 in appendix A) but found inconclusive.

2.5.3. Attenuation

The results shown in Fig. 2.15 show a constant attenuation factor for most amplitude settings but increased attenuation at the largest amplitudes. This behavior is in agreement with the power-law attenuation model (2.4) proposed by v.d. Wildenberg et at[11] if $p^* = 10$ Pa and $\varepsilon = 0.02$ are used for the fit. In v. d. Wildenberg's work p^* is found at 50 Pa. The discrepancy could be attributed to the uncertainty in the transition between constant and increased, amplitude-dependent attenuation. At sensor-sensor distances ≈ 50 mm the exponent $\beta = \exp^{-\varepsilon x/d} \approx 0.77$ is still close to 1, making it difficult to distinguish the two attenuation regimes. Further measurements at larger distances could provide more accuracy. At least the order of magnitude is clearly the same for the data presented here and in [11].

For the coefficient ε (or ε_s in [11]) the value 0.020 ± 0.005 is found. The coefficient in [11] is clearly the same, even though the numerical value reported in [11] is wrong. Repeating the fit of (2.4) to the data shown in Fig. 4 and 5 in [11] yields $\varepsilon_s = 0.021 \pm 0.05$, in agreement with the result of this thesis.

2.6. Conclusion and Outlook

Measurements of acoustic waves in glass bead packings at low confinement pressure p_0 from 20 to 400 Pa were conducted in microgravity on-board the *Mapheus* sounding rocket. A stable packing was reached at each planned pressure setting and the normal force distribution was found close to isotropic, in stark contrast to ground-based experiments. The low-amplitude wave-front speed was found to be independent of amplitude. Its pressure dependence is well approximated by a $c_p \propto p_0^{1/3}$ law, in contrast to the Hertzian prediction of $p_0^{1/6}$, known to be valid at high pressure, and the widely-reported low-pressure behavior $\propto p_0^{1/4}$. However, literature values and the results of this thesis, measured at much lower pressure can be described by a continuous transition of the exponent from $1/3$ to $1/6$, corresponding to a constant logarithmic derivative across at least six orders of magnitude of p_0. Qualitatively, this is similar to the continous transition found for two-dimensional systems in [18]. In the future, studies of the contact force law across as many orders of magnitude could lead to insight of the microscopic mechanism of this transition. However, if stress disorder is the origin of the transition, as argued in [18], then studies of wave scattering (see chapter 3 of this thesis) could provide valuable insight. Further sound measurements with additional pressure settings could also make our knowledge of the pressure dependence more quantitatively accurate. If the accuracy of the pressure control loop could be increased by a factor of ten, e.g. by using the existing sensor with large surface area instead or in addition to the average of the smaller sensors, then even a direct test of the $c_p \propto p_0^{1/2}$ behavior predicted at $p_0 \approx 1$ Pa could become feasible with the existing experimental apparatus.

The high-amplitude behavior is found to show shock-like behavior, characterized by rising wave-front speed with increasing amplitude, at the lowest pressure settings. However, at higher confinement pressure the results for the largest amplitudes can not be unambiguously interpreted. A drop in wave-front speed indicates elastic weakening due to the strong acoustic excitation. Further measurements with different signal shapes could provide insight into possible microscopic changes in the packing configuration. A new set of signals with different alternating low and high amplitude signals is currently being tested for use in a future campaign. This would enable us to compare the resemblance of repeated measurements at different amplitudes to probe the onset of rearrangements in the force-chain network.

The attenuation of short pulses is mostly well-described by a constant attenuation factor. At the largest amplitudes the attenuation is found to be stronger. It is well-described by the power-law model proposed by v.d. Wildenberg et al.

In this chapter, even the behavior of low-amplitude waves was found to be non-trivial. Therefore elastic waves shall be studied further beyond the effective medium theory, e.g. by taking the effect of nonlinear contact-forces and disorder as scattering sources into account. In the next chapter this will be attempted by considering multiple scattering and diffusive transport of elastic waves.

Bibliography

[1] Jacques Duffy and R.D. Mindlin. Stress-strain relation and vibrations of a granular medium. *J. Appl. Mech., ASME*, 24:585–593, 1957.

[2] K. Walton. The effective elastic moduli of a random packing of spheres. *J. Mech. Phys. Solids*, 35(2):213 – 226, 1987.

[3] P. J. Digby. The effective elastic moduli of porous granular rocks. *J. Appl. Mech.*, 48(4):803, 1981.

[4] Joe Goddard. Nonlinear elasticity and pressure-dependent wave speeds in granular media. *Proceedings of The Royal Society A: Mathematical, Physical and Engineering Sciences*, 430:105–131, 07 1990.

[5] SN Domenico. Elastic properties of unconsolidated porous sand reservoirs. *Geophysics*, 42(7):1339–1368, 1977.

[6] X. Jia, C. Caroli, and B. Velicky. Ultrasound propagation in externally stressed granular media. *Phys. Rev. Lett.*, 82:1863–1866, Mar 1999.

[7] X. Jia, Th. Brunet, and J. Laurent. Elastic weakening of a dense granular pack by acoustic fluidization: Slipping, compaction, and aging. *Phys. Rev. E*, 84:020301, Aug 2011.

[8] VF Nesterenko. Propagation of nonlinear compression pulses in granular media. *J. Appl. Mech. Tech. Phys. (Engl. Transl.)*, 24(5):733–743, 1983. Translated from Zhurnal Prikladnoi Mekhaniki i Tekhnicheskoi Fiziki, No. 5, pp. 136-148, September-October, 1983.

[9] Leopoldo R. Gómez, Ari M. Turner, Martin van Hecke, and Vincenzo Vitelli. Shocks near jamming. *Phys. Rev. Lett.*, 108:058001, Jan 2012.

[10] Leopoldo R Gómez, Ari M Turner, and Vincenzo Vitelli. Uniform shock waves in disordered granular matter. *Physical Review E*, 86(4):041302, 2012.

[11] Siet van den Wildenberg, Rogier van Loo, and Martin van Hecke. Shock waves in weakly compressed granular media. *Phys. Rev. Lett.*, 111:218003, Nov 2013.

[12] X Zeng, JH Agui, and Masami Nakagawa. Wave velocities in granular materials under microgravity. *Journal of Aerospace Engineering*, 20(2):116–123, 2007.

[13] Martin Siegl, Florian Kargl, Frank Scheuerpflug, Jörg Drescher, Christian Neumann, Michael Balter, Matthias Kolbe, Matthias Sperl, Peidong Yu, and Andreas Meyer. Material physics rockets mapheus-3/4: flights and developments. In *Proceedings of the 21st ESA Symposium on European Rocket and Balloon Programmes and Related Research*, volume 9, page 13, 2013.

[14] Karsten Tell, Christoph Dreißigacker, Alberto Chiengue Tchapnda, Peidong Yu, and Matthias Sperl. Acoustic waves in granular packings at low confinement pressure. *Review of Scientific Instruments*, 91(3):033906, 2020.

[15] H. A. Janssen. Versuche über Getreidedruck in Silozellen. *Zeitschr. d. Vereines deutscher Ingenieure*, 39:1045–1049, 1895.

[16] Matthias Sperl. Experiments on corn pressure in silo cells–translation and comment of janssen's paper from 1895. *Granular Matter*, 8(2):59–65, 2006.

[17] Leonardo Trujillo, Vanessa Torres, Franklin Peniche, and Leonardo Di G Sigalotti. Towards a mathematical model for elastic wave propagation in granular materials. 2012.

[18] B Velickỳ and C Caroli. Pressure dependence of the sound velocity in a two-dimensional lattice of hertz-mindlin balls: Mean-field description. *Physical Review E*, 65(2):021307, 2002.

3. Measurement of Multiple Scattering

3.1. Introduction

The previous chapter was only concerned with measurements of the wavefront, determined by the first arrival or peak of a sensor signal, as a result of a short pulse-like excitation. The wavefront speed for low-amplitude elastic waves in jammed granular packings is well-described by Effective Medium Theory(EMT)[1, 2, 3] in terms of the volume fraction Φ, coordination number Z and confinement pressure p_0 as $c \propto \Phi^{-1/6} Z^{1/3} p_0^{1/6}$ if the particles constituting the packing are interacting via Hertzian contacts. The latter is a good approximation at sufficiently high confinement pressure, whereas for lower pressure a different pressure dependence $c \propto p_0^{1/4}$ arises[4, 5]. In all cases, an effective Jiang-Liu elasticity[6, 7] describes the wavefront speed in a given pressure range. However, these effective medium approaches neglect the microscopic structure of the packing and thus can not be entirely accurate. Indeed, apparent discrepancies are found when the full received signal beyond just the first arrival of the wave is taken into account. Determining the group velocity from either the time-of-flight as $v_{tof} = \delta x / \delta t$, taking into account the first arrival after propagation of the distance x, or from the frequency-derivative of the phase-shift $v_g = 2\pi\delta x / (\frac{\mathrm{d}\phi}{\mathrm{d}f})$, taking into account the entire signal, was found to yield different results $v_{tof} \approx 280$ m/s and $v_g \approx 60$ m/s [8]. Furthermore, v_g was found to be very sensitive to small bead rearrangements while v_{tof} remained unaffected.

More insight is gained from studying a large ensemble of packings that are independently prepared with the same preparation protocol at the same volume fraction and confinement pressure, but which differ microscopically. The average or coherent signal is well-described by EMT and well reproducible, while the configuration-specific or incoherent contribution of the signal is dominated by larger times of arrival[9]. After excitation by a short pulse or burst, the received signal is a superposition of a pulse-like coherent signal and an incoherent signal of much longer duration. The latter is highly irregular in time but reproducibly measurable for the same packing configuration. The incoherent signal gives the main contribution to the total signal after the initial coherent pulse has passed, hence it is often identified with the tail or coda that follows the initial or ballistic signal[10, 11], reminiscent of the long-duration coda of seismic waves studied in geophysics[12]. For wave measurements at small sample thickness or source-receiver distance, the coherent and incoherent signals can substantially overlap, which affects especially the shear wave, which propagates at smaller sound speed than the longitudinal wave. Thus, a conveniently appearing identification of the ballistic signal with the coherent signal, and of the coda with the incoherent signal, only applies to sufficiently large systems where the two are clearly separated in time. It is also interesting to note that the ballistic signal, often found to be dominated by low frequencies even after excitation with a high frequency burst, results from nonlinear demodulation within the first layers of beads close to the source, instead of being generated directly from the excitation source itself[11].

The highly irregular but reproducible configuration specific nature of the incoherent signal along with its long duration, compared to the excitation signal and to the coherent signal, suggests that it results from the interference of waves propagating through the packing along various paths of different length, possibly involving multiple reflections until it is dissipated by inelastic absorption[9]. Increasing the surface area of the receiving sensor relative to the bead size results in a suppressed incoherent signal in favor of the coherent signal[9], similar to the effect that ensemble averaging has on the signal. The incoherent signal thus seems to probe the random inhomogeneities in the granular elastic medium analogous to how optical speckle patterns probe optical (dielectric) inhomogeneities[13]. This be-

havior can be treated as multiple scattering in a random (but still continuous) medium [14], which has been studied for many different types of waves (acoustic, elastic, electromagnetic, quantum-mechanical wave functions of electrons in solids)[15, 16, 17, 18, 19, 20].

For the granular packing, the question arises, what is the medium and what are the inhomogeneities acting as scatterers, as the measured sound wave is not transmitted by an interstitial homogeneous medium but by the particles, such as glass beads, which constitute the packing, and the force-carrying contacts through which they are interacting with each-other. Different types of disorder in the form of random distributions of particle positions, bead diameter, elastic modulus and density of the beads are possible, which could give rise to inhomogeneous terms added to an otherwise homogeneous wave equation. Inhomogeneities of a larger length scale are known as the force-chains, linear but branched structures consisting of the force-carrying contacts between beads that are established under applied stress[21, 22, 23], which are thought to provide preferred paths for sound propagation, as implied by stress-optical experiments [24]. Studies on the influence of disorder on sound propagation were already conducted in two-dimensional systems, where the force-chains were directly observable with stress-optical methods [25, 26], however, only the coherent signal was measured. Measurements of multiply scattered waves in packings of such stress-birefringent particles tend to be severely obstructed by absorption from viscoelastic damping in the particle material[24] (as I have also found in various experimental attempts). For large three-dimensional packings the force-chains are not yet directly resolvable in experiments, although some initial developments have been made [27]. Three-dimensional packings have been studied in simulations [28] where the effect of disorder on dispersion and attenuation, resulting in the packing acting as a low-pass filter, was shown. In experiments, the microscopic configuration of a packing is not known, thus one must rely on the sound measurements to extract the moments or correlation functions of the random distribution that leads to the multiply scattered wave. In appendix E.2 the dependence of the scattering mean free path ℓ_s on ℓ_c is illustrated by explicit calculation for the simplest examples. The correlation length can then be compared to the micro- and mesoscopic length-scales of the packing such as bead diameter and force-chain correlation length.

Measurements of the incoherent intensity of elastic waves in the diffusive limit showed that the transport mean free path $\ell_T \approx d$ is close to the bead diameter[10, 29], implying the correlation length of the elastic medium is much shorter than the correlation length of force-chains. These experiments were conducted in three-dimensional glass bead packings at high confinement pressure $p_0 \propto 100$ kPa at small wavelengths, comparable to the bead diameter, such that $k \cdot d \approx 2.9$, and sufficiently large sample size $L \gg \ell_s$ of many scattering mean free paths, ensuring randomization of the phase and equipartition of energy in all (but predominantly shear) modes. This is in contrast to what could have been expected based on the experiments with monolayers of stress-birefringent particles that showed sound propagation predominantly along the force-chains[24]. The question arises how general this result is, or if and how the correlation length of the elastic medium and the transport and scattering mean free paths depend on experimentally accessible properties of the packing (or ensembles of macroscopically equivalent packing configurations). For example, it is known that the correlation length of the force chains increases when the packing is sheared or put under anisotropic load[30], suggesting a similar increase in the correlation length of the elastic medium, which could be probed by sound measurements. Another interesting case arises for packings at low confinement pressure. Simulations show diverging correlation lengths when the unjamming transition is approached[31, 32]. In this chapter, measurements of the transport mean free path (section 3.3) and the scattering mean free path (section 3.4) at low confinement pressure $\propto 1$ kPa are shown.

As mentioned above, the incoherent signal is sensitive to microscopic changes in the packing configuration and conversely thus may be used to experimentally probe reversible and irreversible rearrangements. Strong excitation may lead compaction of the packing and elastic strengthening, or to buckling, slipping and loosening of the bead packing resulting in elastic weakening[33], affecting the coordination number Z. While the latter is not directly accessible in experiments, it influences the sound speed according to EMT as $c \propto Z^{1/3}$, which is extracted from measurement of the coherent signal. The incoherent signal provides evidence of the rearrangements in the from a drop of a resemblance function

according to Eq. (3.1) measuring the similarity of successively measured signals[33]. In appendix A such an analysis is shown for the sound measurements in microgravity from chapter 2, but the incoherent signal was not strong enough to provide meaningful results, except when the packing configuration was intentionally changed by repeating the packing preparation.

$$\Gamma_{i,i+1}(\tau) = \frac{C_{i,i+1}(\tau)}{\sqrt{C_{i,i}(0) \cdot C_{i+1,i+1}(0)}} \text{ with } C_{i,j}(\tau) = \int x_i(t) \cdot x_j(t+\tau) \mathrm{d}t \tag{3.1}$$

In section 3.5 of this chapter, other methods of potential use for extracting evidence for microscopic rearrangements from sound measurements are tested which rely on extracting the impulse-response relating the excitation signal and the measured sound signal. When the full duration of the signal is taken into account and a large-bandwidth excitation signal is used, the received signal is mostly incoherent and thus affected by multiple-scattering. Using the signal-processing technique of section 2.3.5 in a different experimental setup that allows for higher confinement pressure and less inelastic absorption than the *Grascha 2* apparatus of chapter 2, wave-focussing after inverse-filtering or time-reversal is measured. The peak of the focussed wave drops for repeated measurements under tapping. Experiments of this type, with time reversal mirros[34] consisting of large arrays of transducers, were already conducted in granular matter[35]. Here, a much simpler version, involving one two transducers, is shown to provide similarly robust and sharp focussed peaks.

3.2. Setup Overview

For the multiple-scattering experiments both the apparatus from chapter 2 and a dedicated sample-cell with adjustable fill height were used. Both experimental setups are described here:

3.2.1. Grascha Setup

The GRASCHA apparatus, as described in section 2.3.2 is used with accelerometers embedded within the packing at different distances, 33 and 88 mm from the vibrating wall, but at the same height in the center of the sample-cell, as well as piezos at the wall opposite to the vibrating wall, at 122 mm distance. The accelerometers have cross-sectional areas of 1 cm x 1 cm in contact with the glass beads. The piezos have machined aluminium sonotrodes of 10 and 20 mm diameter cross-sectional area exposed to the granular packing. The large one is mounted at $2/3$ of the sample cell height, the small one at $1/3$. The total length of the sample cell of 122 mm is fixed. The transverse dimensions of 15 cm width and 12 cm height are also fixed in good approximation, apart from small adjustments of the pressure wall position in the range of millimeters.

During the measurements with GRASCHA it became clear that some flexibility regarding the sample cell length is desirable. Also, the almost cubic geometry of the GRASCHA-cell deviates from the boundary conditions assumed in section 3.3 because reflections from the side-walls can not be neglected. Finally, beads smaller than 3 mm in diameter are unsuitable as they can get stuck between moveable parts in the cell, specifically between the pressure wall and the outer cell walls. To overcome these limitations, another setup solely for manual measurements on ground was built.

3.2.2. 3D-printed Sample Cell

The sample cell is shown in Fig. 3.1. It has a cylindrical geometry of 12 cm diameter and similar height. The sidewall is made from 3D-printed photo-resin. The bottom plate is a rigid aluminium plate with circular hole at its center. In the hole, a longitudinal piezo transducer (Olympus VS 103, 15 mm diameter, center frequency 1 MHz) is mounted. It is possible to lead additional wires through this hole to enable usage of additional sensors, such as the bender element shown in Fig. 3.2 (Johnson Matthey)

to enable measurement or excitation of transversal waves. In this case, the bender is mounted on the bottom plate beneath the piezo at the center. It protrudes into the packing by 12 mm and is located off-axis at a radius of 20 mm from the center. The top plate is a circular aluminium plate that loosely fits into the cylindrical cell so it can be used to close the cell at arbitrary fill height. The plate has four holes that permit feeding through cables to sensors mounted on the inside of the plate. Usually another longitudinal piezo (a cheap piezoceramic disk of 25 mm diameter, ca. 2 nF capacitance and fundamental modes at 105 kHz and 1.8 MHz, supplied by Conrad) is mounted at the center of the plate. Additionally or alternatively, another bender element is mounted on the plate. Additionally, accelerometers (*Brüel&Kjær* 4508-B) can be placed within the packing as shown in Fig. 3.9.

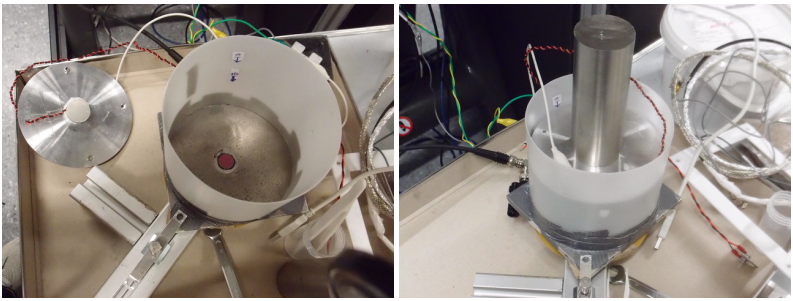

Figure 3.1.: Left: *Overview of 3D-printed cylindrical sample cell containing a longitudinal piezo (Olympus VS 103) mounted at the bottom plate as well as another piezo mounted on the inside of the removable top plate. Both bottom and top plates are grounded. The bottom plate is rigidly mounted on a heavy aluminium structure that is also grounded.* Right: *Filled and closed sample cell with steel weight on top for providing adjustable confinement pressure.*

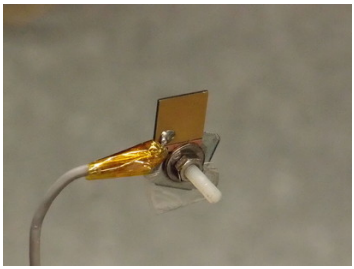

Figure 3.2.: *Bender Element with wires.*

Apart from the sensors, the measurement chain consists of a USB oscilloscope (*Picoscope* 5442B series), CCLD preamplifier (*Brüel&Kjær* 1704-A-002) and a power amplifier (Cosinus HSA 4011, 0 - 1 MHz, 1 A_{rms}, 150 V_{p-p}) as shown in Fig. 3.3. The oscilloscope contains an arbitrary signal generator (AWG) that provides any desired excitation signal. The signal from the AWG is amplified by the power amplifier by up to a factor of 100 in voltage in order to drive any of the piezos. As the piezos have large impedance in the range of 10 kΩ - 1 MΩ in the relevant frequency range of 1 - 100 kHz in my experiments, the current consumption is much lower than what the amplifier can provide. For piezos used as receiver, the piezo impedance is much closer to, but still lower than the input impedance of

the oscilloscope. Therefore, in principle one can connect them directly to the oscilloscope, as they approximately act as a voltage source. However, it has proven beneficial to use the preamplifier which provides an adjustable voltage gain (1, 10 or 100). Then the oscilloscope records the amplified received signal in up to 4 channels at adjustable resolution and sample rate. Usually 14 bit and 65536 samples for 200 ms of recording time is chosen which is well suited for the 10 - 50 kHz signals measured in these experiments here. The grounds of oscilloscope, preamplifier and power-amplifier output are connected. This ground is also connected to the bottom and top plate of the sample cell as well as to the aluminium structure on which the cell is mounted.

Figure 3.3.: Left: *Power amplifier (Cosinus HSA 4011) to drive the piezos.* Right: *USB oscilloscope (Picoscope 5442B) and CCLD preamplifier (Brüel&Kjær 1704-A-002) for piezos and accelerometers. Also a small, convenient keyboard was used next to the experimental setup.*

3.3. Incoherent Intensity Profile

In this section the transport mean free path ℓ_T for elastic waves in glass bead packings is determined from the incoherent intensity profile ofdiffusively scattered waves. Compared to previous measurements in the literature [9, 10, 11] which were conducted at confinement pressure of $p_0 \propto 100 - 1000$ kPa, here $p_0 \propto 1$ kPa is used, potentially rendering the results sensitive to effects of unjamming such as to an increase of the correlation length ℓ_c of the elastic medium[31, 32] and a resulting increase in ℓ_T.

We use the diffusion model (1.128) from section 1.3.4. In the experiments with the cylindrical sample cell the length $38 < L < 74$ mm is always much smaller than the diameter 120 mm whereas the emitter and receiver are mounted on or close to the symmetry axis of the cell, far away from the sidewall. Thus we can use the approximation of wave propagation through a slab of infinite transversal extent. The longitudinal central axis of the cylinder is denoted z, while x and y correspond to the transversal axes. If a point source at $z = x = y = 0$ emits a pulsed wave at time $t = 0$ into a medium of infinite transversal dimensions and longitudinal size L, the time-dependent intensity of diffusely scattered waves along the z-axis is given by: [36, 37]

$$I(t) = -D\,\frac{\partial U}{\partial z}\bigg|_{z=L} = \frac{\mathrm{e}^{-r^2/(4Dt)}\mathrm{e}^{-t/\tau_a}}{2\pi L^2 t}\sum_{n=1}^{\infty} A_n \mathrm{e}^{-D\beta_n^2 t/L^2} \tag{3.2}$$

Here $r = \sqrt{x^2+y^2}$ and $D = \frac{1}{3} v_T \ell_T$ is the diffusion coefficient. We also have to include the inelastic absorption time $\tau_a = Q/(2\pi f)$. The extrapolation length z_0 is well approximated by ℓ_T for diffusive scattering in the slab geometry[38]. The coefficients A_n that arise from the boundary conditions are[37]:

$$A_n = \frac{\beta_n \left(\beta_n K \sin\left(\beta_n z/L\right) - \cos\left(\beta_n z/L\right)\right)\left(\sin\left(\beta_n z_0/L\right) + \beta_n K \cos\left(\beta_n z_0/L\right)\right)}{1 + 2K + \beta_n^2 K^2} \tag{3.3}$$

Here the β_n satisfy the transcendental equation

$$\tan(\beta_n) = \frac{2\beta_n K}{\beta_n^2 K^2 - 1} \tag{3.4}$$

where K depends on the reflection coefficient R of the top and bottom boundaries:

$$K = \frac{2\ell_T}{L}\frac{1+R}{1-R} \tag{3.5}$$

R is determined by the acoustic impedance mismatch of the top/bottom plates and the granular medium as well as the angle of incidence. The aluminium plates have a density of $2700 kg/m^3$ and a sound speed of $6400 m/s$ (longitudinal)[39], therefore the impedance is $Z_{Al} = c \cdot \rho = 17 \cdot 10^6$ Rayl. In the granular medium, as prepared in these experiments here, longitudinal sound speeds around $350 m/s$ were measured. Here packings of $d = 4mm$ glass spheres of volume fractions $\phi \approx 0.66$ were prepared. The glass density, as measured for the spheres used here, is $2519 kg/m^3$. Then the granular acoustic impedance is $Z_G \approx 0.58 \cdot 10^6$ Rayl. Thus we can estimate the reflectivity at normal incidence as:

$$R = \left|\frac{Z_{Al} - Z_G}{Z_{Al} + Z_G}\right|^2 \approx 0.87 \tag{3.6}$$

For a nonzero angle of incidence R will be even larger. For multiply scattered waves the angle of incidence will be randomly distributed. Thus the average reflectivity will be close to 1, which we now insert in (3.5) thus taking the limit $K \to \infty$. Then (3.4) is solved by $\beta_0 = 0$, $\beta_1 \to 0$ and $\beta_n \to n\pi$ for $n > 1$. Then the resulting intensity is:

$$I(z,t) = \frac{\mathrm{e}^{-r^2/(4Dt)}\mathrm{e}^{-t/\tau_a}}{2\pi L^2 t} \sum_{n=1}^{\infty} \cos(n\pi z_0/L)\sin(n\pi z/L)\mathrm{e}^{-Dt(n\pi/L)^2} \tag{3.7}$$

After convolution with the applied excitation signal intensity, this expression can be fitted to the measured incoherent intensity at a detector at position $z = L$ as used in the cylindrical sample cell. In case of similar measurements using the GRASCHA apparatus we have to use slightly different boundary conditions. First of all, the emitter covers the entire cross-sectional area of the cell, resulting in plane-wave excitation. Therefore we have to integrate (3.7) over the x-y-plane. Second of all, for measurements with the accelerometers embedded into the packing, we have to insert their known positions at $z = 33mm$ or $z = 88mm$. The resulting intensity is given by:

$$I(z,t) = \frac{v_e U_0}{2L} e^{-t/\tau_a} \sum_{n=0}^{\infty} \frac{1}{\delta_n} cos\left(\frac{n\pi z}{L}\right) cos\left(\frac{n\pi \ell_T}{L}\right) e^{-tD(n\pi/L)^2} \tag{3.8}$$

Again, the a convolution with the excitation pulse is applied (numerically) before fitting.

3.3.1. Measurement Procedure with Grascha

The cell was filled with glass beads and closed. Then alternating high and low pressure settings were applied and several sound measurements taken using the command-line interface in order to find the most suitable measurement parameters. Depending on the amount of granular material in the cell different minimum and maximum pressures were found attainable, thus the pressure settings for the actual measurement campaign had to be adjusted accordingly. For the oscilloscope and signal generator similar fine tuning was done whenever a new signal type was used. For example, as the frequency was increased, the attenuation in the granular medium as well as the limited bandwidth of the voice-coil became more apparent and needed to be compensated by adjusting the preamplifier gain and oscilloscope ranges as well as the signal generator output voltage. Another concern was the pulse duration. As the received intensity profile is the convolution of (3.8) with the pulse intensity, the pulse duration had to be kept as short as reasonably possible while still providing a well-defined center frequency. Here, not only the desired excitation signal has to be taken into account, but also the response of the voice-coil and its driving electronics. A systematic way to suppress any artifacts from this response such as extended ringing due to its fundamental frequency of 20 kHz was the method of inverse filtering as described in section 2.3.5. Attempts to fine-tune the parameters for inverse filtering often took several hours of heuristic work. Oftentimes the inverse filtering was omitted as the "raw" signal was deemed good enough.

Once the measurement parameters were fixed, they were used in a fully automated campaign which was defined in few configuration files. In each campaign the pressure was readjusted to alternate between a low setting, typically at 500 Pa, and a high setting, typically at 900 Pa. These values correspond to normal forces acting on sensors in a side wall. It must be noted that in control measurements with different orientation of the sample cell a highly anisotropic force distribution was found with vertical forces about twice as high as horizontal forces. Also a Janssen effect[40, 41] was found, reducing the effective weight on the bottom of the cell by about 27%.

To prepare the packing for sound measurements the protocol described in section 2.3.3 was applied twice to ensure a stable packing. Then a series of measurements of identical tone-burst pulses was performed. Usually 16 repetitions were recorded to provide a means of averaging out noise artifacts from the electronics or random mechanical vibrations. Any incoherent signal resulting from such artifacts would be averaged out, while the random but deterministic scattering signal for one given packing configuration would remain. Then an effectively new packing was prepared by changing the pressure setting by applying the preparation protocol, again, twice. By alternating between high and low pressures it was attempted to change the packing configuration as violently as possible without the need of manual intervention involving opening and refilling the sample cell. 64 configurations per pressure setting were prepared, or 128 in total. Such a campaign lasted typically one hour. Afterwards the settings could be changed or the sample cell could be refilled in preparation of a new campaign. Usually two or three campaigns were run per day where different particle sizes were used, including monodisperse 3, 4 and 10 mm spheres and bidisperse mixtures. Signal types were 3 - 5 cycle Gaussian tone-bursts of 4 - 30 kHz center frequency.

An alternative measurement protocol consisted of a series of 20 or 40 tone-bursts of increasing center frequency from 2 to 11 kHz or from 10 to 29 kHz separated by 5 ms intervals between bursts. The series was implemented as a single waveform that was sent to the signal generator. Such a series was measured 16 times for each configuration. Again, 64 configurations were prepared per pressure setting or 128 in total. The advantage was that here many frequencies were measured in one campaign within one hour instead of 20 or 40. The disadvantage is that the oscilloscope and other device settings had to be a compromise suitable for the entire frequency range. Also, in hindsight, the interval between pulses should have been extended to at least 10 ms if not 20 ms to avoid any residual vibrations in any interval resulting from excitation during the previous interval. For such increased interval lengths it would be necessary to split the series into several waveforms as the signal generator resolution is limited. But even with the 5 ms interval the main part of each signal was still mostly cleanly measured

with low frequency ringing present mostly after the low frequency excitation signals.

The data analysis was performed mainly with the tool QUICK described in the appendixC. Additionally, an averaging tool was written. The overall analysis was organized in a Makefile, where the targets correspond to the various stages of the analysis. The dependency handling via Makefile provided a great amount of automation without which any meaningful analysis would be practically impossible. The individual stages were implemented in shell-scripts. First, preprocessing of the recorded waveforms was necessary i.e. conversion from the GRASCHA 2 oscilloscope file-format to the generic QUICK file-format, DC-removal, resampling or downsampling and bandpass-filtering and/or white-noise removal via Gaussian smoothing. Then averaging over all waveforms for each configuration was performed to get rid of electronic or other noise that could otherwise be mistaken for an incoherent signal. Then the average waveform over all configurations was calculated. This average signal which represents the coherent wave was then subtracted from each configuration-specific waveform. Then the intensity was calculated for each subtracted waveform. Finally, the average over all these intensities was calculated. The analysis includes all four oscilloscope channels, usually corresponding to two accelerometers and two piezos.

It shall be noted that in early versions of the experiment the trigger point of the oscilloscope was unreliable, especially when the protocol with a series of many bursts in each waveform was used. In an attempt to correct the resulting time offsets between waveforms the following method was implemented: the first waveform was picked as a reference to which the time-shift of each of the remaining waveforms was estimated. This was done by finding the highest peak of the cross-correlation using the full duration of the waveforms. Each waveform was then time-shifted back accordingly. Then a 2 - 50 kHz bandpass filter was applied to remove any noise outside the relevant bandwidth of the measurement. Then a small region-of-interest containing only the first few oscillation cycles of one burst was selected as only the beginning of the signal can be meaningfully compared between different configurations. Within this region-of-interest the cross-correlation was calculated to get an estimate for the remaining time-shift according to which each waveform was then shifted back. While this procedure worked in general, the precise result was found to depend on the parameters for preprocessing such as filter frequencies, Gaussian kernel width and the selection of the region-of-interest for the cross-correlation. A visual comparison of random selections of waveforms often showed remaining time-shifts of several waveforms. It was concluded that no unambiguous way of finding the correct preprocessing parameters for removing all time-shifts can be found, rather all measurements had to be redone. Eventually better trigger settings were found such that the excitation signal from the AWG as detected in the external trigger channel could be used. The result was a reliable trigger point with μs accuracy i.e. practically no time-shift within the accuracy of these measurements presented here.

3.3.2. Measurement Procedure with 3D-printed Cell

The cell was filled with glass beads and closed. From the fill height and the total weight of the glass beads the volume fraction was obtained. In this initial state no transmission of high frequency sound in the range of several 10 kHz was possible, even after adding a steel weight on the top plate to add confinement pressure. To prepare a packing for sound measurements manual force was exerted on the top plate for 5 seconds in addition to the force from the steel weight. This resulted in a packing of much higher transmission of low frequency waves of few kHz but rapidly repeated sound measurements showed strong fluctuations between successive measurements. At this point tapping was applied to the packing by repeatedly knocking on the aluminium structure. As a result, the received sound signals began to look increasingly similar, including the high frequency part. Finally, a series of high frequency pulses, as used for the proper measurement, was transmitted until the received signals looked identical, which was used as criterion for a stable packing. This was often reached after 30 pulses but sometimes not even after 60, in which case a completely new packing was prepared.

The excitation signals were usually 1 - 3 cycle bursts of 20 - 60 kHz center frequency. Then the received signals at the longitudinal piezo showed a leading low frequency pulse followed by a high

frequency signal. The leading pulse amplitude was found roughly proportional to the squared excitation amplitude, suggesting it results from nonlinear demodulation. As it was always the earliest arriving part of the signal it can be assumed the demodulated pulse is a P-wave, independent of whether a bender or longitudinal piezo was used for excitation. Given the assumption that this demodulated wave was emitted within few layers of beads close to the emitting piezo or bender, as demodulation from layers far away from the emitter carry random phases and thus are expected to interfere destructively, it can be assumed to have travelled the linear distance between emitter and receiver. Then its time of arrival can be used to determine the longitudinal speed of sound in the packing. This time of arrival was used as criterion for 'equivalently' prepared packings, as all macroscopic properties (ϕ, p_0, c_p and thus Z) were the same for all packings prepared this way.

The time of arrival of the high frequency part of the received signal at the bender element was used to determine the S-wave speed of sound. This measurement was highly inaccurate compared to the measurement of the demodulated wave as the high frequency signal was much more spread out in time with no clear leading edge. Comparison of the received signal with the time-shifted 3-cycle excitation signal shows it is roughly consistent with $c_s \approx \frac{1}{\sqrt{3}} c_p$ in all cases. Therefore it is assumed that the measurement using the bender element is mostly sensitive to S-waves.

For each packing a series of 32 identical tone-burst measurements was conducted. Then a new packing was prepared by opening the sample cell, manually stirring the beads in the cell, closing it and repeating the above mentioned procedure. For each type of packing characterized by fill height, confinement pressure and bead diameter 16 configurations were prepared and measured which took about one hour.

3.3.3. Results from Grascha

The measurements shown here were taken at a pressure setting that resulted in 200 Pa at the uppermost sensor and 1200 Pa at the lowest sensor in the sidewall.

In Fig. 3.4 a typical raw signal is shown, along with the square-root of the average incoherent intensity, in this case after excitation with a 12 kHz tone-burst. In Fig. 3.5 the intensity profiles for both accelerometers along with the diffusion fit according to Eq. (3.8) using the known accelerometer positions is shown. The absorption is very high with $Q \approx 30$, limiting the signal duration to 3 - 4 ms, at which point the signal becomes comparable to the noise. The diffusion coefficient D is fitted to 0.77 m^2/s. To get an estimate of the transport mean free path ℓ_T, first the transport velocity v_T is needed, which is estimated by the shear wave speed, as is appropriate in the diffusion limit. However, in these measurements only the longitudinal sound speed is obtained from the ballistic signal. Here we estimate $c_s \approx c_p/\sqrt{3}$, according to the approximate ratio found at similar pressure with the same glass beads in the cylindrical sample-cell, and get 144 m/s. Then, $\ell_T \approx 3D/v_T \approx 5d$ is found. Similar results are found for other center-frquencies.

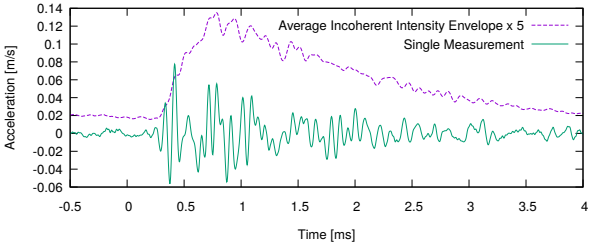

Figure 3.4.: *Raw signal of transmitted tone-burst (green) and square-root of averaged incoherent intensity of 64 configurations is shown here.* Taken from [42].

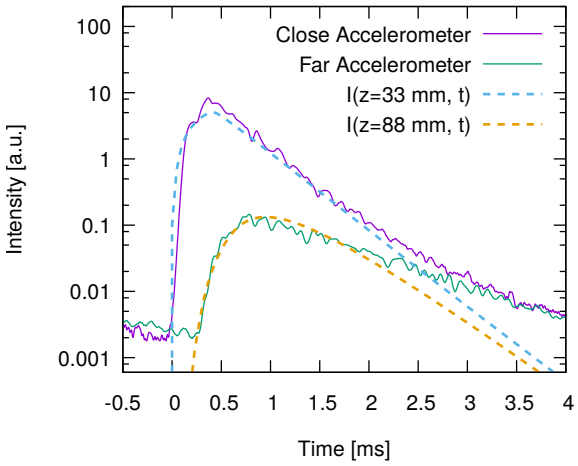

Figure 3.5.: *Incoherent intensity after 4 cycle tone-burst at 12 kHz measured on ground with* GRASCHA. *The intensity was averaged over 64 configurations after subtraction of the average signal. Results from the close (violet) and far (green) accelerometer within the packing are shown as well as the fit to the diffusion model (3.8) with z = the position of each accelerometer. The fit gives $D = 0.77\ m^2/s$ and $Q = 30$.* Taken from [42].

3.3.4. Results from 3D-printed Cell

First, it should be noted that the pressure in these experiments is higher and more well-defined than in the GRASCHA setup. Due to the steel weight on top, the minimum pressure is limited to 1.4 kPa. The maximum pressure, as estimated from the mass of the glass bead packing and the weight, is between 2.0 and 2.7 kPa. From this estimate, an unknown fraction has to be subtracted due to the Janssen effect, but as the beads are the same as in the GRASCHA experiments, where the Janssen effect contributed $\approx 27\%$, it can be assumed to be a similar but likely smaller contribution, since the cylindrical sample-cell has a larger aspect-ratio. As expected based on this higher pressure, a larger sound speed is determined from the ballistic signals around ≈ 350 m/s for all fill heights.

In Fig. 3.6 the average incoherent intensity is shown together with the fitted diffusion profile for two different sets of measurements in terms of fill height and center-frequency. For a summary of different fill heights, the intensity profiles for 38 - 75 mm are shown in Fig. 3.7. In all cases, the transport mean free path is found between 1.55 and 1.8 particle diameters and the quality factor is between 65 and 80.

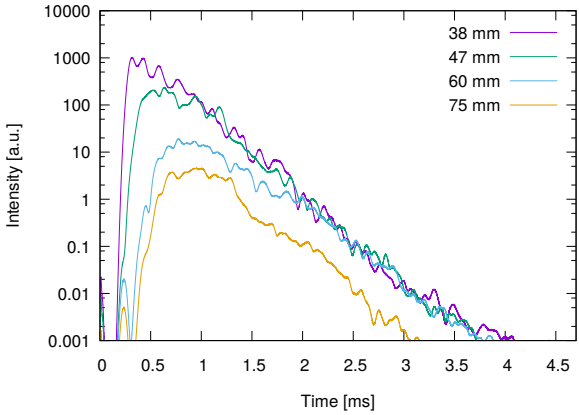

Figure 3.7.: *Incoherent Intensity for different sample thicknesses from 38 to 75 mm. For each thickness results for the average intensity of 16 configurations after subtraction of the average signal are shown for measurements using the bender element. As the thickness increases, the intensity peak broadens and shifts to later times but the diffusion coefficient stays almost constant. The transport mean free path ℓ_T is found within 1.55 - 1.80 particle diameters and Q is fitted to 65 - 80.*

3.3.5. Discussion

The results for ℓ_T from various sample thicknesses and frequencies as measured in the printed cell are all very similar. The GRASCHA-Result shows more absorption and 2.5 times larger ℓ_T. In all cases Q is much lower than literature values measured at several 100 times larger pressure[10, 29] and ℓ_T is almost twice as large in the printed cell and five times as large in the GRASCHA setup than in [10, 29], where $\ell_T \approx d$. This large transport mean free path could be the result of anisotropy from the hydrostatic gradient, leading to a large correlation length similar to what was found in two-dimensional packings of stress-birefringent particles [30]. While the hydrostatic gradient is negligible at the large pressures used in [10, 29], it leads to a large pressure difference in the experiments shown here, most significantly in the GRASCHA cell due to the lack of a weight on top. The low pressure itself could also be responsible, as the packing is closer to the jamming point than in the high pressure experiments reported in the literature, which is thought to be related to an increase in the correlation length[31, 32]. Those two proposed sources for large correlation lengths can not be distinguished here.

3.4. Coherent Attenuation

Due to multiple scattering at random disorder, the ensemble-averaged Green's function (1.72) contains a self-energy term which leads to dispersion and attenuation. Under the assumption that the coherent signal is attenuated mainly by scattering instead of inelastic absorption, its attenuation length can

be used to estimate the scattering mean free path ℓ_s. For this purpose, frequency-dependent sound transmission is measured here in glass bead packings within the cylindrical sample-cell.

3.4.1. Procedure

To get an estimate of the effective transfer function in the far field, measurements at two large sample thicknesses, 47 and 70 mm, were conducted that were chosen such that for the largest thickness it was still possible to receive a high frequency signal that could be distinguished from noise. For each thickness 16 packings were prepared with the procedure as in section 3.3.2. The excitation signal for the sound measurements was an exponential chirp ranging from 5 - 80 kHz, covering more than the entire passband. According to the power density spectrum of the received signals, a cutoff frequency at about 50 kHz was found for all packings. For each configuration 32 waveforms were recorded. As always, the analysis was conducted with QUICK.

To probe the coherent wave only, the analysis conducted here uses only the average of all waveforms for a given thickness. After averaging, two different methods of extracting the transfer function were used. In the first method, for each sample thickness $L_1 = 47$ mm and $L_2 = 75$ mm the impulse response $h_L(t)$ satisfying $y_L(t) = (x * h)(t)$ for the known excitation signal $x(t)$ and the measured coherent signal $y_L(t)$ was calculated numerically by and FFT-based inverse convolution. Then, for both $h_{L_1}(t)$ and $h_{L_2}(t)$, a region of interest of few milliseconds starting at $t = 0$ was selected to remove potential artifacts from anti-causal contributions or reflected waves. Then the ratio of intensities at L_1 and L_2 was calculated as the power-density of the impulse response $h(t)$ defined by $y_{L_2}(t) = (y_{L_1} * h)(t)$, where $h(t)$ was calculated by inverse convolution of $h_{L_2}(t)$ with $h_{L_1}(t)$. Written in the Fourier domain this is equivalent to:

$$H(\omega) = \frac{I_{L_2}(\omega)}{I_{L_1}} = \frac{H_{L_2}(\omega)}{H_{L_1}(\omega)} = \left(\frac{Y_{L_2}(\omega)}{X(\omega)}\right) / \left(\frac{Y_{L_1}(\omega)}{X(\omega)}\right) \tag{3.9}$$

Then, using Lamber-Beer's law, the scattering mean free path is given by:

$$\ell_s = -\frac{L_2 - L_1}{\log(|H(\omega)|^2} \tag{3.10}$$

In second method, the analysis was done in the time domain. The measured coherent signals were decomposed into 1024 sine and cosine components at frequencies up to 80 kHz as $s(\omega) = \int_t^{t+T} y(t+t') \cdot \sin(\omega t')\mathrm{d}t' / \int_0^T \sin(\omega t')\mathrm{d}t'$ and analogously for the cosine. Here, the signal was divided into periods of duration T containing a full sine/cosine period of angular frequency ω, then the average over all periods was taken for the final result. At each frequency the signal amplitude was determined from the sine and cosine components. The scattering mean free path was then obtained as in Eq. (3.10) but from the amplitude ratio substituted for $H(\omega)$.

3.4.2. Result from 3D-printed Cell

In Fig. 3.8 the scattering mean free path is shown, as obtained from the chirp measurements in the 3D-printed cell. The results from both methods agree well with each other, despite each being sensitive to different types of artifacts. In the frequency range up to 50 kHz, where clear sound signals were still received, ℓ_s is found between one and two particle diameters.

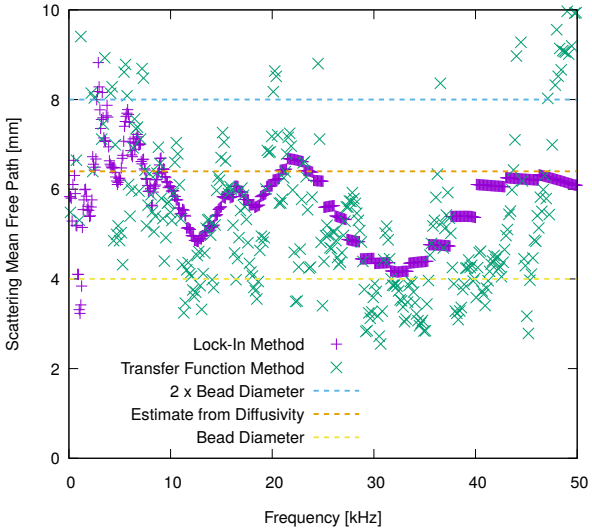

Figure 3.8.: *Scattering mean free path obtained from attenuation of coherent wave. The excitation signal was a 5 - 80 kHz exponential chirp. At ca. 50 kHz the cutoff frequency limits the accessible measurement range. Results from lock-in method (violet crosses) and transfer function method (green crosses) after averaging over 16 configurations are shown in comparison with the result from incoherent scattering measurements(center dashed line) from section 3.3.4. For reference, the bead diameter d and $2 \cdot d$ is also shown (top and bottom dashed lines).*

3.4.3. Discussion

The obtained scattering mean free path $d < \ell_s < 2d$ is similar to the transport mean free path $1.55d < \ell_T \approx< 1.80d$ obtained from the incoherent intensity in the previous section, suggesting they can be identified with each-other. Although inelastic absorption was found to severely limit the duration of the incoherent signal in the previous section, with $\tau_a \approx 0.2$ ms, the time-of-flight between 47 and 75 mm is even smaller at the longitudinal ballistic wavefront speed 380 m/s, making it plausible that scattering still dominates the attenuation in this measurement. The result is consistent with the treatment of multiple scattering in section 1.3.4.

3.5. Wave Focussing and Time Reversal

3.5.1. Introduction

If one tries to focus a travelling wave of center frequency $\omega = 2\pi c/\lambda$ on a point at distance L from the source then due to diffraction the focal spot is limited to a minimum width $\approx \lambda L/a$ where a is the aperture of the source. In a inhomogeneous medium multiple scattering leads to an increased resolution i.e. it gives rise to an effective aperture $a_e > a$ [43]. Experiments with time reversal mirrors[35] consisting of arrays of transducers that measure the elastic wave resulting from excitation with a point-like source, electronically i.e. numerically reverse the recorded signals in time and transmit it back,

found a finer focal spot of the refocussed wave when the full signal, including the long-duration coda, was used. It was demonstrated, that for a given granular packing configuration, the focussed signal was reproducible until deviations were found when the amplitude was increased such that microscopic rearrangements in the packing were triggered. The measurement of such focussed waves thus appears to be a promising diagnotic method to probe the time-evolution of granular matter under excitation. In this section, simple versions of similar wave focussing techniques based on only a pair of transducers are tested.

3.5.2. Setup Overview

As in the previous measurements using the 3D-printed sample cell, usually one longitudinal piezo or bender was used as emitter, while one piezo or bender was used as receiver. Both were mounted on the central axis of the cell on the top and bottom plate, facing each other directly.

As can be seen in Fig. 3.9 sometimes accelerometers were used as receivers as alternative to the otherwise used configuration with a longitudinal piezo and a bender element at the bottom of the sample-cell. The accelerometers were placed in the packing within close proximity to check if after inverse filtering a focussed signal could be obtained at one but not the neighboring sensor. This indeed worked even for the smallest obtainable sensor-sensor distance (ca. one bead in between).

All signal processing, as described in section 2.3.5, was done with the tool QUICK which is descibed in appendix C.

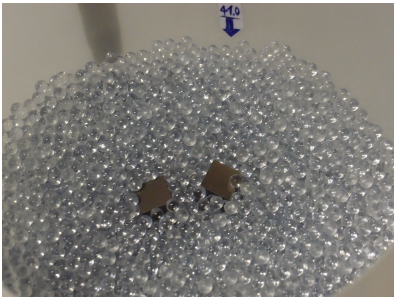

Figure 3.9.: *Accelerometers (Brüel&Kjær 4508-B) placed in glass bead packing within close proximity to each-other. In the experiments even closer proximity was used while still being able to focus the signal at one of the two sensors.*

3.5.3. Focussing in Air and in Granular Matter

The measurement took place in two steps. First, a probe signal was recorded from which the impulse response, relating the received sound signal to the excitation signal, was determined according to Eq. (2.12). Then the original excitation signal, a short sinusoidal burst, was inversely convolved with this impulse response and the result, a signal of much longer duration and of irregular structure in time, was transmitted. It was found to be feasible and convenient to combine the two calculations into one step, as is implemented in QUCK.

In Fig. 3.10 the probe signal is shown for two packing configurations illustrating the effect of tapping.

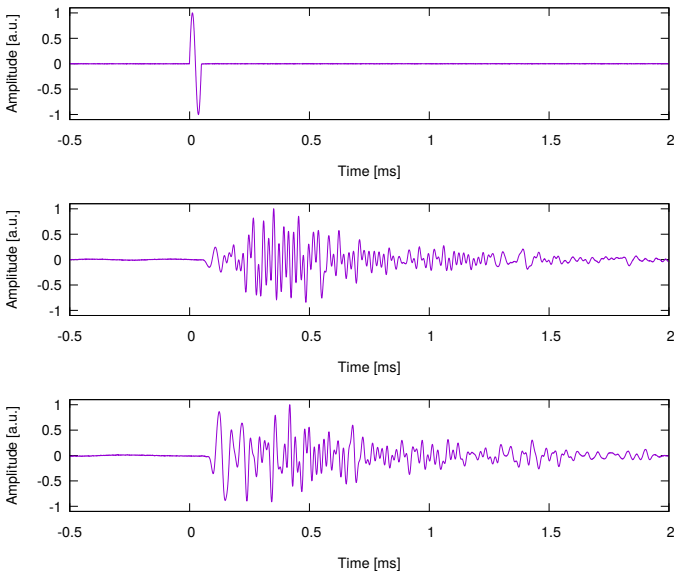

Figure 3.10.: *Probe Signal. Top: Excitation signal. Center and bottom: received signal after propagation through glass bead packing shown for two different configurations. The exact shape of the highly fluctuating signal is configuration dependent as it changes after tapping.*

A comparison of wave focussing in air and in granular matter is immediately feasible as both air and the packings of 4 mm glass beads at ≈ 2 kPa exhibit nearly the same longitudinal speed of sound around ≈ 330 and ≈ 380 m/s. In both cases, a single cycle sine at 20 kHz was used as probe signal. In Fig. 3.11 the resulting focussed signal after propagation in air vs. granular matter is shown.

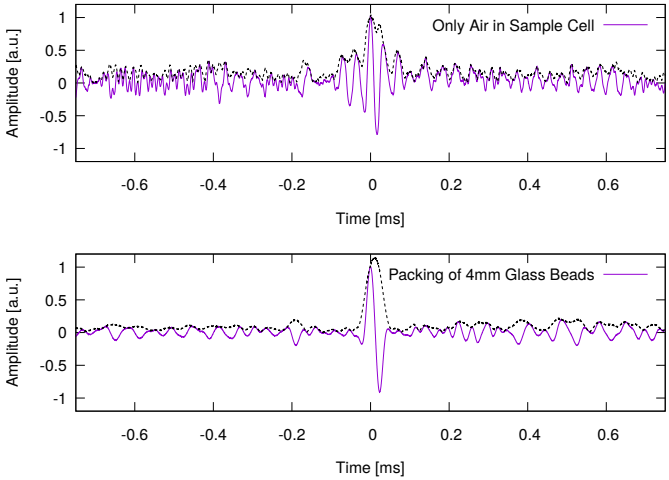

Figure 3.11.: *Received signal at accelerometer within the sample cell after inverse filtering of excitation signal. Results are shown for the empty i.e. air-filled sample cell (top) and the full cell containing a packing of glass beads of diameter 4 mm (top). In both cases, the same probe signal was used. Direct comparison of the focussed signal shows increased temporal resolution and higher contrast for the result in granular matter compared to air.*

3.5.4. Evolution under Tapping

In Fig. 3.12 the resulting focussed signal after wave propagation through the glass bead packing is shown for repeated measurements during tapping. After many tapping hits (or one very violent hit) the focussed pulse is lost. To regain it, a new probe signal must be measured and the inverse filtering must be repeated.

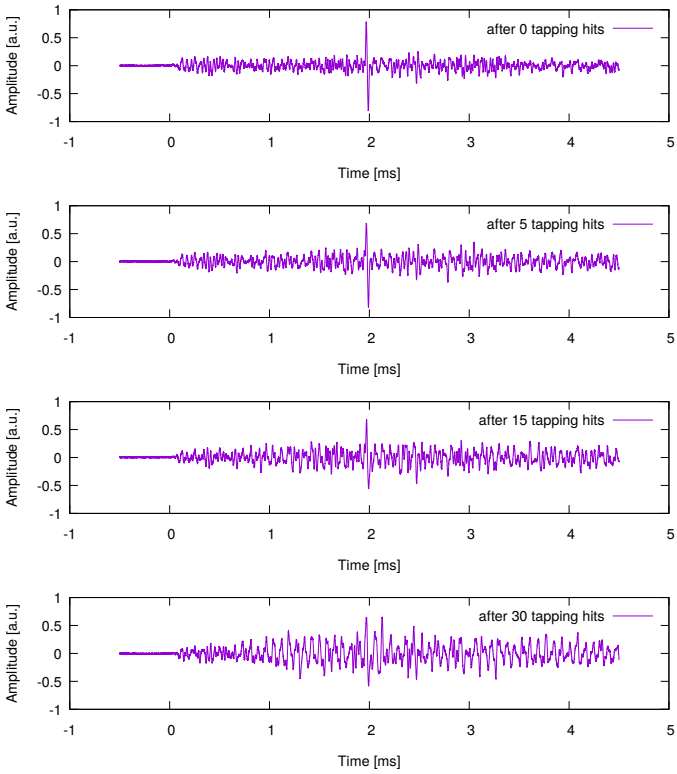

Figure 3.12.: *Received signal at accelerometer within granular packing after repeated tapping. For the same inverse filtered excitation signal the focussed signal gets progressively weaker compared to the fluctuating background and is eventually lost. Similarly, a single violent tapping hit leads to loss of focus (not shown here).*

3.5.5. Time Reversal

In the first step of the measurement a short probe signal, specifically a single cycle 30 kHz sine, was transmitted by the first transducer. The received signal at the second transducer was time-reversed and filtered to remove noise from electrical interference and transmitted back from the second transducer. The first transducer, this time acting as receiver, recorded a focussed signal resembling the time-reversed original probe signal, as shown in Fig. 3.13. Similar to the focussed pulse after inverse filtering shown in Fig. 3.12 it was also found to get progressively weaker under repeated or strong tapping and can then only be restored after measuring a new probe signal.

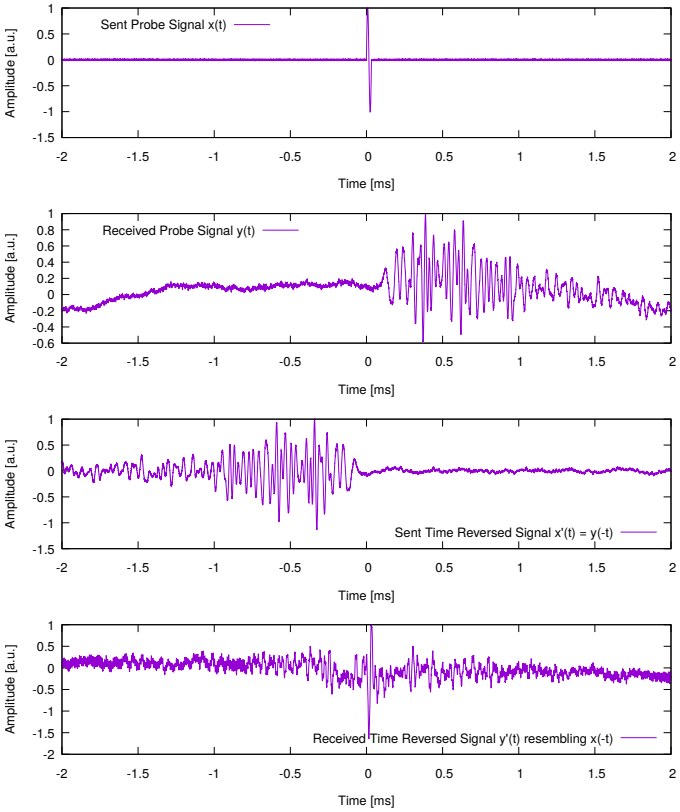

Figure 3.13.: *Time reversal experiment. From top to bottom: original excitation signal, received probe signal, numerically calculated time-reversed probe signal, received signal after exchanging emitter and receiver using the time-reversed probe signal as new excitation signal. The received signal after propagation through the disordered glass bead packing (bottom) closely resembles the time-reversed original excitation signal. It is highly symmetric around $t = 0$.*

3.5.6. Discussion

The direct comparison of temporal resolution for the focussed pulse after inverse filtering of the excitation signal shows a smaller focal width by a factor of ca. 3. This is consistent with an increase of the effective aperture due to multiple scattering in granular matter. The focussed signals are found sensitive to external perturbations such as tapping, but more detailed studies of the amplitude dependence are necessary.

3.6. Conclusion and Outlook

The transport mean free path ℓ_T was determined from the average incoherent intensity. In the measurments in the cylindrical sample-cell at $p_0 \approx 1.8$ kPa ℓ_T is found between one and two bead diameters. This resuts is in well agreement with the scattering mean free path ℓ_s obtained from the attenuation of the coherent signal in the same experimental setup, suggesting $\ell_T \approx \ell_s$. Measurements of the incoherent intensity with the GRASCHA 2 apparatus, at $p_0 \approx 1$ kPa but at a much larger pressure gradient show ℓ_T close to five bead diameters. In all cases ℓ_T is considerable larger than reported previously[10, 29] which could be explained by either stress anisotropy, leading to a large correlation length ℓ_c of the elastic medium[30] or by a similar increase of ℓ_c due to unjamming[**?** 32]. To investigate this further, studies of the force distribution using stress-birefringent particles combined with sound measurements similar to [24] could in principle provide insight. However, with currently available materials the inelastic absorption due to viscoelastic damping severly limits measurements of multiply-scattered waves. For a more accurate analysis of the sound measurements themselves, theoretical treatments need to be developed that include anisotropy and finite correlation lengths. Such a treatment could possibly be based on the Christoffel equation (1.118) which can easily account for the anisotropy. Finally, to unambiguosly distinguish the effects of anisotropy from the effects of jamming, experiments in microgravity should be considered, where arbitrarily low confinement pressure without any hydrostatic gradient can be reached.

The experiments with wave-focussing after numerically applied inverse filtering or time-reversal of the excitation signal demonstrate techniques that can be used to probe microscopic changes in the packing configuration. Further work is necessary to study the width of the focussed peak, which is related to an effective aperture that results from multiple scattering, and the evolution of peak height during repeated mechanical excitation or tapping.

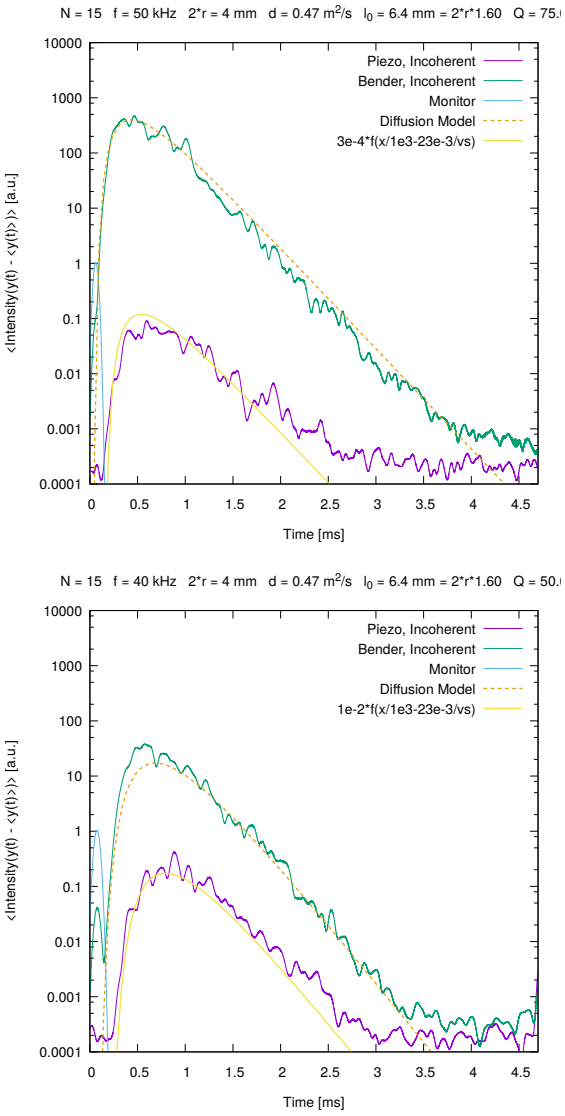

Figure 3.6.: Top: *Incoherent intensity after 3 cycles of excitation at center frequency $f = 50$ kHz after propagation through $L = 50$ mm sample thickness of 4 mm glass beads at confinement pressure 1.6 kPa. The intensity was averaged over 16 configurations after subtraction of the average signal. Results from the bender element (upper, green line) and the piezo (lower, violet line) are shown as well as fits of the diffusion model (3.8) with $z = L$ are shown. The fit gives $D = 0.47\ m^2/s$ and $Q = 75$.* Bottom: *Similar measurement for $f = 40$ kHz and $L = 70$ mm sample thickness resulting in $D = 0.47\ m^2/s$ and $Q = 50$.*

Bibliography

[1] Jacques Duffy and R.D. Mindlin. Stress-strain relation and vibrations of a granular medium. *J. Appl. Mech., ASME*, 24:585–593, 1957.

[2] K. Walton. The effective elastic moduli of a random packing of spheres. *J. Mech. Phys. Solids*, 35(2):213 – 226, 1987.

[3] P. J. Digby. The effective elastic moduli of porous granular rocks. *J. Appl. Mech.*, 48(4):803, 1981.

[4] SN Domenico. Elastic properties of unconsolidated porous sand reservoirs. *Geophysics*, 42(7):1339–1368, 1977.

[5] Joe Goddard. Nonlinear elasticity and pressure-dependent wave speeds in granular media. *Proceedings of The Royal Society A: Mathematical, Physical and Engineering Sciences*, 430:105–131, 07 1990.

[6] Yimin Jiang and Mario Liu. A brief review of "granular elasticity". *The European Physical Journal E*, 22(3):255–260, 2007.

[7] Leonardo Trujillo, Vanessa Torres, Franklin Peniche, and Leonardo Di G Sigalotti. Towards a mathematical model for elastic wave propagation in granular materials. 2012.

[8] Chu-heng Liu and Sidney R. Nagel. Sound in a granular material: Disorder and nonlinearity. *Phys. Rev. B*, 48:15646–15650, Dec 1993.

[9] X. Jia, C. Caroli, and B. Velicky. Ultrasound propagation in externally stressed granular media. *Phys. Rev. Lett.*, 82:1863–1866, Mar 1999.

[10] X. Jia. Codalike multiple scattering of elastic waves in dense granular media. *Phys. Rev. Lett.*, 93:154303, Oct 2004.

[11] V. Tournat and V. E. Gusev. Nonlinear effects for coda-type elastic waves in stressed granular media. *Phys. Rev. E*, 80:011306, Jul 2009.

[12] Anton M Dainty and M Nafi Toksöz. Seismic codas on the earth and the moon: A comparison. *Physics of the Earth and Planetary Interiors*, 26(4):250–260, 1981.

[13] J Christopher Dainty. *Laser speckle and related phenomena*, volume 9. Springer science & business Media, 2013.

[14] Leonardo Trujillo, Franklin Peniche, and Xiaoping Jia. Multiple scattering of elastic waves in granular media: Theory and experiments. In Ruben Pico Vila, editor, *Waves in Fluids and Solids*, chapter 5. IntechOpen, Rijeka, 2011.

[15] Uriel Frisch. Wave propagation in random media. *Institue d'Astrophysique centre national de la recherche, Paris, Academic Press Inc., New York, USA, Card Nr. 68-18657*, 1968.

[16] SM Rytov, Yu A Kravtsov, and VI Tatarski. Principles of statistical radiophysics, vol. 1 springer-verlag, 1987.

[17] Ping Sheng. *Introduction to wave scattering, localization and mesoscopic phenomena*, volume 88. Springer Science & Business Media, 2006.

[18] Leonid Ryzhik, George Papanicolaou, and Joseph B Keller. Transport equations for elastic and other waves in random media. *Wave motion*, 24(4):327–370, 1996.

[19] Nicolas P Tregoures and Bart A Van Tiggelen. Quasi-two-dimensional transfer of elastic waves. *Physical Review E*, 66(3):036601, 2002.

[20] Ibrahim Baydoun, Diego Baresch, Romain Pierrat, and Arnaud Derode. Radiative transfer of acoustic waves in continuous complex media: Beyond the helmholtz equation. *Physical Review E*, 94(5):053005, 2016.

[21] T Travers, M Ammi, D Bideau, A Gervois, JC Messager, and JP Troadec. Uniaxial compression of 2d packings of cylinders. effects of weak disorder. *EPL*, 4(3):329, 1987.

[22] Farhang Radjai, Michel Jean, Jean-Jacques Moreau, and Stéphane Roux. Force distributions in dense two-dimensional granular systems. *Phys. Rev. Lett.*, 77:274–277, Jul 1996.

[23] Heinrich M Jaeger, Sidney R Nagel, and Robert P Behringer. Granular solids, liquids, and gases. *Reviews of modern physics*, 68(4):1259, 1996.

[24] E. T. Owens and K. E. Daniels. Sound propagation and force chains in granular materials. *EPL*, 94(5):54005, may 2011.

[25] Eli T Owens and Karen E Daniels. Acoustic measurement of a granular density of modes. *Soft Matter*, 9(4):1214–1219, 2013.

[26] S Lherminier, R Planet, Gilles Simon, Loıc Vanel, and Osvanny Ramos. Revealing the structure of a granular medium through ballistic sound propagation. *Physical review letters*, 113(9):098001, 2014.

[27] Peidong Yu, Stefan Frank-Richter, Alexander Börngen, and Matthias Sperl. Monitoring three-dimensional packings in microgravity. *Granular matter*, 16(2):165–173, 2014.

[28] O Mouraille and Stefan Luding. Sound wave propagation in weakly polydisperse granular materials. *Ultrasonics*, 48(6-7):498–505, 2008.

[29] XiaoPing Jia, J Laurent, Yacine Khidas, and Vincent Langlois. Sound scattering in dense granular media. *Chinese Science Bulletin*, 54(23):4327–4336, 2009.

[30] Trushant S Majmudar and Robert P Behringer. Contact force measurements and stress-induced anisotropy in granular materials. *Nature*, 435(7045):1079–1082, 2005.

[31] Corey S O'Hern, Stephen A Langer, Andrea J Liu, and Sidney R Nagel. Random packings of frictionless particles. *Physical Review Letters*, 88(7):075507, 2002.

[32] Leonardo E Silbert, Andrea J Liu, and Sidney R Nagel. Vibrations and diverging length scales near the unjamming transition. *Physical review letters*, 95(9):098301, 2005.

[33] X. Jia, Th. Brunet, and J. Laurent. Elastic weakening of a dense granular pack by acoustic fluidization: Slipping, compaction, and aging. *Phys. Rev. E*, 84:020301, Aug 2011.

[34] Mathias Fink. Time-reversal mirrors. *Journal of Physics D: Applied Physics*, 26(9):1333, 1993.

[35] Maxime Harazi, Yougu Yang, Mathias Fink, Arnaud Tourin, and Xiaoping Jia. Time reversal of ultrasound in granular media. *The European Physical Journal Special Topics*, 226(7):1487–1497, 2017.

[36] John Conrad Jaeger and Horatio Scott Carslaw. *Conduction of heat in solids*. Clarendon P, 1959.

[37] JH Page, HP Schriemer, AE Bailey, and DA Weitz. Experimental test of the diffusion approximation for multiply scattered sound. *Physical Review E*, 52(3):3106, 1995.

[38] Douglas J Durian. Influence of boundary reflection and refraction on diffusive photon transport. *Physical Review E*, 50(2):857, 1994.

[39] Engineering toolbox, (2004). metals and alloys - densities. Accessed on 2020-04-06.

[40] H. A. Janssen. Versuche über Getreidedruck in Silozellen. *Zeitschr. d. Vereines deutscher Ingenieure*, 39:1045–1049, 1895.

[41] Matthias Sperl. Experiments on corn pressure in silo cells–translation and comment of janssen's paper from 1895. *Granular Matter*, 8(2):59–65, 2006.

[42] Karsten Tell, Christoph Dreißigacker, Alberto Chiengue Tchapnda, Peidong Yu, and Matthias Sperl. Acoustic waves in granular packings at low confinement pressure. *Review of Scientific Instruments*, 91(3):033906, 2020.

[43] Peter Blomgren, George Papanicolaou, and Hongkai Zhao. Super-resolution in time-reversal acoustics. *The Journal of the Acoustical Society of America*, 111(1):230–248, 2002.

4. Conclusion and Outlook

In this thesis experiments were conducted to investigate elastic waves in granular packings. The sound speed at low confinement pressure was measured in the experiment GRASCHA 2[1] on-board the sounding rocket MAPHEUS 8 of DLR launched in 2019. During six minutes of microgravity, mechanically stable granular packings were prepared at pressure settings from 20 to 400 Pa. The force distribution was found much more isotropic than on ground. The sound measurements conducted showed wavefront speeds from 60 to 160 m/s, implying a pressure dependence $c_p \propto p_0^\nu$ deviating from the literature value of $\nu = 1/4$ for low pressures[2, 3] but much closer to $\approx 1/3$ and in stark contrast to the prediction of EMT, 1/6, based on Hertz-Mindlin contacts[4, 5, 6]. However, in good agreement with measured values at high pressure in the literature[7] and at low pressure in this work, a continuous increase of the exponent with pressure described by a constant logarithmic derivative over at least five orders of magnitude was found, qualitatively similar to a previously reported finding in two-dimensional systems[8]. Further work is required to investigate its microscopic origin. Measurements with the GRASCHA apparatus at even lower pressure seem feasible and should be considered. Additionally, studies of the contact force of glass beads over many orders of magnitude of force could provide insight as well as studies of the role of disorder close to unjamming.

The results for the high-amplitude behavior show the onset of shock-waves at the lowest pressure settings. At the highest amplitudes, increased attenuation was found, in accordance with the results and proposed model in [9]. For the highest pressure settings, no shock-like behavior is found. Instead a drop in wavefront speed occurs, which might suggest elastic weakening due to the strong vibrations. Clearly, more data is needed, potentially with different excitation signals.

In ground-based measurements, multiple scattering of elastic waves was investigated at low pressure ≈ 1 kPa, firstly in the GRASCHA sample cell, then in a dedicated new experimental setup. From the average incoherent sound intensity in packings within the GRASCHA cell, which suffer from a large hydrostatic gradient, a transport mean free path ℓ_T close to five bead diameters was found. Similar measurements in the dedicated new sample-cell affected by a much weaker gradient resulted in $\ell_T \approx 1.6$ - 1.8 bead diameters. In the same setup, attenuation of the coherent wave was measured to extract the scattering mean free path ℓ_s which was found in the same range. In contrast to literature results[10, 11], where $\ell_T \approx 1$ diameter, suggesting vanishing correlation length, the present results suggest a finite long correlation length which could be due to anisotropy[12] or to unjamming[13] due to the low pressure. Further work is necessary to investigate scattering in packings with stress anisotropy, possibly combined with stress-optical studies of the force-chain network.

Test measurements of wave focussing in granular media by application of inverse-filtering and time reversal were conducted. The focussed signal was found three times narrower in the granular packing than in in a air filled cell at the same parameters and similar sound speed, suggesting an increased effective aperture due multiple scattering. The focussed signals were weakened by tapping and external perturbation. More detailed studied with varying excitation strength are necessary, but such methods seem promising for studying microscopic rearrangements of the force-chain network, as found in previous work[14].

The combined efforts of wave speed measurements, diffusive transport measurements or other forms of multiple scattering measurements, stress-optical measurements and simulations could further provide insight into the effect of disorder, anisotropy and jamming on wave propagation, and the latter provides insight into elasticity of granular matter in general.

[1]

Bibliography

[1] Karsten Tell, Christoph Dreißigacker, Alberto Chiengue Tchapnda, Peidong Yu, and Matthias Sperl. Acoustic waves in granular packings at low confinement pressure. *Review of Scientific Instruments*, 91(3):033906, 2020.

[2] SN Domenico. Elastic properties of unconsolidated porous sand reservoirs. *Geophysics*, 42(7):1339–1368, 1977.

[3] Joe Goddard. Nonlinear elasticity and pressure-dependent wave speeds in granular media. *Proceedings of The Royal Society A: Mathematical, Physical and Engineering Sciences*, 430:105–131, 07 1990.

[4] Jacques Duffy and R.D. Mindlin. Stress-strain relation and vibrations of a granular medium. *J. Appl. Mech., ASME*, 24:585–593, 1957.

[5] P. J. Digby. The effective elastic moduli of porous granular rocks. *J. Appl. Mech.*, 48(4):803, 1981.

[6] K. Walton. The effective elastic moduli of a random packing of spheres. *J. Mech. Phys. Solids*, 35(2):213 – 226, 1987.

[7] X. Jia, C. Caroli, and B. Velicky. Ultrasound propagation in externally stressed granular media. *Phys. Rev. Lett.*, 82:1863–1866, Mar 1999.

[8] B Velickỳ and C Caroli. Pressure dependence of the sound velocity in a two-dimensional lattice of hertz-mindlin balls: Mean-field description. *Physical Review E*, 65(2):021307, 2002.

[9] Siet van den Wildenberg, Rogier van Loo, and Martin van Hecke. Shock waves in weakly compressed granular media. *Phys. Rev. Lett.*, 111:218003, Nov 2013.

[10] X. Jia. Codalike multiple scattering of elastic waves in dense granular media. *Phys. Rev. Lett.*, 93:154303, Oct 2004.

[11] XiaoPing Jia, J Laurent, Yacine Khidas, and Vincent Langlois. Sound scattering in dense granular media. *Chinese Science Bulletin*, 54(23):4327–4336, 2009.

[12] Trushant S Majmudar and Robert P Behringer. Contact force measurements and stress-induced anisotropy in granular materials. *Nature*, 435(7045):1079–1082, 2005.

[13] Leonardo E Silbert, Andrea J Liu, and Sidney R Nagel. Vibrations and diverging length scales near the unjamming transition. *Physical review letters*, 95(9):098301, 2005.

[14] Maxime Harazi, Yougu Yang, Mathias Fink, Arnaud Tourin, and Xiaoping Jia. Time reversal of ultrasound in granular media. *The European Physical Journal Special Topics*, 226(7):1487–1497, 2017.

Appendices

A. Additional Grascha 2 Data

A.1. Results from Sound Measurements

Packing Evolution over Time

To examine possible irreversible changes of the packing configuration during repeated acoustic excitation, the resemblance $\Gamma_{i,i+1}(0)$ of successively measured waveforms i and $i+1$ is analyzed according to:

$$\Gamma_{i,i+1}(\tau) = \frac{C_{i,i+1}(\tau)}{\sqrt{C_{i,i}(0) \cdot C_{i+1,i+1}(0)}} \quad \text{with} \quad C_{i,j}(\tau) = \int x_i(t) \cdot x_j(t+\tau) \mathrm{d}t \tag{A.1}$$

In Fig. A.1 the resemblance, the wavefront speed for low amplitudes and the confinement pressure are shown as measured during the six minute microgravity period. The sound measurement was interrupted when three readjustments of the pressure wall were performed. Each time when the sound measurement resumed, a drop in $\Gamma_{i,i+1}$ occurred, as expected. Further analysis of the resemblance is difficult since the signals contained only few kHz bandwidth, which limits the ability to detect any microscopic rearrangements in the packing, and for the lower pressure settings the attenuation was high, increasing the effect of noise which reduces the resemblance considerably even if the packing is unchanged. For further measurements in the future, alternative signal shapes might be considered that are more suitable to detect small rearrangements in the packing.

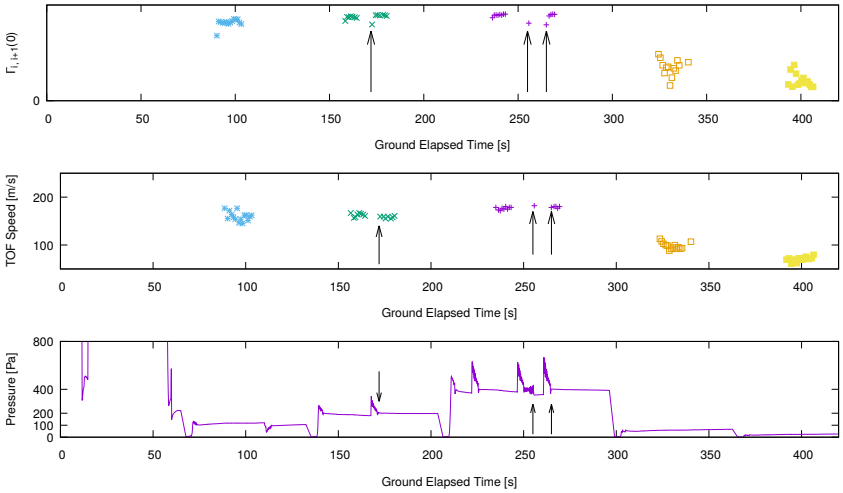

Figure A.1.: Top: *Resemblance of successive waveforms according to Eq. (A.1).* Center: *Low amplitude wavefront speed.* Bottom: *Confinement pressure vs time. The arrows indicate when the sound measurement resumed after a short pause due to automatic pressure readjustment. At these points the resemblance drops visibly.*

Degree of Coherence

Further measurements were conducted with a 200 ms signal containing 40 tone-bursts with center-frequencies from 2 - 11 kHz. This signal type was used three times for each pressure setting. Analysis

of the received signal at the accelerometers shows a drop in transmitted bandwidth as the static pressure is decreased. To quantify the coherent transmission within the granular packing we use the coherence function:

$$C(\omega) = \frac{|\langle X^*(\omega)Y(\omega)\rangle|^2}{\langle X^*(\omega)X(\omega)\rangle\langle Y^*(\omega)Y(\omega)\rangle} \tag{A.2}$$

Here $X(\omega) = \mathcal{F}[x(t)]$ is the Fourier transform of the signal measured by the close accelerometer. Accordingly, $Y(\omega)$ represents the far accelerometer. If the two signals are related by a linear response then $C(\omega)$ is close to 1. For uncorrelated noise or nonlinear distortions $C(\omega)$ will be much lower than 1. To compute the coherence function, the recorded waveform was split into N segments with 50% overlap. The ensemble-averages in (A.2) were calculated over the N segments. The FFT-based implementation of the algorithm used in the analysis program (see section C) requires N to be a power of two. To get a good compromise between number of frequency bins and samples, N was chosen to be 64. The result, as shown in Fig. A.2 clearly shows an overall decrease in transmitted bandwidth with decreasing packing pressure. For the ground test at 1 kPa (determined by the average of the side-wall force sensors) and for the in-flight measurement at 400 Pa essentially the entire range from 2 - 11 kHz is transmitted from 33 to 88 mm depth into the packing. As the pressure is lowered towards 20 Pa, only few narrow frequency ranges seem to be transmitted linearly.

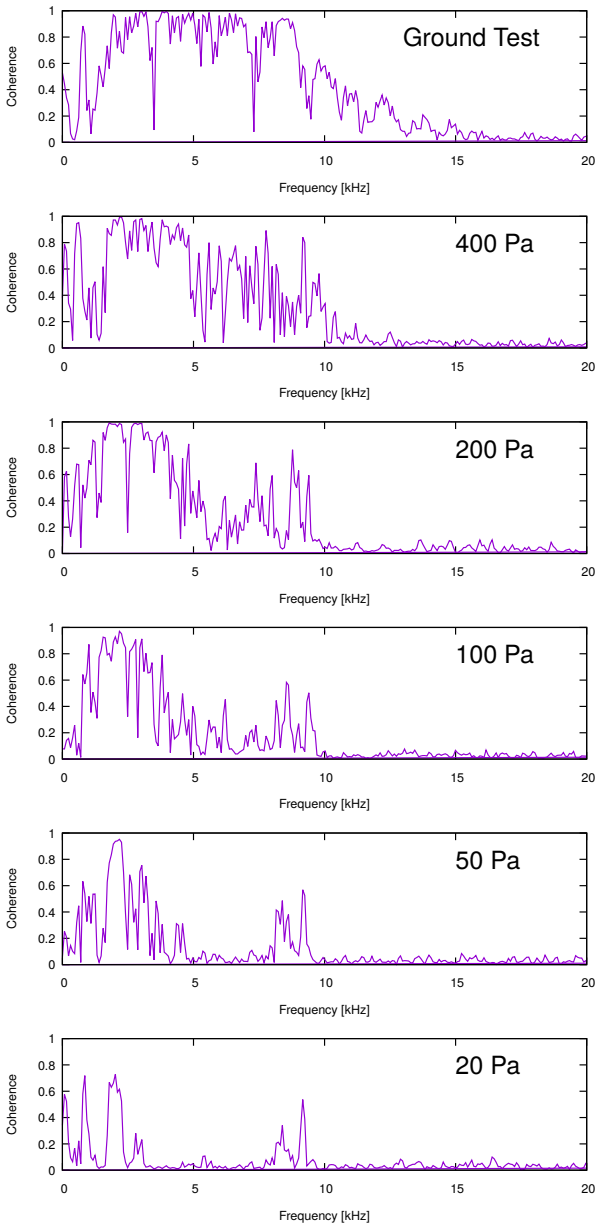

Figure A.2.: *Coherence according to Eq. (A.2) of 2 - 11 kHz tone-burst signals recorded by two accelerometers within the packing at different static pressures. For the highest pressure on ground (top) and in microgravity at 400 Pa a linear response is seen for almost the entire transmitted frequency range. Lowering the pressure results in fewer frequencies contributing to linear transmission.*

Peak Velocity vs. Peak Acceleration

After integrating the accelerometer signals and comparing the peak amplitudes, an approximately linear relationship between peak velocity and peak acceleration at the wavefront is found for the entire amplitude range as shown in Fig. A.3.

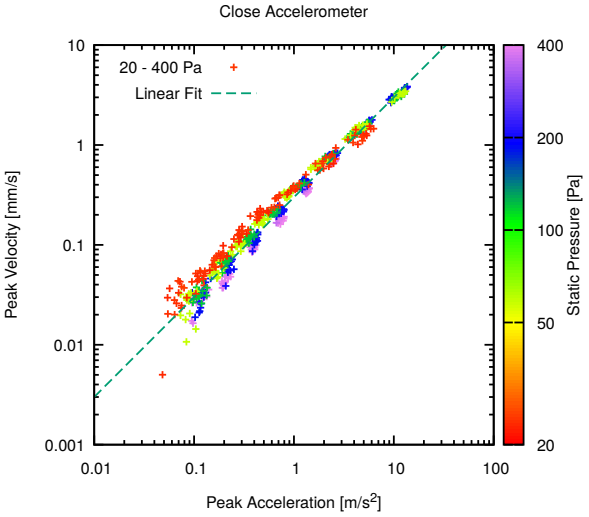

Figure A.3.: *Peak velocity vs. peak acceleration as determined from integrated and raw accelerometer signal.*

Wavefront Speed

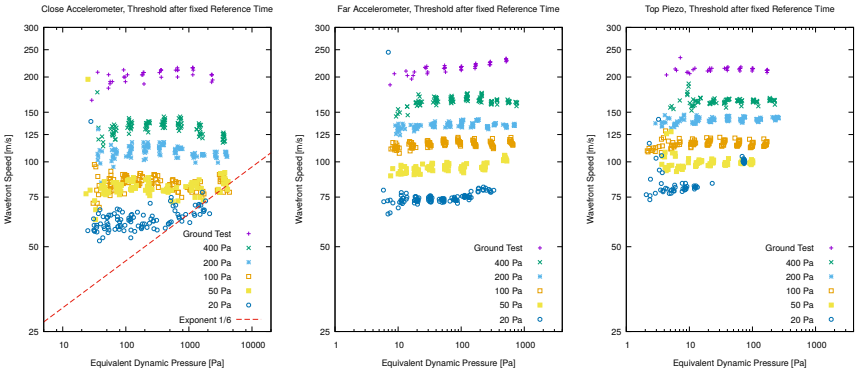

Figure A.4.: *Wavefront speed determined from relative threshold of 1/e of each single sensor signal relative to fixed reference time given by the oscilloscope trigger point on the AWG excitation signal. Shown are results for the accelerometers at 33 and 88 mm distance from the vibrating wall as well as one of the piezos at 122 mm. For the lowest pressure setting and the highest amplitude settings an increase of speed with amplitude is found as indicated by a power-law fit of exponent 1/6 according to the shock-wave model.*

A.2. Raw Signals

Acceleration at largest amplitude

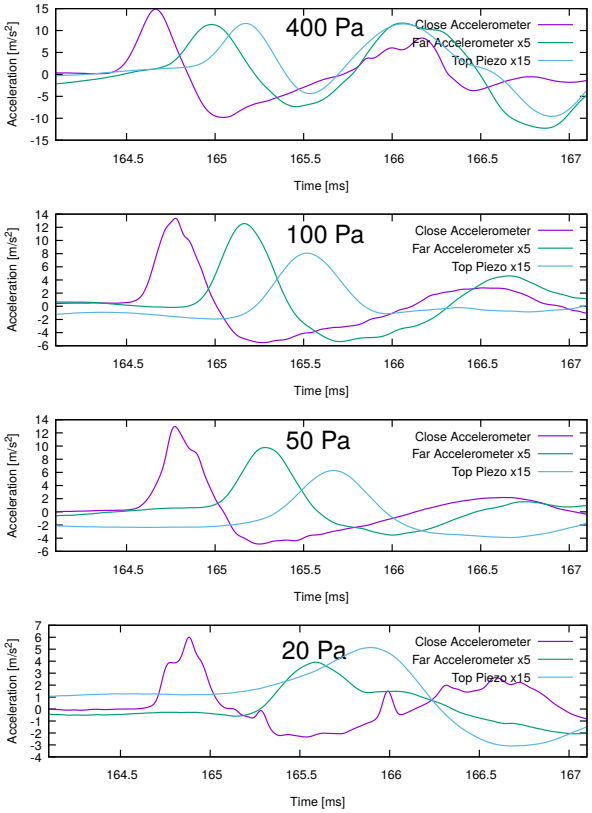

Figure A.5.: *Acceleration signal at largest amplitude setting for different static pressures. The piezo signal amplitude is scaled to units of acceleration for better comparison.*

Acceleration at small amplitude

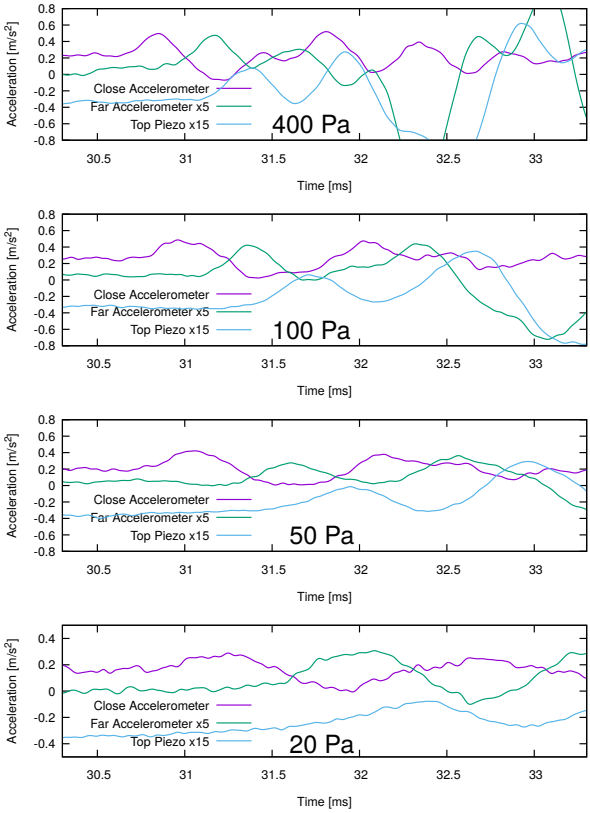

Figure A.6.: *Acceleration signal at second-smallest amplitude setting for different static pressures. The piezo signal amplitude is scaled to units of acceleration for better comparison.*

Velocity at largest amplitude

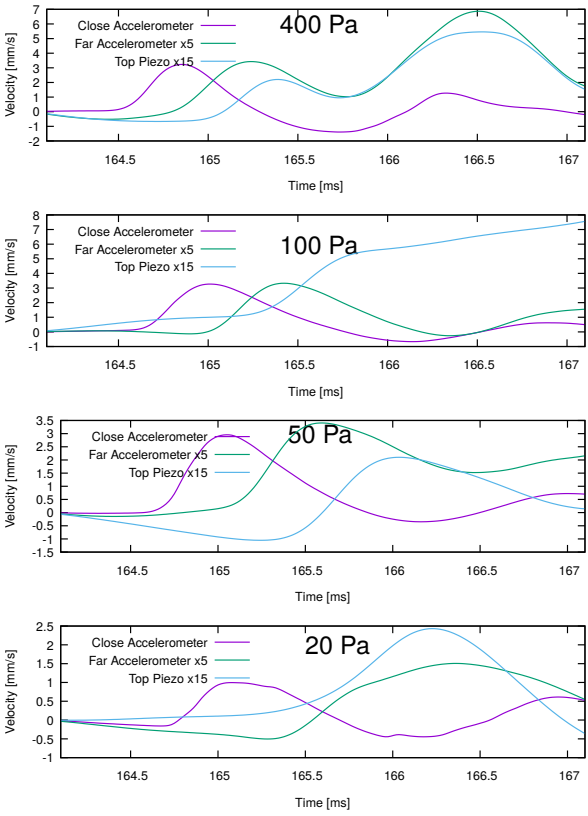

Figure A.7.: *Velocity in terms of integrated acceleration signal at largest amplitude setting for different static pressures. The piezo signal amplitude is scaled to units of acceleration and integrated for better comparison.*

Velocity at small amplitude

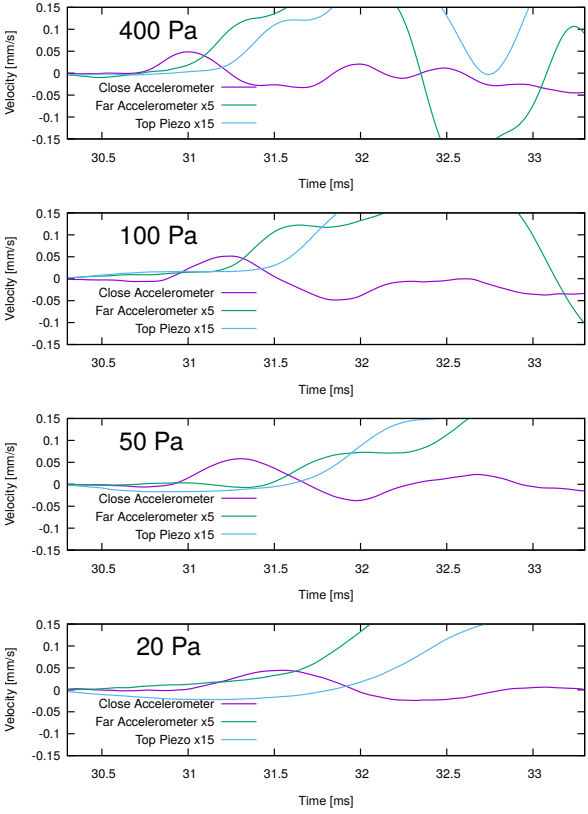

Figure A.8.: *Velocity in terms of integrated acceleration signal at second-smallest amplitude setting for different static pressures. The piezo signal amplitude is scaled to units of acceleration and integrated for better comparison.*

Displacement at largest amplitude

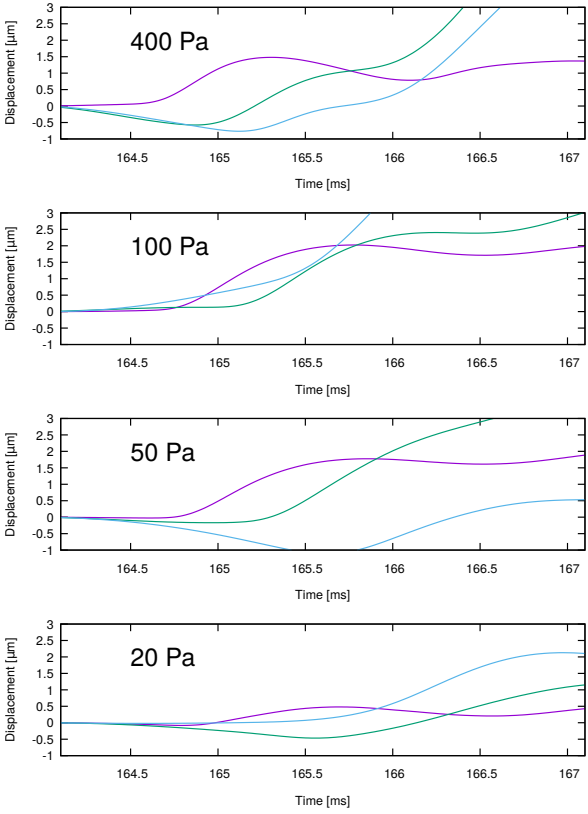

Figure A.9.: *Displacement in terms of twice-integrated acceleration signal at largest amplitude setting for different static pressures. The piezo signal amplitude is scaled to units of acceleration and integrated twice for better comparison.*

Displacement at small amplitude

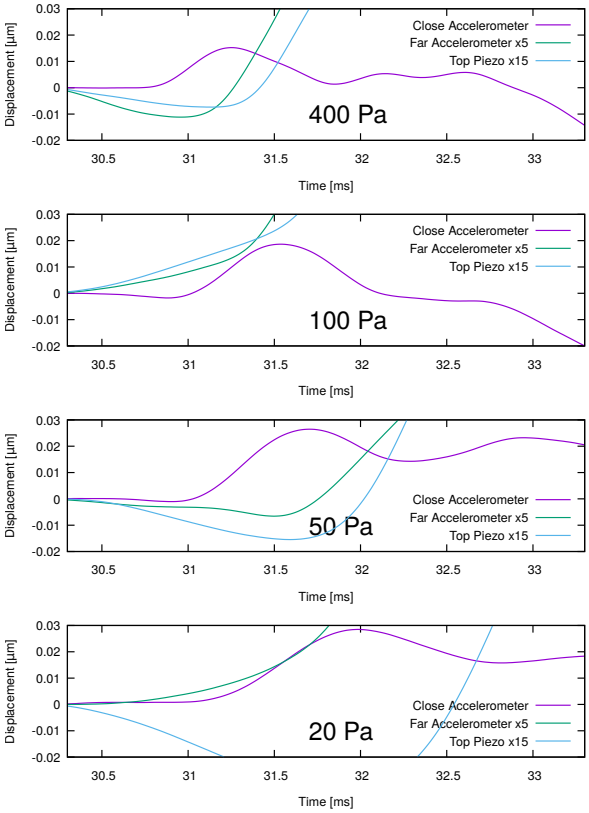

Figure A.10.: *Displacement in terms of twice-integrated acceleration signal at second smallest amplitude setting for different static pressures. The piezo signal amplitude is scaled to units of acceleration and integrated twice for better comparison. No useful displacement signal is found for the far accelerometer and the piezo due to low-frequency artifacts.*

B. Overview of Grascha 2 Experiment Software

B.1. Overview

The *Grascha 2* experiment operation and data acquisition is implemented by software on the `Intel NUC`. In addition, there is an `Arduino Uno` microcontroller on which monitoring and adjustment of packing pressure is implemented. The software running on the `NUC` is responsible for coordinating the simultaneous operation of the oscilloscope (`Picoscope 5000` series), the high resolution ADC (`Picolog ADC-24`) and the microcontroller as well as the overall measurement campaign consisting of many pressure and acoustic signal settings.

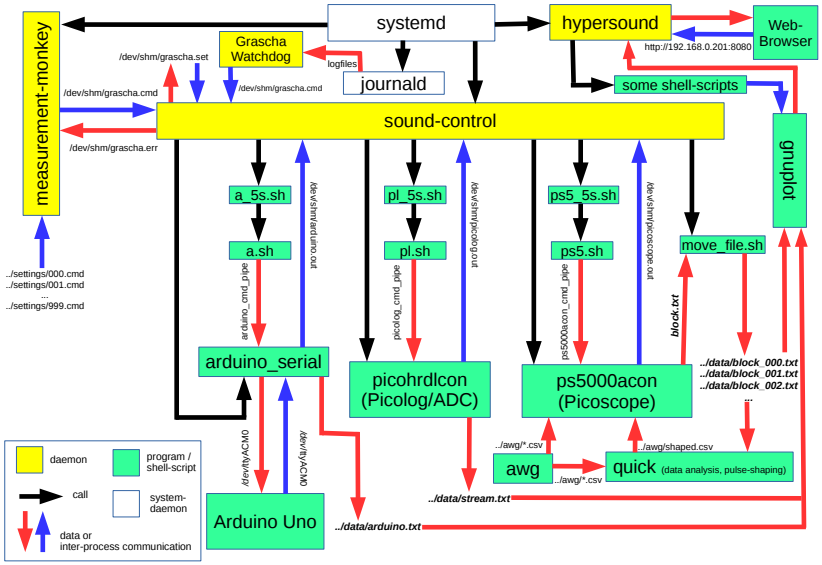

Figure B.1.: *Schematic diagram of programs running on the NUC and their interactions.*

The operating system on the `NUC` is `Open Suse Linux`. We make extensive use of its automation, logging and remote control features through usage of shell scripts, custom-written `systemd` services, `ssh` and a custom written HTTP-server and web-interface. The software is divided into several concurrently running programs dedicated to specific tasks. They are communicating with one-another via FIFO-pipes, named pipes, shared memory and TCP-sockets. Bidirectional communication between `NUC` and `Arduino` is implemented via virtual serial port over USB. Remote control and user interaction is possible via LAN connection as long as the Ethernet umbilical cable is attached. The general software architecture is highly modular in order to simplify maintenance, debugging and development. In most cases, any program can be recompiled and restarted without affecting the operation of other programs and the overall measurement campaign. In the most extreme case, a software update is still feasible minutes before liftoff without interrupting the countdown. The modular design is inherently failure tolerant i.e. the crash of any program does not affect any other program. Each program is being continuously monitored and checked for nominal operation by other programs and `systemd` services. If non-nominal behavior is detected, an attempt to restore a well-defined state of the program is made. If this fails, the program is restarted. In case of the `Arduino`, it is reset by resetting the serial connection

if necessary. Such error handling takes up to 10 seconds for the `Arduino` and much less than a second for most programs on the `NUC`. At all times the parameters defining the state of the experiment (device settings, measurement parameters, current state of the campaign) are tracked by `Sound-Control` and stored in memory such that in the event of a crash of any programs (including `Sound-Control` itself) the state of all affected programs and devices can immediately be restored. This makes the *Grascha 2* software suitable for microgravity and long-duration ground-based measurements where user interaction is restricted or not possible.

B.2. Low-Level Programs

B.2.1. Picoscope and Picolog programs

The manufacturer of the oscilloscope and data-logger provides drivers for `Linux` and documentation of the API, along with example code in `C`. Based on the programs `ps5000acon` for the oscilloscope and `picohrdlcon` for the data-logger, command-line programs were prepared that are suitable for automated measurements. To enable supervision of these programs by `sound-control` as shown in Fig. B.1, interprocess-communication had to be implemented for each program.

In order to receive commands, the program reads from a named pipe. Tho provide immediate feedback to the sender of such command, indicating whether the command was successfully received, two shell scripts are used. The first script calls the second script with a list of commands as arguments. The second script writes these arguments to the named pipe, one-by-one. The write blocks until the pipe was read by the oscilloscope/data-logger program. If the second script exits within a time limit of five seconds, then the first script exits normally and writes `"OK"` to `stdout`. If the time limit is exceeded i.e. the write operation is still blocking because the pipe was not entirely read and closed by the oscilloscope/data-logger program, indicating a problem with the program, then the first script terminates the second script, exits with an error code and writes `"NO RESPONSE"` to `stdout`. The mechanism can be tested without `sound-control` by calling the first script from the command-line with a list of commands as arguments. This also provides a rudimentary keyboard interface to the oscilloscope/data-logger programs for testing and debugging.

In order to write status and error messages, a form of shared memory is used. Each program writes its status and error messages to a file in `/dev/shm/`, which represents a ram-disk or filesystem in memory. It is not written to the hard-disk, which helps reduce number of read/write operations on the SSD that would otherwise unnecessarily consume time and wear the SSD down over time. The files are accessible to other programs. The oscilloscope/data-logger program writes a message to `/dev/shm/` and immediately closes the file. The program is then ready to receive new commands from the name pipe.

The different mechanisms are chosen such that `sound-control` can at any time send a command to the oscilloscope/data-logger program and get an immediate confirmation that the command was received or not. In the latter case `sound-control` can take measures to handle the problem, otherwise it can take care of all other programs it has to supervise. On the other hand, the messages sent by the oscilloscope/data-logger program are not read immediately by `sound-control`, but at a later time, when `sound-control` is ready to receive the message and not busy handling the other programs.

For the oscilloscope program an interface to set up and trigger the signal generator was implemented. The latter has to be possible during a time when the oscilloscope is armed and waiting for the trigger or when it is in the process of recording a signal. In a typical sound measurement, first the scope is armed by a non-blocking call to the API, then the program waits for a call-back to a function that stores any data received from the scope buffer to disk. During this waiting period, the program waits for one or many commands from the named pipe to trigger the signal generator upon request. If a waveform is successfully measured and saved to disk, the program writes a `UNIX`-timestamp with millisecond precision to the file header, representing the time when the last trigger for the signal generator was

sent. For the recorded waveforms, each reading contains the time in nanoseconds and the voltage for each channel in millivolt (as float).

The data-logger program is operated by starting and stopping a continuously running measurement. A UNIX-timestamp with millisecond precision is provided for each reading. The channel readings are converted from counts to millivolts after analog-digital conversion.

B.2.2. Arduino Code

The Arduino Uno microcontroller maintains a virtual serial port through which it communicates with the NUC. The port remains connected through the entire runtime of the microcontroller code. Closing the port from the NUC-side resets the microcontroller, which can be done on purpose if the microcontroller malfunctions or needs to be re-flashed to update the code. The microcontroller reads commands from the serial port, such as requests for pressure readjustment to a specific target pressure, or for offset calibration. Further possible commands force the microcontroller to continuously report pressure readings or to continuously readjust the pressure wall position in order to keep the pressure at a specific value despite external perturbation. It is also possible to change the control loop parameters via command, such as the maximum acceptable pressure error, maximum number of iterations and minimum runtime of the linear motor during one iteration of the pressure control loop. The magnets used to shake the piezos to prevent glass beads from getting stuck between the piezo and the sample cell wall are also activated and deactivated via command over the serial port.

The nontrivial part of the packing preparation protocol is implemented in the microcontroller code. Upon command, or when in continuous readjusting mode, the requested pressure is compared with the actual pressure, determined from the average of the three side-wall force-sensors. If the maximum allowable error is exceeded or the actual pressure falls below the allowable absolute minimum, then a readjustment is initiated. Otherwise, the microcontroller refuses to readjust the wall and reports "ok, pressure reached" to the serial port. The readjustment itself is implemented as described in section 2.3.3, with an initial over-/undershoot applied to the set pressure and a continuously decreasing error multiplier. To help the packing reach a stable state, strong vibrations are applied as a form of tapping. For this purpose, the microcontroller repeatedly sends requests for "hammer hits" over the serial port, which are then handled by sound-control and the picoscope program.

It is possible to compile the microcontroller code and flash it using only a command-line interface (via SSH-connection to the NUC) without the Arduino IDE. For this purpose two shell scripts were written. Before re-flashing, the serial port must be made available by closing any program that uses it to communicate with the microcontroller (see next section).

B.2.3. Arduino Serial Communication Program

To provide mechanisms for communication between the microcontroller and sound-control analogous to the mechanisms used for the oscilloscope and data-logger programs, a dedicated serial communications program was implemented in C++. It concurrently reads from the virtual serial port connected to the microcontroller and writes the result to a file in /dev/shm/ while reading from a named pipe and writing the result to the serial port.

This program also adds UNIX-timestamps with millisecond precision to each pressure reading received from the microcontroller before writing it to /dev/shm/. The timestamp represents the time when the reading was taken by the microcontroller. It is based on a millisecond timestamp sent by the microcontroller, which represents the time since the last reset. To relate it to the UNIX-time according to the system clock of the NUC, a time synchronization is necessary. This is implemented within this serial communications program, by repeatedly sending requests for single pressure readings to the microcontroller and measuring the time of request and response to estimate the offset between the NUC system clock and the microcontroller clock. The synchronization is performed each time the serial

communications program is restarted and thus the virtual serial port connection to the microcontroller and the microcontroller itself is reset.

B.3. High-Level Programs

B.3.1. Sound-Control

This program is mainly responsible for coordinating the operation of the programs for the oscilloscope, data-logger and microcontroller. It keeps track of all device settings at all times. It supervises the mentioned programs i.e. it ensures they are in a known, well-defined state by checking their status and responsiveness. If any deviation, crash or unresponsive state occurs, `sound-control` restores the well-defined state by sending appropriate commands to the affected program or by restarting it if necessary. `sound-control` also acts as an interpreter of high-level commands issued by `measurement-monkey`, or by user-input. The program must be run as `systemd` service. Then, if `sound-control` itself crashes, it is automatically restarted. The program is implemented in `C++`.

Inter-process communication is implemented in three different ways: via `/dev/shm`, via named pipe and via `FIFO`-pipe. Additionally, background processes can be spawned. `sound-control` reads commands from `/dev/shm/grascha.cmd` and status messages from the microcontroller, oscilloscope and data-logger from `/dev/shm/arduino.out`, `/dev/shm/picoscope.out` and `/dev/shm/picolog.out`. It writes its own status messages to `stdout`. For errors and major events, such as successful or failed sound measurements, device reset or the `SOE` signal, messages are written to `/dev/shm/grascha.err`. When `sound-control` runs as a `systemd` service, then its output is logged by `journald`.

`sound-control` continuously reads messages from the above-mentioned `/dev/shm/` files and interprets them. Any incoming commands are written to a list, implemented as a double-ended queue, from which they are executed one-by-one. Some commands are available that alter the list itself to facilitate high-priority commands, repetition of previous commands or to abort one or a list of many measurements. There are high-level commands such as `CheckAll`, `SetPressure` and `Measure` that automate procedures that consist of many steps involving device-specific low-level commands for multiple devices (microcontroller, oscilloscope, data-logger) or filesystem operations. Such commands, are implemented as functions within `sound-control`. In these functions, often many checks of device status and readiness with different timeouts are implemented (such as: is the pressure acceptable for the planned sound-measurement ? is the oscilloscope armed? is the time to send the AWG trigger reached? was the AWG trigger received within a certain time window? etc.). It is possible to send device-specific low-level commands to `sound-control`, which then relays them to the appropriate device via an external "interpreter". For commands to the microcontroller, the oscilloscope or the data-logger, the shell-scripts mentioned in the previous sections are called synchronously i.e. the interpreter script is spawned by `sound-control`, which keeps a pipe open until the interpreter process exits. Any status or error message from the interpreter, such as "`OK`" or "`NO RESPONSE`" is read by `sound-control` through the pipe.

The interpreters for the devices are the scripts mentioned in the previous sections about the programs for the oscilloscope, data-logger and microcontroller. Commands, intended for these interpreters must be preceded by the interpreter name, here either `picoscope`, `picolog` or `arduino`. Additionally, the system shell can be used as an interpreter. It can be used to executes commands either synchronously, by specifying the interpreter name `cmd`, which will force `sound-control` to send the specified command to the system shell and wait until it returns before continuing with the next command, or by specifying `cmda`, which will lead to asynchronous execution i.e. `sound-control` will not wait but immediately continue with the next command. For (most) internal commands, implemented within `sound-control`, the interpreter `sndctrl` must precede the command. To execute a list of commands read from a specified file, the command `sndctrl CallScript` followed by the filename is used. Such a file (or "`Grascha`-script") may contain any of the mentioned commands including further

CallScript commands.

The main loop repeats the following three steps: firstly, sound-control reads new status messages from the other programs as well as new commands. The messages are interpreted and the status of each device is noted. Then, if the command-list is not empty, the oldest command in the list is executed. If the command specifies a change of device settings, then in the new desired setting is stored in /dev/shm/grascha.set and it is then applied to the respective devices by sound-control by sending low-level commands to the device-specific programs via the interpreters.

The more complex commands SetPressure and Measure involve several waiting periods of different duration during which sound-control waits for feedback from a device-specific program. During such a waiting period, sound-control continues to check for new messages from all programs as well as for new commands. The latter are not executed but stored in the command list for later execution, unless an ABORT command is issued.

If at any point a problem is detected, e.g. by feedback from an interpreter, by a specific timeout or a message indicating a problem, then an exception is triggered. Several exception handlers are used to handle problems related to the device-specific programs. The latter are checked for readiness and responsiveness, and reset if necessary. Then sound-control resumes running the main loop. During execution-handling, triggering of further executions is disabled.

The detection of SOE is implemented in sound-control in the following way: the last command in the initial script .../settings/000.cmd, which is called sndctrl WaitForSOE forces sound-control to delay further execution of commands in the command list until SOE is detected. During this waiting period, sound-control continuously checks for new messages and, additionally, conducts repeatedly status checks of all devices. If a device problem triggers an execution, it is handled and the main loop is resumed. The waiting status is noted in /dev/shm/grascha.err along with all settings, such that, if sound-control is restarted by human intervention or automatically in case it crashes, it fully remembers the last state. In any case sound-control continues to wait for SOE. Then, once a LO (lift-off) message is received from the microcontroller, which sends it after detecting the lift-off signal from the MAPHEUS service module, then sound-control waits 72 s for a SOE message from the microcontroller. If the SOE message is received, regardless of whether the LO message was previously received or not, or if the timeout is reached, then sound-control writes SOE! to /dev/shm/grascha.err and to stdout and resumes execution of commands.

Several compile options exist. In the flight-version, sound-control checks the confinement pressure before measurement of each waveform. During the MAPHEUS 8 mission, this lead to three pressure readjustments between sound measurements, as the pressure was found outside a 20 Pa specified tolerance. In another version, sometimes used in ground-based measurements, these repeated pressure checks are omitted. This enables long-duration measurements (of several days) involving irreversible changes in the packing configuration under acoustic excitation, without intervention of the pressure-control loop, unless explicitly demanded by a command in a script file.

B.3.2. Measurement-Monkey

measurement-monkey reads major status messages from sound-control via /dev/shm/grascha.err and writes its own status messages to /dev/shm/monkey.info. This program, implemented in C++, reads commands containing pressure settings and parameters for sound measurements from files contained in ../settings/ and sends them to sound-control by appending them in blocks of lines to /dev/shm/grascha.cmd. A block may contain at most one sndctrl Measure command, after which measurement-monkey waits for confirmation by sound-control that the requested measurement was conducted successfully or that it failed. In the latter case the measurement will be requested again (this is currently disabled). If multiple measurements are requested by a single sndctrl Measure command followed by the number of measurements, measurement-monkey will wait until all requested measurements are performed or until a measurement fails before continuing with the next command block.

The time limit for each pressure setting as well as the time limit for the entire measurement campaign are implemented in `measurement-monkey`. Once the initial settings and tests, as written in `../settings/000.cmd`, are completed, `measurement-monkey` waits for the confirmation of the `SOE` signal. It must be found in `/dev/shm/grascha.err` and is written by `sound-control` as described in the previous section. Then, `measurement-monkey` loads and processes each settings file as described above. If the timeout per pressure setting is reached, then whatever commands remain in the current setting file will be skipped and the next setting file will be loaded. If the time limit for the campaign is reached then `measurement-monkey` jumps to the final file, `../settings/999.cmd`, which contains instructions to prepare a final (high) pressure setting, stop all programs, move and compress the datafiles and safely shutdown the `NUC` in preparation of reentry and landing.

`measurement-monkey` is run as a `systemd` service so its output is logged by `journald`.

B.4. User Interface

B.4.1. Hypersound HTTP-Server and Web-interface

As shown in Fig. B.2, there is a rudimentary web-interface providing a live-view of recently measured data from all sensors, including static-force sensors, oscilloscope, and CPU temperature sensors. Status messages from `sound-control` as well as further status messages, as selected by the human user, are continuously displayed. The most critical commands are also exposed here, such as starting/stopping of most `GRASCHA` programs, triggering a measurement, simulating the `LO` and `SOE` signals for test purposes and shutdown/reboot of the computer. Device problems can be simulated here by stopping a device program during a measurement or during the `SOE` waiting period, to test how fast `sound-control` can correct the problem.

On the low-level side, this is implemented with a custom-written HTTP-server called `Hypersound` which is written in `C++`. It also acts as a parser for HTTP-requests, which are compared to a list of known requests and interpreted accordingly. One simple textfile is sufficient to configure it. If a known command is received, a shell-command is executed, as specified in the configuration file, or a notification is written to a file in `/dev/shm/`. This design make `Hypersound` unsuitable for exposure to the public Internet. It must only be used within a local network such as the LAN-connection between the experiment on-board the rocket and the computer in the launch control room. Commands that require root-privileges, such as shutdown/reboot of the computer, are not directly executed by `Hypersound`, which only has normal user-privileges. Instead, a request for shutdown etc. is written to a file in `/dev/shm/` and parsed/executed by a dedicated shell script running as a `systemd`-service with root-privileges. All traffic related to the web-interface, such as plots and audio files, is handled by `Hypersound`. For large files of several GB, other methods of file transfer are recommended that provide higher speed, such as SCP.

The website itself is implemented as a combination of static HTML and shell-scripts. The latter take 'drafts' of HTML pages containing placeholders and replace those placeholders by status messages or data provided by `journald` and files in `/dev/shm/` containing the output of the device-related programs. A list of stored data files can also be provided using `ls -lth`. The plots, shown in the web-interface, are created on the `NUC` after HTTP request using `GNUplot`. They are provided as `.svg` vector images, enabling zooming in the browser-window on the remote computer without blurring the image due to limited resolution. To provide a seemingly continuous live-view, requests for new plots are sent from the remote computer once per second. This is implemented in `JavaScript`, its only usage in the web-interface. Audio files providing an audible preview of the oscilloscope data are generated on HTTP request using `quick` (see section C) in combination with `SoX`. The resulting `.ogg` files are available for playback, as implemented per HTML5 capability.

During a nominal countdown, no human intervention is required, but a human operator must monitor the status of the service module signal during the payload checkout test. In the `GRASCHA` web-interface

this is done using the user-configurable status display in the center of the screenshot in Fig. B.2, which has be set up to show the "Latest Arduino Readings".

B.4.2. Command Line Interfaces

Full access to all GRASCHA debugging and test functionality is available via command-line using a SSH connection. Apart from the Linux shell, which provides access to all above mentioned programs and scripts, there is a dedicated GRASCHA shell through which the human operator can send commands to sound-control according to the same syntax as used in the scripts or settings for the measurement campaign. All programs can be re-compiled using gcc or g++ and restarted. In case of the microcontroller, its serial connection has to be reset to flash new code as described in section B.2.2.

Special caution is necessary if measurement-monkey is restarted, as it does not store its exact execution state (or which settings file it is currently interpreting) in a non-volatile manner. Therefore, it starts always with the file containing the initial settings and test measurements. To enable a clean restart, the file /dev/shm/grascha.err needs to be cleaned. This is done in the GRASCHA shell with the commands sndctrl ForgetLO and sndctrl ForgetSOE or with the respective commands in the web-interface.

From the Linux command line, the device command interpreters can be directly addressed to send commands directly to the microcontroller, oscilloscope and data-logger, bypassing sound-control entirely. This is useful for testing these programs individually.

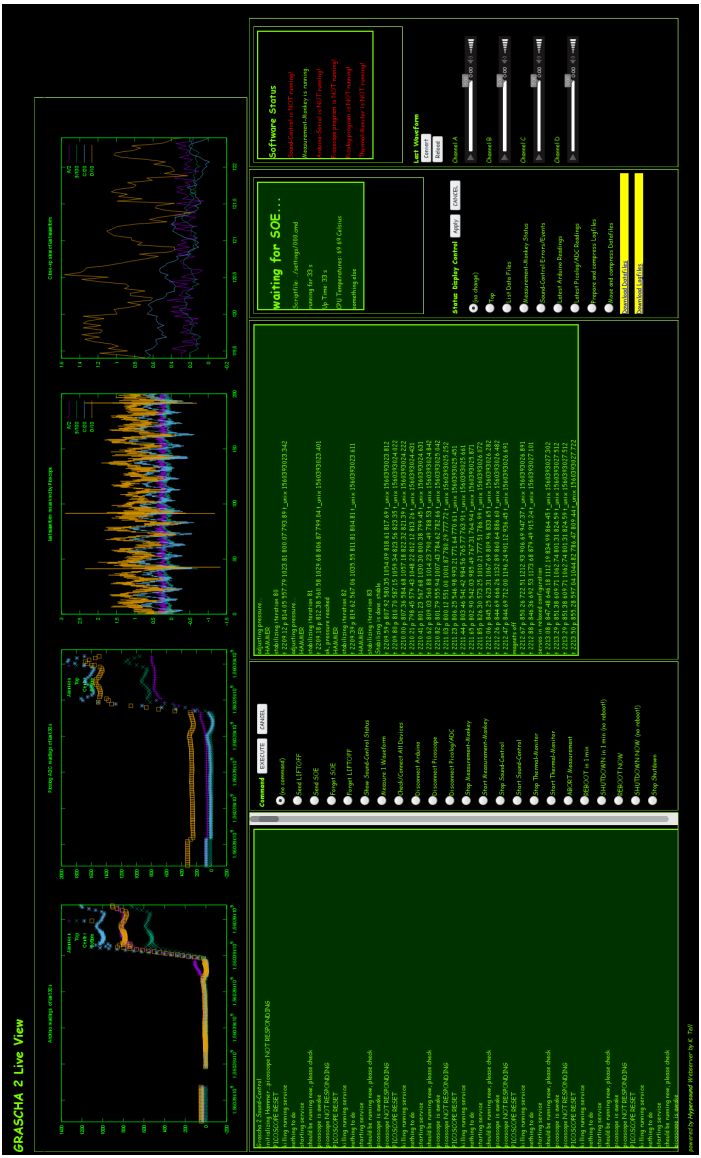

Figure B.2.: *Screenshot of Grascha 2 web-interface.* Top row: *Live-plots of static force-sensor readings with offset-correction (left) and raw voltage values (center left) and waveforms most recently measured by the oscilloscope (center right) with a close-up view showing interesting parts of the signal (right).* Bottom row: *Status messages from sound-control (left), list of frequently used commands for easy access (center left), further status messages from a user-selected program or list of stored data files (center), further status messages and commands as well as audio-preview of sound measurements converted from oscilloscope data (right).*

C. Overview of quick (Grascha 2 Analysis Tool)

This is `quick`, the analysis tool for `Grascha 2`.

A list of all possible command line arguments can be generated by running `arglist.sh` which reads them directly from the source code and presents them in a more readable format.

To build quick and install it in `/home/USERNAME/bin/` run `make.sh` which uses `gcc` to compile three binaries:

`quick`
The debugging version containing additional information for debugging with `gdb`

`quick_O3`
The optimized version, compiled with optimization level 3. If speed matters, use this one.

The binary `/home/USERNAME/bin/quick` should be equivalent to `quick_O3`.

Even a Windows binary, `quick_w64.exe`, is also compiled.

General operation of the program:

`quick` reads data from one or two text files. For each file the number of columns must be specified. Columns are seperated by tabs, spaces or commas. Any lines that do not contain the specified number of columns will be ignored. Binary data is not supported. If more than one column exists, the first column is assumed to contain time or frequency (common x-axis) while further columns are assumed to contain real signal (e.g. signal voltage) or the spectrum modulus (e.g. transmission) for each channel.

All arguments are optional. The first few arguments, if provided, must be in this order:

```
quick [filename] [number of columns] [start time] [stop time]
```

All other arguments can be given in arbitrary order.

If the maximum of the first column is larger than 1e5 then `quick` assumes it contains time in nanoseconds (as used in Picoscope raw data). This unit is inconvenient for most Grascha analysis. Therefore `quick` will convert the time from nanoseconds to milliseconds before attempting any further analysis.

Calculations are performed on data stored in memory. For FFT-based calculations, extra memory will be used temporarily, several times the size of the original data.

Finally, results are written to a new file. Its name is the original filename plus an extension.
Example:

`input_file.csv -> input_file.csv.res`

Additionally, status messages and warnings are printed to `stdout` containing some selected results from the analysis. They can be easily parsed with `grep` and `cut` when `quick` is run in a shell script, as is often the case.

Common examples:

`quick`
(no arguments provided) This will generate an example file called test.res which contains 4 columns: x-values from 0 to 100, y-values representing a Gaussian centered at x=50, a Gaussian at x=50.5 and a Delta function at x=50.

`quick file.txt 5 0 200`
This will read the file file.txt into memory, parse its content assuming column 1 is the x-axis and colums 4-5 are y-axis channels. A region of interest from x=0 to x=200 will be selected. The data will be normalized and analyzed for global maxima and the first significant local maxima. A simple time-of-flight analysis will be performed to get the speed of sound from measured oscilloscope data. The normalized data will be saved to disk as file.txt.res

`quick file.txt 5 0 200 nonorm`
same as above, but no normalization is performed
Note: without normalization, many types of analysis will be skipped, such as time-of-flight and all FFT based calculations. If you need such analysis but do not want the result to be affected by normalization, use unnorm instead of nonorm

`quick filte.txt 5 0 200 smooth .1 down 10`
the data is downsampled by a factor of 10, normalized, convolved with a Gaussian kernel of width 0.1 and the result is saved to disk as file.txt.res
Note: This convolution is calculated in the time-domain. Only small widths shall be used to keep computation time within acceptable limits. This method is useful for removing white noise without introducing any shifts or ringing artifacts. For more elaborate filtering, the FFT-based filters shall be considered (see further below).

`quick file.txt 5 0 200 nonorm differentiate`
differentiates each column (2-5) with respect to column 1 and saves result as file.txt.dif

`quick file.txt 5 0 200 nonorm integrate`
integrates each column (2-5) with respect to column 1 and saves result as file.txt.int

`quick file.txt 5 0 200 time .1 nonorm`
applies linear time shift by adding 0.1 to each x-value (first column) while the y-values (other columns) remain unchanged. x=0 is shifted to x=0.1 and x=200 is shifted to x=200.1. Result is saved to disk as file.txt.res
Note: linear shift is performed before any further analysis and only affects first data file, not the ref data file.

`quick file.txt 5 0 200 rotate .1 nonorm`
applies circular time shift of 0.1 by changing to order of rows in all columns. x-range remains unchanged at 0..200 but row at x=0 is moved to x=0.1 while row at x=199.99 is moved to 0.09. Result is saved to disk as file.txt.res

Note: circular shift is performed before any further analysis and only affects first data file, not the ref data file.

`quick file.txt 5 0 200 fft`
the two-sided fourier transform will be calculated using radix-2 Cooley-Tukey FFT with sufficient zero-padding to avoid wrap-around artifacts and the result will be saved to disk as file.txt.fft

`quick file.txt 5 0 200 filter identity`
The forward fourier transform will be calculated as mentioned above. Then the inverse transform of the result will be calculated and the result will be written to disk as file.txt.fil
Note: while the y-axis will not be changed (apart from normalization and possible artifacts), the x-axis will be shifted such that the origin corresponds to half the x-scale. The sample count will be increased to be a power of 2

`quick file.txt 5 0 200 filter identity high .1 low 10 notch 2 window 100 gaussian`
same as above, but a high-pass filter of corner frequency 0.1 will be applied as well as a low-pass filter with corner frequency 10 and a notch filter at center frequency 2. Prior to this, the data is windows by a Gaussian of width 100.

`quick a.txt 5 0 200 ref b.txt 5 1 filter correlation`
Five columns will be read from a.txt and the second of five columns will be read from b.txt. The cross-correlation of column 2 (=channel 1) of b.txt and each column of a.txt (column 1-5 or channel 1-4) will be calculated. The highest correlation peak for each channel pair will be printed to stdout. A file containing all four correlation functions will be saved to disk as a.txt.cor

`quick a.txt 5 0 200 ref b.txt 5 1 filter convolution`
same as above, but convolution instead of correlation is calculated and saved to disk as a.txt.con

`quick a.txt 5 0 200 ref b.txt 5 1 filter inverse`
same as above but inverse convolution $(a * b^{-1})$ is calculated

`quick output.txt 5 0 200 ref input.txt 5 1 filter response`
assuming output.txt is the measured output of a linear system to an input given by input.txt, `quick` will estimate the impulse response and save it to disk as output.txt.resp

`quick output.txt 5 0 200 ref input.txt 5 1 filter response causal`
same as above, but here only the minimal-phase impulse response is calculated by imposing Kramers-Kronig relations

`quick file.txt 2 0 200 picoscope`
column 2 (channel 1) of file.txt will be used to create a single channel csv file to be used for the Picoscope AWG

`quick file.txt 5 0 200 audio 200 4`
column 5 (channel 4) of file.txt will be converted to a csv file representing 200 milliseconds and saved as file.txt.dat which can be converted to wav or ogg audio files using sox

`quick file.txt 5 0 200 wigner 1 .2`
`quick` will take channel 1 (column 2) of file.txt and calculate its Smoothed Wigner-Ville distribution using a Gaussian window of 0.2 milliseconds in time and a corresponding Gaussian window in the frequency domain where the width is chosen to satisfy the Gabor-Heisenberg uncertainty. This will

consume a lot of memory (proportional to N^2 for N samples in the original data). The resulting Wigner-Ville distribution will be saved as a grayscale picture in PGM format under the name file.txt.wig and the first moments of the distribution will be saved under file.txt.mom

```
quick file.txt 5 0 200 nonorm env
```
calculates envelope of data via Hilbert transform and saves result as file.txt.env

```
quick file.txt 5 0 200 nonorm intensity
```
calculates intensity envelope of data via Hilbert transform and saves result as file.txt.inten

```
quick file.txt 5 -10 10 fit gauss 1 -.123 .2
```
A region of interest from -10 to 10 will be chosen from file.txt, then `quick` will fit a Gaussian to the data in each channel (1-4) using the parameters amplitude, position and width with initial values of 1.0, -0.123 and 0.2. The results will be written to stdout. No output is written to disk.

It is encouraged to run N instances of `quick` in parallel if N cpu cores are available and if sufficient memory is available to permit analysis of several data files in parallel.

If you want to contribute to `quick` development, get an up-to-date local copy of the master branch from the `git` repository (on `mp-cummins` or on the MP `gitlab` server), make sure your changed code actually builds and send me a diff. If i approve your changes, i will then merge them into the master branch.

E-mail for questions, suggestions, etc:
`karsten.tell@dlr.de`

D. Analysis Methods

D.1. FFT

In QUICK the FFT is implemented according to a radix 2 Cooley-Tukey algorithm[1] in the following way:

First of all, in QUICK, up to two data-files are loaded into memory. The first data-file, called 'original data', may have multiple columns where each column represents an oscilloscope channel and the first column representing time. The second file, called 'reference data', may contain a different number of columns but only one user-specified column is used for further analysis. All columns share the same time axis. Before any FFT-based operation can be performed, QUICK makes sure the columns from both the original and reference data have the same number of rows, which is not required for the raw data provided in the input files. If the reference data has fewer rows than the original data, then zeros are inserted at the end. If the original data has fewer rows than the reference data, then values corresponding to the mean of the respective channel are inserted at the end of each channel. In that case, additional time-values are inserted at the end of the time column.

As the FFT algorithm requires the sample count to be an integral power of two, which is not required for the raw data in the input files, it may be necessary to add or remove rows. For this purpose, QUICK inserts zeros at the end of each channel column in both the original and reference data until the new sample count satisfies two conditions: firstly, it is a power of two. Secondly, it is twice the old sample count if the old sample count was already a power of two or four times the largest power of two that is still smaller than the old sample count. This ensures that there are at least as many zero samples as original samples. This is found necessary to avoid artifacts from the FFT. The time column is extended by inserting additional time values at the end to match the number of rows of the channel columns.

The frequency column is created with the same number of rows as the time column but with the frequency $f \in [-f_{max}; f_{max}]$ with $f_{max} =$ the number of rows divided by twice the total time interval length. This is done as the result of the FFT will yield the Fourier transform for both negative and positive frequencies.

The FFT itself is calculated for each channel column using the function `RecurseFFT(interval)` of some specified index interval within the column. Initially, the function is called with the full range of rows specified. It then recursively calls itself with smaller and smaller intervals specified. Once the interval length is smaller than two, it simply returns. Otherwise, it executes the following steps: firstly, it calls the function `SortEvenOdd(interval)`. This function rearranges the rows in the specified interval. It copies each even row one after the other into a new column, then each odd row. Finally, it overwrites the specified interval in the original column with the rows from the new column, containing the re-arranged rows. To make this process memory efficient, dynamic memory allocation must be avoided or reduced to the absolute necessary minimum. For this purpose, `SortEvenOdd` uses a statically allocated vector which is initialized, triggering the internal dynamic memory allocation of `std::vector` only once, when `SortEvenOdd` is called for the first time. Here, the full number of rows of the interval, specified at the initial call of `SortEvenOdd(interval)`, is used. After `SortEvenOdd` returns, `RecurseFFT` calls `RecurseFFT(`first half of `interval)`, then it calls `RecurseFFT(`second half of `interval)`. Finally, each row gets a value assigned according to

`column(k) = even +` $e^{i\omega t}$ `odd`

`column(k + interval / 2) = even -` $e^{i\omega t}$ `odd`

for $k \in$ `first half of interval`, where
`even = column(k), odd = column(k + interval/2),` $\omega \cdot t =$`k / interval`

The computation time for an FFT of N samples is proportional to $N \cdot \log N$, which is an advantage for large data-files, where a naive, integral-based calculation would require time proportional to N^2.

Once the FFT is calculated, various filters can be applied in the frequency domain. For a single data-file, high-/low-/band-pass or notch-filters can be applied. For two data-files, cross-correlation, convo-

lution and inverse convolution of any original data channel with one reference data channel can be calculated. In QUICK, there are dedicated deconvolution filters for the calculation of the impulse response and for inverse filtering. Compared to the straight-forward inverse convolution they include frequency-smoothening, a noise-term (see section 2.3.5) and optional application of the Kramers-Kronig relations to ensure a causal impulse-response (see section D.3).

To return to the time domain, the FFT is inverted by applying the function `RecurseFFT` on each previously Fourier-transformed column and then applying complex conjugation. The time column is calculated based on the frequency range of the Fourier transformed data such that the total time interval is the sample count divided by f_{max}.

For more details, see the source-code of QUICK, specifically the files:
`grascha-analysis.h` and `grascha-analysis.cpp`.

D.2. Time-Frequency-Analysis

By measuring the group velocity of Gaussian tone-bursts at different center frequencies, we can obtain the dispersion relation of a given granular packing. The signals consist of approx. 5 cycles. The frequency is varied from 500 Hz to 40 kHz. To save time while in microgravity during the flight, we record 8 successive bursts of different frequency in one waveform. As in chapter 2, we use signals of the two accelerometers within the packing, separated by a fixed distance. To obtain the dispersion relation we use the following methods:

For each burst the phase velocity v_ϕ is determined by peak-fitting under the constraint that the signal peak of the close sensor precede the peak of the far sensor. Alternatively we determine the global maximum of the cross-correlation of both signals. The group velocity v_G is then obtained by the relation:

$$v_G = \left(\frac{dk}{df}\right)^{-1} = \left(\frac{d\frac{f}{v_\phi}}{df}\right)^{-1} \tag{D.1}$$

This was found to be the most reliable method for all packings.

Alternatively we calculate the group velocity from the cross-phase spectrum $\delta\phi(f)$ using the relation:

$$v_G = 2\pi \cdot \delta x \cdot \left(\frac{d\delta\phi(f)}{df}\right)^{-1} \tag{D.2}$$

$\delta\phi(f)$ is obtained either by subtracting the phase spectra of both sensor signals, or, by first calculating the transfer function by inverse convolution of the two signals and then calculating the phase spectrum of the transfer function. In the former case phase unwrapping is required to remove jumps resulting from the 2π-periodicity of the phase. This is not necessary for the latter method. However, calculation of the transfer function relies on proper handling of noise- and bias-induced artifacts. These methods use heuristically chosen parameters as described in section *Pulse Shaping*.

Furthermore, the group velocity can be determined more directly by analysis of the signal envelope time-of-flight. First, we determine the analytic signal $s(t)$ of the measured real signal $x(t)$:

$$s(t) = x(t) + i \cdot H[x(t)] \tag{D.3}$$

where we use the Hilbert transform:

$$H[f(t)] = \frac{1}{\pi}\text{p.v.}\int_{-\infty}^{\infty}\frac{f(\xi)}{t-\xi}\mathrm{d}\xi \tag{D.4}$$

In practice, the analytic signal is calculated in the Fourier domain using:

$$x(t) \xrightarrow{FFT} X(\omega) \xrightarrow{H} S(\omega) = \begin{cases} 2\cdot X(\omega) & \omega > 0 \\ X(\omega) & \omega = 0 \\ 0 & \omega < 0 \end{cases} \xrightarrow{IFFT} s(t) \tag{D.5}$$

Then $\|s(t)\|$ is the signal envelope. We use peak-fitting to obtain the time-of-flight between the maxima of the two sensor signal envelopes. Alternatively, we use the cross-correlation peak.

In practice, the received signals contain a variety of frequencies other than the burst frequency. To isolate the proper burst, we apply a lock-in filter. It is implemented by first dividing the captured waveform into intervals of period T, determining the in-phase and out-of-phase coefficients

$$a_i = \frac{\int_0^T x(t_i+t)\cos(2\pi t/T)\mathrm{d}t}{\int_0^T \cos(2\pi t/T)\mathrm{d}t} \tag{D.6}$$

and

$$b_i = \frac{\int_0^T x(t+t_i)\sin(2\pi t/T)\mathrm{d}t}{\int_0^T \sin(2\pi t/T)\mathrm{d}t} \tag{D.7}$$

for each interval i, linearly interpolating the coefficients for time $t_i < t < t_i + T$, smoothening the interpolated coefficients with a Gaussian Kernel of width T and finally reconstructing the filtered signal as

$$x_{Lock-in}(t) = a_i \cdot \cos(2\pi t'/T) + b_i \cdot \sin(2\pi t'/T) \tag{D.8}$$

with $t = t_i + t'$ and $0 \le t' < T$.

Another complication is the appearance of reflected signals in the measurements, visible as secondary peaks in the envelope. To make sure the analysis is sensitive to the first peak only, we determine the time of arrival of the leading edge using a threshold of 0.1 relative to the global maximum in the region-of-interest. The result for a series of test measurements is shown in figure D.1 where we also show the predicted dispersion relation for a monodisperse chain of particles with diameter d according to $v_G = \frac{d\omega}{dk} = c\cdot\cos(q)$ with $q = \arcsin\left(\frac{\omega d}{2c}\right)$ and with the speed of sound c. We assume a Pseudo-Brioullin zone at $k = \pi/d$. The experimentally obtained dispersion relation does not correspond to this simplified model where polydispersity, disorder in terms of contact stiffness and contact number as well as nonlinear behavior are neglected.

The methods described above are based on knowledge of the signal shape in terms of burst frequency and duration. A more general method that is applicable to signals containing a large variety of frequencies at different times is analysis of distributions that represent the signal as a function of both time and frequency. We use the smoothed Pseudo-Wigner-Ville distribution of the measured coherent signal after a series of bursts or (inverse-filtered) white exponential chirp excitation to obtain dispersion relations of different packing configurations. The Wigner-Ville distribution is given by:

$$W(t,\omega) = \frac{1}{2\pi}\int_{-\infty}^{\infty} s(t+\tau/2)s^*(t-\tau/2)\mathrm{e}^{-i\omega\tau}\mathrm{d}\tau \tag{D.9}$$

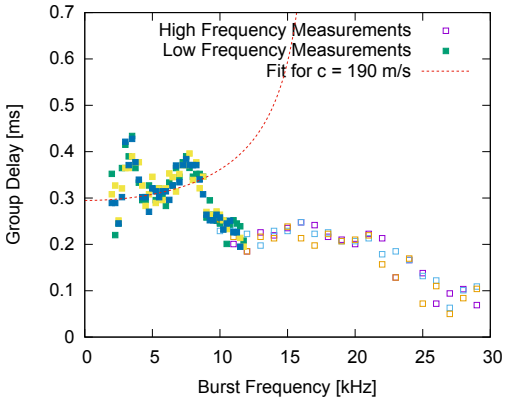

Figure D.1.: Group delay of Gaussian tone-bursts with center frequencies from 2 - 30 kHz, obtained through the time-of-arrival of the leading edge of the Lock-in filtered signal's envelope (open and filled squares). For comparison, the prediction for a linear chain is shown (dashed line).

Then for any given time t the instantaneous frequency f_i is given as the first order moment:

$$f_i(t) = \frac{\int_0^\infty f W(t,f)\mathrm{d}f}{\int_0^\infty W(t,f)\mathrm{d}f} \tag{D.10}$$

Analogously, for any frequency-component f the group-delay t_g is given by:

$$t_g(f) = \frac{\int_{-\infty}^\infty t W(t,f)\mathrm{d}t}{\int_{-\infty}^\infty W(t,f)\mathrm{d}t} \tag{D.11}$$

However, in practice these definitions can not be used directly due to interference terms of different frequencies present at the same time (as the Wigner-Ville transform is quadratic) as well as reflected and distorted signals leading to shifted group-delay.

To get rid of the interference terms we convolute the Wigner-Ville transform with Gaussian kernels both in time and frequency. If the kernel widths δt and δf satisfy the Heisenberg-Gabor uncertainty relation

$$\delta t \cdot \delta f \geq \frac{1}{4\pi} \tag{D.12}$$

then the interference terms vanish [2].

To avoid the group-delay shifts we use peak fitting at the global maximum for each frequency instead of the first order moment.

All methods described in this section are sensitive to the selection of the region-of-interest in the data due to distortions with respect to the ideal Gaussian shape resulting from reflection of the wave at the cell wall and signal distortion by the granular medium. To obtain reproducible results we restrict the region of interest to few oscillation cycles at the beginning of the burst, which is always the cleanest

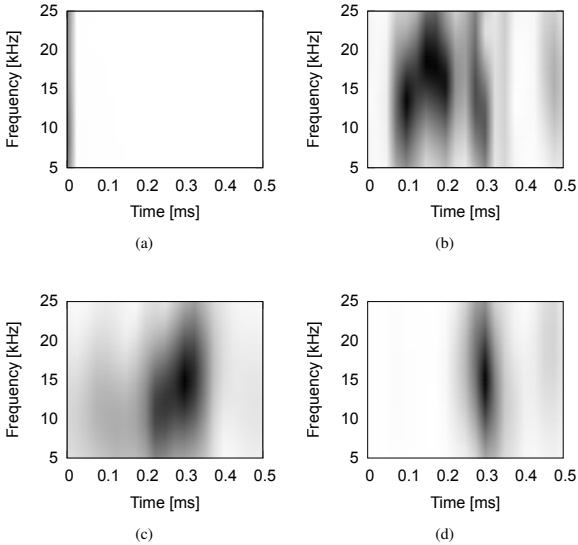

Figure D.2.: Smoothed Pseudo-Wigner-Ville distribution of the transfer function between sensors at different distances from the voice-coil after excitation with a series of 40 bursts with increasing center frequency from 10 to 20 kHz: (a) same sensor, (b) accelerometers 56 mm apart, (c) accelerometer and upper piezo, 88 mm apart, (d) accelerometer and lower piezo, 88 mm apart. Due to the height difference of 54 mm the piezos are exposed to different static pressure, resulting in shorter delay as measured by the lower sensor.

part of the signal. While this works well for the phase velocity determination by peak-fitting or cross-correlation, it is more difficult to apply to the other methods as they require a larger time interval. Extending the region-of-interest beyond the undistorted part of the signal yields nonsensical results. Additionally, if the time-of-flight changes significantly with frequency, the region of interest has to be changed accordingly, making the analysis unreliable and badly reproducible for all but the first method described here.

D.3. Causal Time-Frequency-Analysis

The time-frequency analysis shown in the previous section is prone to artifacts that are difficult to filter out. To get more accurate results it is helpful to impose constraints on the physical quantities under investigation, such as causality (effects do not preceed their causes) which we apply in this section to the transfer function $H(\omega) = \frac{A_{far}(\omega)}{A_{close}(\omega)}$ for the sensor signals $a_{close}(t)$ and $a_{far}(t)$ measured within the granular packing at different distances close and far to the excitation source.

Given a minimal-phase transfer function $H(\omega) = G(\omega)\mathrm{e}^{i\theta(\omega)}$. Then its complex logarithm $\mathrm{Log}(H)(\omega) = \log\|G(\omega)\| + i\theta(\omega)$ is analytic. Its inverse Fourier transform, the cepstrum, is causal, i.e. it is zero for negative times. The real and imaginary parts form a Hilbert pair related through Kramers-Kronig relations:

$$\theta(\omega) = \frac{1}{\pi}\text{p.v.}\int_{-\infty}^{\infty}\frac{\log\left(G(\xi)\right)\mathrm{d}\xi}{\omega-\xi} = \left(\log(G) * \frac{1}{\pi\omega}\right)(\omega) \tag{D.13}$$

and

$$\log(G)(\omega) = -\frac{1}{\pi}\text{p.v.}\int_{-\infty}^{\infty}\frac{\theta(\xi)\mathrm{d}\xi}{\omega-\xi} = -\left(\theta * \frac{1}{\pi\omega}\right)(\omega) \tag{D.14}$$

Now we can calculate the phase spectrum $\mathrm{e}^{i\theta(\omega)}$ from the known amplitude spectrum $G(\omega)$ based on equation D.13. In practice, the Hilbert transform is calculated with a FFT-based implementation where we use

$$FT\left(\frac{1}{\pi\omega}\right) = -i\cdot\operatorname{sgn}(\tau) = \begin{cases} -i & \tau > 0 \\ 0 & \tau = 0 \\ i & \tau < 0 \end{cases} \tag{D.15}$$

and the empirical transfer function is Gauss-smoothed and regularized with a noise-term as described in section 2.3.5 via equation 2.12 to ensure the absence of isolated poles and zeros and $h(t) = 0$ for $t < 0$.

D.4. Sensor Response

The sound measurements are affected by the finite size of the sensors. Our accelerometers are of cubic shape with $L = 10$ mm edge length, so each side is in contact with 6 - 11 beads. The wavelengths are in the range 7 - 100 mm. While a simple treatment of the sensors as point-like receivers seems reasonable at the largest wavelengths, a more detailed analysis is needed for the smaller wavelengths.

The net force acting on an accelerometer is the sum of contact forces between it and its neighboring particles. For simplicity we assume the accelerometer can be treated as a probe particle within a continuous elastic medium through which pressure waves $p(x,t)$ with well-defined phase speed v_ϕ can propagate without being scattered by the accelerometer. Also we neglect tangential forces. Then the net force is given by the pressure difference acting on opposing sides of the sensor, leading to the acceleration:

$$a(t) = \frac{L^2}{m_a}\left[p(x_0+L,t) - p(x_0,t)\right] \tag{D.16}$$

Here $m_a = 5.0$ g is the sensor mass. For long wavelengths $L/\lambda \to 0$ we can approximate the pressure difference by the pressure derivative along the sensor axis:

$$a(t) = \frac{L^2}{m_a}\left.\frac{\partial p}{\partial x}\right|_{x_0,t}\cdot L + \mathcal{O}(\|L\|^2) \tag{D.17}$$

For $p = p(t - x/v_\phi)$ we can use $\partial_x p = -(1/v_\phi)\partial_t p$ to get:

$$a(t) \xrightarrow{\frac{L}{\lambda}\to 0} -\frac{L^2}{m_a}\frac{L}{v_\phi}\left.\frac{\partial p}{\partial t}\right|_{x_0,t} \tag{D.18}$$

Therefore the accelerometer acts as a differentiating or high-pass filter on the signal representing the local pressure acting on its surface at x_0. The original signal can be obtained simply by integrating the measured sensor output.

In the more general case, applicable to all wavelengths, the accelerometer signal is given by convolution of $p(t)$ with the impulse response $h(t)$:

$$a(t) = \frac{L^2}{m_a 0}(p_{x_0} * h)(t) \tag{D.19}$$

with

$$h(t) = \delta(t) - \delta(t - L/v_\phi) \tag{D.20}$$

$$= \frac{1}{2\pi}\int_{-\infty}^{\infty}\left(1 - e^{-i\omega L/v_\phi}\right)e^{i\omega t}d\omega \tag{D.21}$$

Then the original signal can be obtained by inverse convolution:

$$p(x_0,t) = \frac{m_a}{L^2}(a * h^{-1})(t) \tag{D.22}$$

$$= \frac{m_a}{L^2}\frac{1}{2\pi}\int_{-\infty}^{\infty}\frac{\hat{\mathbf{a}}(\omega)e^{i\omega t}}{1-(1-\varepsilon)e^{-i\omega L/v\phi}}d\omega \tag{D.23}$$

Here we introduced $\varepsilon \in (0;1]$ to regularize the integral which otherwise suffers from infinitely many isolated poles. Physically this corresponds to attenuation along the length of the sensor. In experiments with two accelerometers separated by distance x in packings of glass beads we found $a(x) \approx a(0)e^{-x/l_a}$ with $l_a \approx 30$ mm for low amplitude waves at 1 kPa confinement pressure, as is common in our ground-based experiments. Therefore $\varepsilon \approx 0.3$ is a realistic value.

It is obvious that if a linear-phase low-pass filter term is used to restrict the bandwidth to small frequencies, Eq. (D.23) will approximate an integrating filter as suggested above as treatment for the long-wavelength case.

An FFT-based filter according to Eq. (D.23) is implemented in our data analysis code.

The piezo sensors are not affected by finite-size affects analogous to the accelerometers because only one flat side is exposed to the granular packing while the sensor body is embedded in the cell wall within a dedicated housing. We found the piezo acts as a differentiating filter acting on a force signal such that

$$\frac{1}{k_{piezo}}\int_0^t V_{piezo}(t')dt' = p(t) - p(0) \tag{D.24}$$

where $k_{piezo} \approx 39\frac{nV\cdot s}{Pa}$ was determined in a calibration measurement, where known weights ~ 1 kg were carefully repeatedly placed on and removed from the piezos on a flat surface.

Bibliography

[1] James W Cooley and John W Tukey. An algorithm for the machine calculation of complex fourier series. *Mathematics of computation*, 19(90):297–301, 1965.

[2] N Yen. Time and frequency representation of acoustic signals by means of the wigner distribution function: Implementation and interpretation. *J. Acoust. Soc. Am.*, 81:1841–1850, 06 1987.

E. Further Calculations

E.1. Displacement Field Theory

Instead of starting from Newton's second law of motion we start with the Lagrangian density:

$$\mathcal{L}\left(\mathbf{u}(\mathbf{x},t),\partial_t\mathbf{u}(\mathbf{x},t),\partial_j\mathbf{u}(\mathbf{x},t)\right)=\frac{1}{2}\rho(\mathbf{x})\left(\partial_t\mathbf{u}(\mathbf{x},t)\right)^2-\frac{1}{2}\lambda(\mathbf{x})\left(\nabla\cdot\mathbf{u}(\mathbf{x},t)\right)^2-\mu(\mathbf{x})\varepsilon_{ij}\varepsilon_{ij} \tag{E.1}$$

Its functional derivatives are:

$$\begin{aligned}
\frac{\delta\mathcal{L}}{\delta\left(u_i\right)}&=0\\
\frac{\delta\mathcal{L}}{\delta\left(\partial_t u_i\right)}&=\rho(\mathbf{x})\partial_t u_i(\mathbf{x},t)\\
\frac{\delta\mathcal{L}}{\delta\left(\partial_j u_i\right)}&=-\lambda(\mathbf{x})\delta_{ij}\partial_k u_k(\mathbf{x},t)-\mu(\mathbf{x})\left(\delta_{ik}\delta_{jl}+\delta_{il}\delta_{jk}\right)\varepsilon_{kl}(\mathbf{x},t)
\end{aligned} \tag{E.2}$$

Now we demand the action be stationary under variation of $\mathbf{u}$ and its derivatives:

$$\mathrm{d}S\left[u_i,\partial_t u_i,\partial_j u_i\right]=\mathrm{d}\int_0^T\iiint_{\mathbb{R}^3}\mathcal{L}\left(u_i,\partial_t u_i,\partial_j u_i\right)\mathrm{d}^3x\mathrm{d}t\stackrel{!}{=}0 \tag{E.3}$$

If the displacement and its derivatives vanish at the boundary then (E.3) is satisfied if the Euler-Lagrange equation is satisfied:

$$\frac{\delta\mathcal{L}}{\delta u_i}=\partial_t\frac{\delta\mathcal{L}}{\delta\left(\partial_t u_i\right)}+\partial_j\frac{\delta\mathcal{L}}{\delta\left(\partial_j u_i\right)} \tag{E.4}$$

which leads immediately to:

$$\begin{aligned}
0=&\rho(\mathbf{x})\partial_t^2 u_i(\mathbf{x},t)-\lambda(\mathbf{x})\partial_i\partial_k u_k(\mathbf{x},t)-2\mu(\mathbf{x})\partial_j\varepsilon_{ij}(\mathbf{x},t)\\
&+\left(\partial_i\lambda(\mathbf{x})\right)\left(\partial_k u_k(\mathbf{x},t)\right)+2\left(\partial_j\mu(\mathbf{x})\right)\varepsilon_{ij}(\mathbf{x})
\end{aligned} \tag{E.5}$$

which is identical to the wave equation (1.102) in section 1.3.1.

E.2. Calculation of Scattering Mean Free Path

E.2.1. Operator Potential and Correlation Functions

Baydoun et al[1] derived an operator potential and related correlation functions from linear hydrodynamics. A similar operator potential follows immediately from the Schrödinger equation without additional assumptions:

We recall from section 1.2.2 Eq. (1.18) that in the monochromatic case but now with varying $\mu(x)$ and $\rho(x)$ we have

$$\mathbf{H}\Psi(x,t) = \omega\Psi(x,t)$$
$$ic(x)\frac{\partial}{\partial x}\begin{pmatrix}\sqrt{\frac{\mu(x)}{2}}\frac{\partial}{\partial x}\\ -i\omega\sqrt{\frac{\rho(x)}{2}}\end{pmatrix}v(x) = \omega\begin{pmatrix}-i\omega\sqrt{\frac{\rho(x)}{2}}\\ \sqrt{\frac{\mu(x)}{2}}\frac{\partial}{\partial x}\end{pmatrix}v(x) \tag{E.6}$$

which immediately yields the inhomogeneous Helmholtz equation

$$\left(\frac{\partial^2}{\partial x^2}+k_0^2\right)v(x) = k_0^2\left(\alpha(x)-\frac{1}{2}\frac{1}{k_0^2}\frac{1}{\mu(x)}\frac{\partial}{\partial x}\mu(x)\frac{\partial}{\partial x}\right)v(x) \tag{E.7}$$

or more conveniently written:

$$\left(\frac{\partial^2}{\partial x^2}+k_0^2\right)v(x) = k_0^2\left(\alpha(x)-\frac{1}{2k_0^2}\frac{\partial}{\partial x}\beta(x)\frac{\partial}{\partial x}\right)v(x) \tag{E.8}$$

where we have used

$$c_0 = \sqrt{\frac{\mu_0}{\rho_0}} \quad \text{and} \quad k_0 = \frac{\omega}{c_0}$$
$$\alpha(x) = 1-\frac{c_0^2}{c^2(x)} \quad \text{and} \quad \beta(x) = \ln\frac{\mu(x)}{\mu_0} \tag{E.9}$$

Thus, the effect of disorder is expressed as a scalar potential depending on $\alpha(x)$ and an operator potential depending on $\beta(x)$. The self-energy will then contain four correlation functions:

$$\begin{aligned}C_{\alpha\alpha}(x-x') &= \langle\alpha(x)\alpha(x')\rangle\\ C_{\beta\alpha}(x-x') &= \langle\beta(x)\alpha(x')\rangle = \langle\alpha(x)\beta(x')\rangle = C_{\alpha\beta}(x-x')\\ C_{\beta\beta}(x-x') &= \langle\beta(x)\beta(x')\rangle\end{aligned} \tag{E.10}$$

Here we have assumed that the processes α and β be jointly stationary, isotropic and homogeneous thus the correlation functions depend only on $|x-x'|$.

E.2.2. Calculation based on Helmholtz Equation

3D Green's function

To get the Green's function of the homogeneous equation, we first apply the Fourier transform:

$$\left(\Delta+\frac{\omega^2}{c_0^2}\right)G(\mathbf{x}) = \delta^3(\mathbf{x})$$
$$\xrightarrow{\mathcal{F}}\left(-k^2+\frac{\omega^2}{c_0^2}\right)G(\mathbf{k}) = 1 \tag{E.11}$$

Then we solve for $G(\mathbf{k})$ and apply the inverse transform, taking advantage of the spherical symmetry of (E.11). We also apply a small imaginary part to regularize the integral by analytic continuation and contour integration over the real-axis plus a half-circle in the upper complex half-plane:

$$\begin{aligned}
G(\mathbf{x}) &= \mathcal{F}^{-1}\left[\frac{1}{(k-\omega/c_0)(k+\omega/c_0)}\right] \\
&= \frac{1}{(2\pi)^3}\iiint_{\mathbb{R}^3}\frac{\mathrm{e}^{i\mathbf{k}\mathbf{x}}}{(k-\omega/c_0-i\varepsilon)(k+\omega/c_0+i\varepsilon)}\mathrm{d}^3k \\
&= \frac{1}{(2\pi)^3}\int_0^{2\pi}\int_0^{\infty}\int_0^{\pi}\frac{\mathrm{e}^{ikr\cos(\theta)}}{(k-\omega/c_0-i\varepsilon)(k+\omega/c_0+i\varepsilon)}k^2\sin(\theta)\mathrm{d}\theta\mathrm{d}k\mathrm{d}\phi \\
&= \frac{1}{(2\pi)^2}\int_0^{\infty}\int_1^{-1}\frac{-k^2\mathrm{e}^{ikr\cos(\theta)}}{(k-\omega/c_0-i\varepsilon)(k+\omega/c_0+i\varepsilon)}\mathrm{d}(\cos(\theta))\mathrm{d}k \\
&= \frac{1}{ir(2\pi)^2}\int_{-\infty}^{\infty}\frac{k\mathrm{e}^{ikr}}{(k-\omega/c_0-i\varepsilon)(k-\omega/c_0+i\varepsilon)}\mathrm{d}k \\
&= \frac{2\pi i}{ir(2\pi)^2}\operatorname*{Res}_{k=\omega/c_0+i\varepsilon}\left(\frac{k\mathrm{e}^{ikr}}{(k-\omega/c_0-i\varepsilon)(k+\omega/c_0+i\varepsilon)}\right) \\
&\xrightarrow{\varepsilon\to 0} \frac{1}{4\pi r}\mathrm{e}^{ir\omega/c_0} \equiv G^+(\mathbf{x})
\end{aligned} \tag{E.12}$$

We are interested in the Green's function that describes outgoing waves. To ensure this, we apply the Sommerfeld radiation condition

$$r^{\frac{d-1}{2}}\left(\frac{\partial}{\partial r}-ik\right)G(\mathbf{x}) \xrightarrow{r\to\infty} 0 \tag{E.13}$$

which is satisfied by $G^+(\mathbf{x})$ because of our choice of the signs $\pm i\varepsilon$.

Scalar Exponentially Correlated Disorder in 3D

In the simplest case we have only the first correlation function as defined in (E.10) which we now simply call $C(\mathbf{x}-\mathbf{x}')$. An easy to calculate example is $C(\mathbf{x}-\mathbf{x}') = \frac{\sigma^2}{\mu^2}\mathrm{e}^{-|\mathbf{x}-\mathbf{x}'|/\ell_c}$ of a fluctuation with variance σ^2 around mean μ of some quantity (either the stiffness, the density or the local speed of sound) with correlation length ℓ_c. Then the self-energy in the Bourret approximation is simply:

$$\begin{aligned}
\Sigma_k(\omega) &= \mathcal{F}\left[\frac{k_0^4\sigma^2}{\mu^2}G^+(\mathbf{x})\mathrm{e}^{-|\mathbf{x}|/\ell_c}\right] \\
&= \frac{k_0^4\sigma^2}{\mu^2}\mathcal{F}\left[\frac{\mathrm{e}^{ir(k_0+i/\ell_c)}}{4\pi r}\right] \\
&= \frac{k_0^4\sigma^2}{\mu^2}\frac{1}{(k-k_0-i/\ell_c)(k+k_0+i/\ell_c)} \\
&\xrightarrow{k\to k_0} \frac{k_0^4\sigma^2}{\mu^2}\frac{\ell_c^2}{1-2ik_o\ell_c} = \frac{k_0^4\sigma^2\ell_c^2}{\mu^2}\frac{1+2ik_0\ell_c}{1+4k_0^2\ell_c^2}
\end{aligned} \tag{E.14}$$

In the last step we assumed $|\Sigma_k(\omega)| \ll k_0^2$ thus $k \approx k_0 = \omega/c_0$ can be used to calculate an approximation of Σ for weak disorder. Then the effective wavenumber is:

$$\begin{aligned} k_{\text{eff}} &= \sqrt{k_0^2 - \Sigma(\omega)} \\ &= k_0 \sqrt{1 - \frac{k_0^2 \sigma^2 \ell_c^2}{\mu^2 (1 - 2ik_0\ell_c)}} \\ &\approx k_0 - \frac{1}{2} \frac{k_0^3 \sigma^2 \ell_c^2}{\mu^2} \frac{1 + 2ik_0\ell_c}{1 + 4k_0^2\ell_c^2} \end{aligned} \tag{E.15}$$

Then the wave decays like $\mathrm{e}^{-r/(2\ell_s)}$ due to incoherent multiple scattering with the mean free path given by $1/(2\ell_s) = \mathrm{Im}(k_{\text{eff}})$ and thus

$$\ell_s = \frac{\mu^2}{k_0^4 \sigma^2 \ell_c^3} \frac{1 + 4k_0^2\ell_c^2}{2} \tag{E.16}$$

which is a well known result in the literature[1].

1D Green's function

In 1D the Green's function is:

$$\begin{aligned} G(x) &= \frac{1}{2\pi} \int_{\mathbb{R}} \frac{-\mathrm{e}^{ikx}}{(k - k_0 - i\varepsilon)(k + k_0 + i\varepsilon)} \mathrm{d}k \\ &= \frac{2\pi i}{2\pi} \operatorname*{Res}_{k=k_0+i\varepsilon} \left(\frac{-\mathrm{e}^{ikx}}{(k - k_0 - i\varepsilon)(k + k_0 + \varepsilon)} \right) \\ &\xrightarrow{\varepsilon \to 0} \frac{\mathrm{e}^{ik_0 x}}{2ik_0} \equiv G^+(x) \end{aligned} \tag{E.17}$$

Scalar Exponentially Correlated Disorder in 1D

The self-energy is:

$$\begin{aligned} \Sigma(\omega) &= \mathcal{F}\left[\frac{k_0^4 \sigma^2}{\mu^2} \frac{\mathrm{e}^{ik_0 x}}{2ik_0} \mathrm{e}^{i|x|/\ell_c} \right] \\ &= \frac{k_0^4 \sigma^2}{2ik_0 \mu^2} \left(\int_0^\infty \mathrm{e}^{x(ik - ik_0 - 1/\ell_c)} \mathrm{d}x + \int_{-\infty}^0 \mathrm{e}^{x(ik - ik_0 + 1/\ell_c)} \mathrm{d}x \right) \\ &= \frac{k_0^3 \sigma^2}{2i\mu^2} \left(\frac{1}{ik - ik_0 + 1/\ell_c} - \frac{1}{ik - ik_0 - 1/\ell_c} \right) \\ &\xrightarrow{k \to k_0} \frac{k_0^3 \sigma^2}{2i\mu^2} 2\ell_c = -i \frac{k_0^3 \sigma^2 \ell_c}{\mu^2} \end{aligned} \tag{E.18}$$

Again, we have used the on-shell approximation $k \approx k_0$ for $\Sigma(\omega)$. Then the effective wavenumber is:

$$\begin{aligned} k_{\text{eff}} &= \sqrt{k_0^2 - \Sigma} \\ &= k_0 \sqrt{1 - i\frac{\sigma^2 k_0 \ell_c}{\mu^2}} \\ &\approx k_0 - \frac{i}{2}\frac{\sigma^2 k_0^2 \ell_c}{\mu^2} \end{aligned} \tag{E.19}$$

Thus, the scattering mean free path is:

$$\begin{aligned} \frac{1}{2\ell_s} &= \text{Im}(k_{\text{eff}}) \\ \Rightarrow \ell_s &= \frac{\mu^2}{\sigma^2 k_0^2 \ell_c} \end{aligned} \tag{E.20}$$

E.2.3. Calculation based on Schrödinger Equation

Here I use the position representation of the Green's function of the granular sound Schrödinger equation instead of the eigenmode representation to calculate the self-energy. This is appropriate for P-waves, while in the general case, when both P- and S-waves are considered and mode-conversion has to be accounted for, then the mode representation is to be used for the calculation.

1D Green's function

We start with the momentum representation (1.26) which we analytically continue such that it has one pole each in the upper and lower complex half-plane:

$$\begin{aligned} G^0(\omega,k) &= \frac{\begin{pmatrix} \omega & ck \\ ck & \omega \end{pmatrix}}{c^2(k-\omega/c)(k+\omega)} \\ \xrightarrow{k\to z\in\mathbb{C}}\ G^0(\omega,z) &= \frac{\begin{pmatrix} \omega & cz \\ cz & \omega \end{pmatrix}}{c^2(z-\omega/c-i\varepsilon)(z+\omega/c+i\varepsilon)} \end{aligned} \tag{E.21}$$

Then we apply the inverse Fourier transform using the residue theorem while using two different integration contours for $x > 0$ and $x < 0$ to make sure the integral converges:

$$\begin{aligned} G^0(\omega,x) = \mathcal{F}^{-1}\left[G^0(\omega,k)\right](x) &= \lim_{\varepsilon\to 0}\frac{1}{2\pi c^2}\int_{-\infty}^{\infty}\frac{\begin{pmatrix} \omega & cz \\ cz & \omega \end{pmatrix}\mathrm{e}^{ixz}}{(z-\omega/c-i\varepsilon)(z+\omega/c+i\varepsilon)}\mathrm{d}z \\ &= \lim_{\varepsilon\to 0}\frac{\pm 2\pi i}{2\pi c^2}\Theta(\pm x)\operatorname*{Res}_{z=\pm\omega/c\pm i\varepsilon}\left[\frac{\begin{pmatrix} \omega & cz \\ cz & \omega \end{pmatrix}\mathrm{e}^{ixz}}{(z-\omega/c-i\varepsilon)(z+\omega/c+i\varepsilon}\right] \\ &= \frac{i}{2c}\left(\begin{pmatrix} 1 & 1 \\ 1 & 1 \end{pmatrix}\Theta(x)\mathrm{e}^{ix\omega/c} + \begin{pmatrix} 1 & -1 \\ -1 & 1 \end{pmatrix}\Theta(-x)\mathrm{e}^{-ix\omega/c}\right) \end{aligned} \tag{E.22}$$

1D Self-Energy

We consider a perturbation like (1.73) but which shall depend only on one scalar random process: $\delta\mathbf{H} = \frac{\delta c(x)}{c}\mathbf{H} = \frac{\delta\mu(x)}{2\mu}\cdot\mathbf{H}$ with correlation function $C(x-x') = \langle\delta\mu(x)\delta\mu(x')\rangle$ the leading order contribution to the self-energy is:

$$\Sigma_k(\omega) = \langle\int_0^L\int_0^L \Psi_k^*(x)\frac{\delta\mu(x)}{\mu}\mathbf{H}G(\omega,x-x')\frac{\delta\mu(x')}{\mu}\mathbf{H}\Psi_k(x')\mathrm{d}x\mathrm{d}x'\rangle \tag{E.23}$$

The integrals can be carried out by partial integration. If the boundary terms vanish then the $\delta\mu$ and $\mathbf{H}$ terms can be rearranged without considering derivatives of $\delta\mu$. Then we use $\mathbf{H}\Psi_k = c|k|\Psi_k$ and replace the ensemble average of the $\delta\mu$'s by the correlation function, yielding:

$$\Sigma_k(\omega) = c^2k^2\int_0^L\int_0^L \Psi_k^*(x)G(\omega,x-x')\Psi_k(x')C(x-x')\mathrm{d}x\mathrm{d}x' \tag{E.24}$$

Now we remember that $\Psi_k^*(x)\cdot\Psi_k(x')$ is proportional to $\mathrm{e}^{ik(x-x')}$. As it only depends on the difference $x-x'$ we can redefine the variables x and x' such that $\Psi_k^*\cdot\Psi_k$ and G as well as C only depend on x. Another way of saying this is all quantities under the integral are translation-invariant. The integration intervals can also be shifted due to the periodic boundary conditions on the granular chain as long as the length of the interval is kept constant at L. Then we can immediately integrate out x':

$$\begin{aligned}\Sigma_k(\omega) &= c^2k^2\int_0^L\int_0^L \Psi_k^*(x)G(\omega,x)\Psi_k(0)C(x)\mathrm{d}x\mathrm{d}x' \\ &= c^2k^2L\int_0^L \Psi_k^*(x)G(\omega,x)\Psi_k(0)C(x)\mathrm{d}x\end{aligned} \tag{E.25}$$

Now we remember the definition of the normalized 1D eigenmodes:

$$\Psi_k(x) = \frac{\mathrm{e}^{ikx}}{\sqrt{2L}|k|}\begin{pmatrix}|k|\\ k\end{pmatrix}$$

After a short calculation we find:

$$\begin{aligned}\begin{pmatrix}|k|\\ k\end{pmatrix}\begin{pmatrix}1 & 1\\ 1 & 1\end{pmatrix}\begin{pmatrix}|k|\\ k\end{pmatrix} &= 2\left(k^2+k\cdot|k|\right)\\ \begin{pmatrix}|k|\\ k\end{pmatrix}\begin{pmatrix}1 & -1\\ -1 & 1\end{pmatrix}\begin{pmatrix}|k|\\ k\end{pmatrix} &= 2\left(k^2-k\cdot|k|\right)\end{aligned} \tag{E.26}$$

According to (E.26) and the definition of the Green's function (E.22) it is guaranteed that $\Sigma_k(\omega)$ only contains one of the two terms of (E.22) i.e. only the $x>0$ term for $k>0$ or only the $x<0$ term for $k<0$. Now, without loss of generality, we consider only $k>0$:

$$\Sigma_k(\omega) = 2ick^2\int_0^L \mathrm{e}^{ix(\omega/c-k)}C(x)\mathrm{d}x \tag{E.27}$$

Exponentially Correlated Disorder

For $C(x) = \frac{\sigma^2}{\mu^2} e^{-|x|/\ell_c}$ we get:

$$\begin{aligned}\Sigma_k \omega &= \frac{2ick^2\sigma^2}{\mu^2} \int_0^L e^{x(i\omega/c - ik - 1/\ell_c}\, dx \\ &= \frac{2ick^2\sigma^2}{\mu^2} \frac{e^{L(-ik+i\omega/c-1/\ell_c)} - 1}{i(\omega/c-k) - \frac{1}{\ell_c}} \\ &\xrightarrow{L\to\infty} \frac{2ick^2\sigma^2}{\mu^2} \frac{1}{\frac{1}{\ell_c} - i(\omega/c-k)}\end{aligned} \tag{E.28}$$

In the last step we took the limit $L \to \infty$ to get a result that does not depend on L. For a long chain, or, due to periodic boundary conditions, for a long propagation time, this will be an appropriate approximation. Now we look at the on-shell approximation $k \approx \omega/c = k_0$:

$$\Sigma(k_0) = \frac{2ick_0^2\ell_c\sigma^2}{\mu^2} \tag{E.29}$$

Then the dressed Green's function in eigenmode representation is:

$$\begin{aligned}G(k_0) &= \sum_k \frac{|k\rangle\langle k|}{-ck_0 + c|k| - \Sigma(k_0)} \\ &= \sum_k \frac{|k\rangle\langle k|}{c\left(|k| - \left(k_0 + \frac{1}{c}\frac{2ik_0^2\ell_c\sigma^2}{\mu^2}\right)\right)}\end{aligned} \tag{E.30}$$

After comparing the dressed and naked Green's functions we can now introduce an effective wavenumber k_{eff}:

$$k_{eff} = k_0 + \frac{1}{c}\Sigma k_0 = k_0 + \frac{2ik_0^2\ell_c\sigma^2}{\mu^2} \tag{E.31}$$

Due to the imaginary part the wave is attenuated like $e^{-x/(2\ell_s)}$ with the scattering mean free path ℓ_s given by:

$$\ell_s = \frac{1}{2\mathrm{Im}(k_{eff})} = \frac{\mu^2}{4\sigma^2 k_0^2 \ell_c} \tag{E.32}$$

Up to a factor of 4 this is consistent with the analogous calculation (E.20) based on the Helmholtz equation.

3D P-Wave Green's Function

If we consider only P-waves, the time-evolution operator simplifies to:

$$\mathbf{H} = ic \begin{pmatrix} 0 & \nabla \\ \nabla & \mathbf{0}_{3\times 3} \end{pmatrix} \tag{E.33}$$

It is convenient to introduce the normalized eigenmodes:

$$\Psi_{\mathbf{k}}(\mathbf{x}) = \frac{\mathrm{e}^{-i\mathbf{k}\cdot\mathbf{x}}}{\sqrt{2L^3}\,|\mathbf{k}|} \begin{pmatrix} |k| \\ \mathbf{k} \end{pmatrix} \tag{E.34}$$

Of course they satisfy

$$\mathbf{H}\Psi_{\mathbf{k}} = c\,|\mathbf{k}|\,\Psi_{\mathbf{k}} \tag{E.35}$$

Then we need to determine the Green's function that satisfies

$$(i\partial_t - \mathbf{H})G(t,\mathbf{x}) = \delta(t)\delta^3(\mathbf{x}) \tag{E.36}$$

or in the Fourier domain:

$$(-\omega + c \begin{pmatrix} 0 & \mathbf{k} \\ \mathbf{k} & \mathbf{0}_{3\times 3} \end{pmatrix})G(\omega,\mathbf{k}) = \mathbf{1}_{4\times 4} \tag{E.37}$$

which is solved by

$$G(\omega,\mathbf{k}) = \frac{\begin{pmatrix} -\omega & c\mathbf{k} \\ c\mathbf{k} & -\omega\mathbf{1}_{3\times 3} \end{pmatrix}}{\omega - c^2\mathbf{k}\cdot\mathbf{k}} \tag{E.38}$$

We are actually interested in $G(\omega,\mathbf{x}-\mathbf{x}')$ which we obtain by inverse Fourier transform:

$$\begin{aligned} G(\omega,\mathbf{x}) &= \mathcal{F}^{-1}\left[G(\omega,\mathbf{k})\right](\mathbf{x}) = \frac{1}{(2\pi)^3}\iiint_{\mathbb{R}^3} G(\omega,\mathbf{k})\mathrm{e}^{i\mathbf{k}\cdot\mathbf{x}}\mathrm{d}^3k \\ &= \frac{1}{c^2}\frac{1}{(2\pi)^3}\int_0^{2\pi}\int_0^{\infty}\int_1^{-1} \frac{\begin{pmatrix} -\omega & c\mathbf{k} \\ c\mathbf{k} & -\omega\mathbf{1}_{3\times 3} \end{pmatrix}\mathrm{e}^{ikr\cos(\theta)}}{(k-\omega/c)(k+\omega/c)} k^2\mathrm{d}\left(\cos(\theta)\right)\mathrm{d}k\mathrm{d}\phi \end{aligned} \tag{E.39}$$

Here we conveniently switched to spherical coordinates such that $k = |\mathbf{k}|$, $r = |\mathbf{x}|$ and $\mathbf{k}\cdot\mathbf{x} = kx\cos(\theta)$. The ϕ-integral only results in a factor 2π since nothing explicitly depends on ϕ. Let $\hat{\mathbf{x}}$ and $\hat{\mathbf{k}}$ denote unit vectors in the direction of $\mathbf{x}$ and $\mathbf{k}$. Then, before we conduct the $\cos(\theta)$-integral, we use that $\mathbf{k}\mathrm{e}^{i\mathbf{k}\cdot\mathbf{x}} = -i\nabla\mathrm{e}^{i\mathbf{k}\cdot\mathbf{x}}$ to simplify the integral:

$$
\begin{aligned}
G(\omega,\mathbf{x}) &= \frac{\begin{pmatrix}-\omega & ic\nabla\\ ic\nabla & -\omega\mathbf{1}_{3\times3}\end{pmatrix}}{c^2(2\pi)^2}\int_0^\infty\int_1^{-1}\frac{\mathrm{e}^{ikr\cos(\theta)}k^2}{k-\omega/c)(k+\omega/c)}\mathrm{d}(\cos(\theta))\mathrm{d}k\\
&= \frac{\begin{pmatrix}\omega & -ic\nabla\\ -ic\nabla & \omega\mathbf{1}_{3\times3}\end{pmatrix}}{irc^2(2\pi)^2}\int_0^\infty\frac{\left(\mathrm{e}^{ikr}-\mathrm{e}^{-ikr}\right)k}{k-\omega/c)(k+\omega/c)}\mathrm{d}k\\
&= \lim_{\varepsilon\to0}\frac{\begin{pmatrix}\omega & -ic\nabla\\ -ic\nabla & \omega\mathbf{1}_{3\times3}\end{pmatrix}}{irc^2(2\pi)^2}2\pi i\operatorname*{Res}_{z=\omega/c+i\varepsilon}\left(\frac{\mathrm{e}^{irz}z}{(z-\omega/c-i\varepsilon)(z+\omega/c+i\varepsilon)}\right)\\
&= \frac{\begin{pmatrix}\omega & -ic\nabla\\ -ic\nabla & \omega\mathbf{1}_{3\times3}\end{pmatrix}}{rc^2 2\pi}\frac{\mathrm{e}^{ir\omega/c}}{2}\\
&= \frac{\omega}{c^2}\frac{\mathrm{e}^{ir\omega/c}}{4\pi r}\begin{pmatrix}1 & \hat{\mathbf{x}}\\ \hat{\mathbf{x}} & \mathbf{1}_{3\times3}\end{pmatrix}
\end{aligned}
\tag{E.40}
$$

Here we used an analytic continuation with one pole each in the upper/lower complex half-plane in order to get the retarded Green's function representing outgoing waves.

3D Self-Energy for P-Waves

Analogous to the 1D case we assume a perturbation $\delta\mathbf{H}=\delta\mu(\mathbf{x})/\mu\cdot\mathbf{H}$ with correlation function $C(\mathbf{x}-\mathbf{x}')=\langle\delta\mu(\mathbf{x})\delta\mu(\mathbf{x}')\rangle$. The leading order contribution to the self-energy is:

$$
\begin{aligned}
\Sigma_{\mathbf{k}}(\omega) &= \langle\iiint_{V'}\iiint_{V}\Psi^*_{\mathbf{k}}(\mathbf{x})\delta\mathbf{H}(\mathbf{x})G(\omega,\mathbf{x}-\mathbf{x}')\delta\mathbf{H}(\mathbf{x}')\Psi_{\mathbf{k}}(\mathbf{x}')\mathrm{d}^3x\mathrm{d}^3x'\rangle\\
&= L^3\iiint_{V}c^2k^2\begin{pmatrix}k\\ \mathbf{k}\end{pmatrix}\begin{pmatrix}1 & \hat{\mathbf{x}}\\ \hat{\mathbf{x}} & \mathbf{1}_{3\times3}\end{pmatrix}\begin{pmatrix}k\\ \mathbf{k}\end{pmatrix}\frac{\mathrm{e}^{-i\mathbf{k}\cdot\mathbf{x}}}{2L^3k^2}\frac{\omega}{c^2}\frac{\mathrm{e}^{ir\omega/c}}{4\pi r}C(\mathbf{x})d^3x
\end{aligned}
\tag{E.41}
$$

As in the 1D case we have assumed translation invariance to carry out the first volume integral and we have changed the order of $\delta\mu(\mathbf{x})$ and $\mathbf{H}$ and used $\mathbf{H}\Psi_{\mathbf{k}}=ck\Psi_{\mathbf{k}}$. We denote $|\mathbf{k}|$ with k and $|\mathbf{x}|$ with r. The ensemble average of the two $\delta\mu$ terms was replaced by $C(\mathbf{x})$. Both volumes are of size L^3, matching the normalization of the eigenmodes.

Now we use this:

$$
\begin{pmatrix}k\\ \mathbf{k}\end{pmatrix}\begin{pmatrix}1 & \hat{\mathbf{x}}\\ \hat{\mathbf{x}} & \mathbf{1}_{3\times3}\end{pmatrix}\begin{pmatrix}k\\ \mathbf{k}\end{pmatrix} = 2(k^2+k\cdot\hat{\mathbf{x}}\cdot\mathbf{k}) = 2k^2\left(1+\cos(\theta)\right)
\tag{E.42}
$$

We also quite conveniently realize that $\cos(\theta)\cdot\mathrm{e}^{-ikr\cos(\theta)}=\frac{i}{k}\frac{\partial}{\partial r}\mathrm{e}^{-ikr\cos(\theta)}$. Now we continue the calculation of the volume integral in spherical coordinates:

$$
\Sigma_{\mathbf{k}}(\omega) = -\frac{\omega k^2}{4\pi}\int_0^{2\pi}\int_0^{L}\int_1^{-1}\left(1+\frac{i}{k}\frac{\partial}{\partial r}\right)\mathrm{e}^{-ikr\cos(\theta)}\frac{\mathrm{e}^{ir\omega/c}}{r}C(\mathbf{x})r^2\mathrm{d}(\cos(\theta))\mathrm{d}r\mathrm{d}\phi
\tag{E.43}
$$

Exponentially correlated Disorder in 3D for P-Waves

Now we can easily calculate the self-energy for exponentially correlated disorder $C(\mathbf{x}-\mathbf{x}') = \frac{\sigma^2}{\mu^2}\mathrm{e}^{-r/\ell_c}$ with $r = |\mathbf{x}-\mathbf{x}'|$:

$$\begin{aligned}\Sigma_{\mathbf{k}}(\omega) &= -\frac{\omega k^2\sigma^2}{4\pi\mu^2}\int_0^{2\pi}\int_0^{L}\int_1^{-1}\left(1+\frac{i}{k}\frac{\partial}{\partial r}\right)\mathrm{e}^{-ikr\cos(\theta)}\mathrm{e}^{ir\omega/c}\mathrm{e}^{-r/\ell_c}r\mathrm{d}(\cos(\theta))\mathrm{d}r\mathrm{d}\phi \\ &= -\frac{\omega k^2\sigma^2}{2\mu^2}\int_0^{L}\int_1^{-1}\left(1+\frac{i}{k}\frac{\partial}{\partial r}\right)\mathrm{e}^{-ikr\cos(\theta)}\mathrm{e}^{ir\omega/c}\mathrm{e}^{-r/\ell_c}r\mathrm{d}(\cos(\theta))\mathrm{d}r \\ &= \frac{k\omega\sigma^2}{2i\mu^2}\int_0^{L}\left(1+\frac{i}{k}\frac{\partial}{\partial r}\right)\left(\mathrm{e}^{ikr}-\mathrm{e}^{-ikr}\right)\mathrm{e}^{r(i\omega/c-1/\ell_c)}\mathrm{d}r \end{aligned} \tag{E.44}$$

Now we take the large volume limit $L\to\infty$. Then the r-derivative term no longer contributes to the integral. The remaining part gives:

$$\begin{aligned}\Sigma_{\mathbf{k}}(\omega) &\xrightarrow{L\to\infty} \frac{k^2\omega\sigma^2}{2i\mu^2}\left(\frac{-1}{i(\frac{\omega}{c}+k)-\frac{1}{\ell_c}}-\frac{-1}{i(\frac{\omega}{c}-k)-\frac{1}{\ell_c}}\right) \\ &\xrightarrow{k\to\omega/c=k_0} \frac{ck_0^3\sigma^2}{\mu^2}\frac{\ell_c^2}{1-2ik_0\ell_c} = \frac{\sigma^2ck_0^3\ell_c^2}{\mu^2}\frac{1+2ik_0\ell_c}{1+4k_0^2\ell_c^2}\end{aligned} \tag{E.45}$$

In the last step we took the on-shell limit $k\to k_0$. Now we can write the dressed Green's function in terms of eigenmodes:

$$G(\omega) = \sum_{\mathbf{k}}\frac{|\mathbf{k}\rangle\langle\mathbf{k}|}{c\left(k-k_0+\frac{1}{c}\Sigma(k_0)\right)} = \sum_{\mathbf{k}}\frac{|\mathbf{k}\rangle\langle\mathbf{k}|}{c\left(k-k_0+\frac{\sigma^2k_0^3\ell_c^2}{\mu^2}\frac{1+2ik_0\ell_c}{1+4k_0^2\ell_c^2}\right)} \tag{E.46}$$

8

Then the effective wavenumber is

$$k_{eff} = k_0 - \Sigma(k_0)/c = k_0 - \frac{\sigma^2k_0^3\ell_c^2}{\mu^2}\frac{1+2ik_0\ell_c}{1+4k_0^2\ell_c^2} \tag{E.47}$$

Thus, the scattering mean free path is

$$\ell_s = \frac{1}{2\mathrm{Im}(k_{eff})} = \frac{1}{4}\frac{\mu^2}{\sigma^2}\frac{1+4k_0^2\ell_c^2}{k_0^4\ell_c^3} \tag{E.48}$$

Bibliography

[1] Ibrahim Baydoun, Diego Baresch, Romain Pierrat, and Arnaud Derode. Scattering mean free path in continuous complex media: Beyond the helmholtz equation. *Physical Review E*, 92(3):033201, 2015.

Erklärung zur Dissertation
gemäß der Promotionsordnung vom 02. Februar 2006 mit den Änderungsordnungen vom 10. Mai 2012, 16. Januar 2013 und 21. Februar 2014

Diese Erklärung muss in der Dissertation enthalten sein

Ich versichere, dass ich die von mir vorgelegte Dissertation selbständig angefertigt, die benutzten Quellen und Hilfsmittel vollständig angegeben und die Stellen der Arbeit – einschließlich Tabellen, Karten und Abbildungen –, die anderen Werken im Wortlaut oder dem Sinn nach entnommen sind, in jedem Einzelfall als Entlehnung kenntlich gemacht habe; dass diese Dissertation noch keiner anderen Fakultät oder Universität zur Prüfung vorgelegen hat; dass sie – abgesehen von unten angegebenen Teilpublikationen – noch nicht veröffentlicht worden ist, sowie, dass ich eine solche Veröffentlichung vor Abschluss des Promotionsverfahrens nicht vornehmen werde.
Die Bestimmungen der Promotionsordnung sind mir bekannt. Die von mir vorgelegte Dissertation ist von Prof. Dr. Matthias Sperl betreut worden.

Teilpublikationen:

Karsten Tell, Christoph Dreißigacker, Alberto Chiengue Tchapnda, Peidong Yu, and Matthias Sperl. Acoustic waves in granular packings at low confinement pressure. *Review of Scientific Instruments*, 91(3):033906, 2020

Datum / Unterschrift
08.06.2020 Karsten Tell

Non-official English translation (The German version must be included in the doctoral thesis)

"I declare that I have independently completed the dissertation I submitted, that the sources and tools used are completely cited and that parts of the dissertation - including tables, maps and figures -, taken from other sources (in the wording or the sense) in each individual case has been referred to as such. Further, I declare that this dissertation has not been submitted to any other Faculty or University and that - apart from the following partial publications - has not yet been published, and that I will not publish the dissertation before the end of the doctoral examination.
I am aware of the requirements of the doctoral regulations. The doctoral project and Dissertation has been supervised by Prof. Dr. Matthias Sperl."

Partial publications of the thesis:

Karsten Tell, Christoph Dreißigacker, Alberto Chiengue Tchapnda, Peidong Yu, and Matthias Sperl. Acoustic waves in granular packings at low confinement pressure. *Review of Scientific Instruments*, 91(3):033906, 2020

Date / Signature
08.06.2020 Karsten Tell